ISSN 0022-4766, Journal of Structural Chemistry, 2022, Vol. 63, No. 2, pp. 176-226. © Pleiades Publishing, Ltd., 2022.
Russian Text © The Author(s), 2022, published in Zhurnal Strukturnoi Khimii, 2022, Vol. 63, No. 2, pp. 109-162.

CRYSTALLINE AND NANOSTRUCTURED MATERIALS BASED ON TRANSITION METAL DICHALCOGENIDES: SYNTHESIS AND ELECTRONIC PROPERTIES

A. Yu. Ledneva[1]*, G. E. Chebanova[1],
S. B. Artemkina[1], and A. N. Lavrov[1]

The article reviews the current state of research of the synthesis, structural, electrophysical and spectroscopic properties of layered transition metal dichalcogenides (TMDs) of group 4-7 elements (M = Zr, Hf, Nb, Ta, Mo, W, Tc, Re; Q = S, Se, Te) depending on their morphology and modification. The changes in the properties of these compounds are considered upon the transition from crystalline materials to nanostructured and monolayer samples. We discuss “fine tuning” of electronic properties by introducing heteroatoms into the TMD structure: intercalation, when a heteroatom is introduced between layers, and isovalent and/or non-isovalent substitution in cationic and anionic sublattices. Practical applications of fine tuning of the properties of TMD based materials are discussed.

DOI: 10.1134/S0022476622020020

Keywords: transition metal dichalcogenides, solid solutions, substitutional solutions, electrophysical properties, electronic properties, nanomaterials.

INTRODUCTION

The origination and further development of modern branches of technology such as solid-state microelectronics, optoelectronics, nanoelectronics stimulate the search and study of new promising materials exhibiting a wider range of properties than those of already employed materials. The discovery of graphene drew attention to other related layered materials, e.g. transition metal dichalcogenides MQ_2 (TMDs). Even though many of these compounds have been already widely studied, they nowadays attract attention, along with other similar layered systems, due to the general interest to nanomaterials and nanotechnologies. Exceptional electronic, mechanical, thermal, and chemical properties of layered materials are now being explored on nanostructured samples as possible photo- and electro-catalysts, including in hydrogen evolution reactions [1-3], gas sensors [4], optoelectronic sensors [5], electrode materials for chemical current sources (batteries and accumulators [6, 7], including solar energy converters), solid lubricants, etc. [8, 9].

Modification of known materials is one way to construct new materials with improved properties finely tuned for each specific task. The uniqueness of TMD materials is related to their structure and provides wide possibilities for chemical modification. The first possibility is due to their layered structure: preparation of intercalated systems where a heteroatom or a molecule is introduced between the layers (e.g., intercalation with lithium and other alkali metals [10], copper [11], organic

---

[1]Nikolaev Institute of Inorganic Chemistry, Siberian Branch, Russian Academy of Sciences, Novosibirsk, Russia; *ledneva@niic.nsc.ru. Original article submitted July 24, 2021; revised August 23, 2021; accepted August 23, 2021.

0022-4766/22/6302-0176 © 2022 by Pleiades Publishing, Ltd.

molecules [12]), as well as splitting and manufacturing of few-layer and monolayer samples [13-17]. The second "source of possibilities" is the substitution of metal atoms in the cationic sublattice [8] and chalcogen atoms in the anionic TMD sublattice [18].

This review is devoted to modified TMDs MQ_2 with M atoms from groups 4-7 and periods 2 and 3 (M = Zr, Hf, Nb, Ta, Mo, W, Tc, Re; Q = S, Se, Te), their preparation, structure, properties. Since MoS_2 is currently a popular "model TMD" that has been discussed in more than 26 thousand publications for the past five years (according to Web of Science), we consider it only briefly in this review and focus mainly on other TMDs.

SYNTHESIS OF TMDs AND MODIFIED TMDs

The development of methods for the synthesis of crystalline and polycrystalline TMD samples also affected the preparation of their crystalline intercalates or compounds doped with metals or chalcogens. The growing interest in micro- and nano-sized TMD materials (and the development of available methods for such studies) expanded the synthesis of such compounds up to solution methods and modifications of chemical vapor deposition (CVD). The development of synthesis methods for the fabrication of nanometer thick ("few-layer") TMD crystallites is also interesting in terms of obtaining new physical characteristics upon the transition from bulk crystals to nanocrystals composed of a small number of molecular layers as well as to mono- and oligolayers.

Synthesis of crystalline and polycrystalline TMDs

Crystals and crystalline TMD powders can be prepared from elements in close to stoichiometric ratios using the oxidation of metals by chalcogens. The decrease of oxidation potentials from sulfur to tellurium requires increased synthesis temperatures in this series. The methods for the TMD synthesis for all metals considered in the present article was summarized in [19]. To some extent, chalcogen atoms in these reactions act as transport agents, and relatively high synthesis temperatures (> 700 °C) exclude the formation of trichalcogenides MQ_3. In the case of group 4 and 5 metals, the pressure of chalcogen (primarily, sulfur and selenium) in the TMD synthesis is important to exclude the formation of non-stoichiometric dichalcogenides. It is known that low sulfur pressure leads to the formation of so-called self-intercalates $M_{1+x}S_2$: 3R–$Nb_{1+x}S_2$, $x > 0.07$ [20], $Ti_{1+x}S_2$, $0.005 < x < 0.014$ [21] or $0.20 < x < 0.33$ [22]. To prepare stoichiometric compounds MQ_2, pressure is controlled using chalcogen excess (up to 10%). Other transport agents are also used: iodine, bromine [23], Ar/H_2 mixture [24], phosphorus [20], phosphorus chalcogenides P_2S_5 and P_2Se_5 [25], and halides of chalcogens ($SeCl_4$) and metals ($TaCl_5$ [26]). The preparation of well crystallized ReS_2 and $ReSe_2$ from elements requires high temperatures (1000-1150 °C) and long-term syntheses in ampoules using transport agents [25]. The use of rhenium oxides or ammonium perrhenate in the synthesis of ReS_2 lead to the formation of a poorly crystallized product with an admixture of oxides [27]. It was observed that semiconductor properties of ReS_2 and $ReSe_2$ depend on the nature of the transport agent: *n*-type and *p*-type semiconductor crystals ReS_2 and $ReSe_2$ were obtained in case of bromine and iodine, respectively.

The use of selenium and tellurium melts to prepare TMD crystals with a size of ~1 mm was described in [28]. Gradual evaporation of chalcogen into the cold end of the ampoule lead to the formation of crystals $NbSe_2$, $TaTe_2$, $ReSe_2$ and chalcogen-mixed crystals $Nb(S_{1-x}Se_x)_2$.

Synthesis of TMD based micro- and nanomaterials

The methods of preparing TMD based micro- and nanomaterials can be represented by two groups: 1) "bottom-up", i.e. using molecular or atomic precursors, 2) "top-down", including the stage of exfoliation of crystalline objects.

"Bottom-up" synthesis of TMD nanomaterials. TMD materials of group 4-7 elements are prepared by various modifications of the CVD method since chemical vapor deposition provides reproducible synthesis of well-crystallized nanomaterials with controlled thickness and lateral dimensions. The sources of transition metals are usually their oxides or halides; the source of chalcogens are chalcogens as such or their organic compounds. Nanocrystals MS_2 (M = Zr, Hf) are successfully prepared using chlorides MCl_4 due to their low melting points (compared to those of oxides) and the absence of oxygen in the resulting products (ZrS_2 [29], HfS_2 [30]). Few-layer 3R–NbS_2 particles [31] (starting with monolayer ones) were prepared using Nb_2O_5 and sulfur in the presence of sodium chloride in the H_2/Ar atmosphere. Nanocrystals of NbS_2 and TaS_2 can also be obtained from corresponding metal pentachlorides MCl_5 and sulfur in a flow-type reactor in the presence of microcrystalline sodium chloride or h-BN particles used as the substrate (3R–NbS_2 modification is formed) [24]. When using metal oxides Zr, Hf, Nb, Ta, alkali metal halides are added; apparently, formation of metal oxohalides increases mass transfer during the synthesis [32] to increase the formation rate of TMD nanocrystals. Thin-layer crystals of disulfides of group 6 metals are commonly prepared using metal oxides (MO_3: M = Mo [33], W [34]) and sulfur (or hydrogen sulfide). Nanocrystals prepared from MO_3 oxides have impurities in the form of oxides, which is unacceptable for some applications, e.g. in optoelectronics. According to XPS data, using carbonyls $M(CO)_6$ (M = Mo, W) in TMD synthesis also leads to the formation of metal oxide impurities (e.g., in the synthesis of WSe_2 from $W(CO)_6$ and $(CH_3)_2Se$ [35]). In some works, molybdenum dichalcogenides were successfully prepared from molybdenum halides: for example, MoS_2 nanoparticles (NPs) were fabricated from $MoCl_5$ and S [36], $MoSe_2$ NPs were fabricated from $MoCl_5$ and $((CH_3)_3Si)_2Se$ [37]. WS_2 was prepared from hexafluoride WF_6 in an atmosphere of H_2S/H_2 plasma [38]. Few-layer samples ReS_2 can be obtained by CVD either from ammonium perrhenate and sulfur [39] (or hydrogen sulfide [40]) or from metallic rhenium. In the first case, the synthesis was carried out at a rather low temperature (460 °C), but the resulting ReS_2 nanocrystals had an admixture of rhenium oxide (the material was used in the catalysis of crude oil hydrosulfonation). The use of metallic rhenium in the synthesis requires high temperatures (> 1000 °C) as well as transport agent (bromine or iodine). The authors of [41] fabricated ReS_2 NPs at 700 °C by lowering the temperature in the course of the synthesis from an eutectic rhenium–tellurium mixture (1:6) with the melting point 430 °C. Nanomaterials of transition metal ditellurides are also prepared by CVD. Review [42] summarized the synthesis parameters of thin-layer samples of group 4-6 transition metal ditellurides MTe_2: such particles were mainly prepared from tellurium and metal oxides in the presence of NaCl, KCl or KI at 650-800 °C in an Ar/H_2 flow.

Few-layer TMD samples are prepared from various metal and chalcogen (usually, sulfur) sources, some of which have complex compositions. Thus, the authors of [43] obtained a series of microcrystalline NbS_2 films using atmospheric pressure chemical vapor deposition (APCVD) from $NbCl_5$ and several sources of sulfur ($(SiMe_3)_2S$, t-Bu_2S_2, t-BuSH, $HSCH_2CH_2SH$) at 250-600 °C. Depending on the sulfur-containing initial substance and the synthesis temperature, the obtained NbS_2 samples had two polymorphic modifications: 1T ($S(SiMe_3)_2$ or t-Bu_2S_2 at 500-600 °C) and 3R (t-BuSH or $HSCH_2CH_2SH$ at 500-600 °C). X-ray amorphous films NbS_2 and TaS_2 were prepared by thermolysis of aerosols of complexes $[M(St\text{-}Bu)_{5-x}(NMe_2)_x]$ (M = Nb, Ta) [44]. Films 2H–$NbSe_2$ were fabricated by APCVD at 600 °C using t-Bu_2Se and $NbCl_5$ in an atmosphere of nitrogen [45].

High vacuum conditions can be used to obtain metal and chalcogen vapors which form TMD NPs after being deposited on a substrate. Ultrathin epitaxial $NbSe_2$ layers were prepared on a Se-terminated GaAs(111) in a high-vacuum chamber in the temperature range 425-530 °C, and, depending on the synthesis temperature, the samples contained crystal modifications of $NbSe_2$ 2Hb+3R (420 °C and 500 °C) or 2Ha+2Hb (530 °C) [46]. Oriented monolayers $TaSe_2$ [43] were obtained on a gold surface upon simultaneous evaporation of selenium and tantalum at 600 °C; the growth of $NbSe_2$ layers was conducted at 300-600 °C [47].

Since CVD allows controlling the thickness of nanocrystals, and chemical compositions of their surface are very close to nominal formulas MQ_2, these thin-layer semiconductor crystals are considered promising in digital electronics and optoelectronics. Heterolayer crystals can be prepared by combining the multitude of studied TMDs. Since each material has unique electronic structures and properties, the fabrication of heterostructures could exhibit improved properties or even new properties compared to individual TMDs. The authors of review [48] discuss TMD heterostructures, their CVD synthesis and growth features, structure, and prospects for the use in nanoelectronics.

TMDs were also prepared in the form of inorganic fullerenes (IFs) and nanotubes. A series of multi-layer IF–MS_2 (NbS_2 [49], TaS_2 [50], MoS_2 [51], WS_2 [52], ReS_2 [53]) were synthesized in reactions of metal chloride vapors (MCl_4 or

MCl_5) with hydrogen sulfide at 550-750 °C and subsequent annealing in H_2S. Solvothermal synthesis of IF–$MoSe_2$ from ammonium molybdate and sodium selenite [54] and IF–WSe_2 from WO_3 and selenium vapor [55] was also reported. Solid solutions of NPs in the form of fullerenes can be prepared from initial substances containing another metal: $Mo_{1-x}Re_xS_2$ and $W_{1-x}Re_xS_2$ [23] and $W_{1-x}Nb_xS_2$ [49]. Besides, binary and doped TMDs were prepared in the form of nanotubes: e.g., MoS_2 and WS_2 nanotubes were obtained upon the decomposition of ammonium tetrathiomolybdate (or tetrathiotungstate) in hydrogen at 1000-1200 °C [56]; $NbSe_2$ nanotubes were prepared by irradiating $NbSe_2$ powder by a beam of electrons [57].

Solution methods for the preparation of TMD NPs include colloidal and sol-gel methods. A characteristic feature of such TMD syntheses is high temperature, for example, when annealing the resulting gel or when carrying out colloidal synthesis. In some cases, the size of TMD particles can be controlled using the sol-gel method. Thus, NbS_2 particles can be obtained from a mixture of $Nb(OEt)_5$ with benzenesulfonic acid (precipitate of niobium ethoxysulfide is formed) [58] or from the thiolate complex $Nb(2,6\text{-}Me_2C_6H_3S)_5$ whose solution is bubbled by H_2S (sol-gel stage) [59] and subsequent annealing at 700-800 °C in H_2S. When preparing NbS_2 microparticles, the synthesis temperature can be also diminished by using the colloidal method: 10-60 nm thick nanoparticles were obtained by the reaction of $NbCl_5$ with CS_2 in oleylamine at 280-320 °C. The authors of [60] described colloidal synthesis of a series of NbS_2 nanoparticles with various shapes (Fig. 1) from $NbCl_5$ solutions in mixtures of oleic acid and oleylamine with carbon disulfide at 300 °C. The shapes of the particles (mono- or oligolayers, plates, hexagonal nanocrystals, nanorods, and nanospheres) depended on the ratio of oleic acid, oleylamine, and CS_2.

TMD nanomaterials of group 6 elements can also be obtained by the sol-gel method. For the study as memristors, films of 2H–MoS_2 nanoparticles were prepared from ammonium heptamolybdate and acetamide as a source of sulfur in water in the presence of a stabilizer; the resulting gel was annealed in an atmosphere of argon at 300-400 °C [61]. Composites MoS_2/C synthesized by the sol-gel method are used as electrodes in lithium batteries [62]. $MoSe_2$ nanoparticles for the study as catalysts in the reaction of hydrogen evolution were prepared from $MoCl_5$ and diphenyl diselenide Ph_2Se_2 in an ethanol solution. The gel was mixed with carbon particles and annealed at 700 °C to obtain 200 nm large particles with a “core–shell” structure [63].

Since the sol–gel method includes a solution stage with the participation of molecular starting compounds, the salts containing various metals can be mixed before preparing the sol to obtain a dichalcogenide based solid solution. Work [64] is a logical development of the sol–gel synthesis with respect to TMDs, namely, preparation of doped dichalcogenides. The

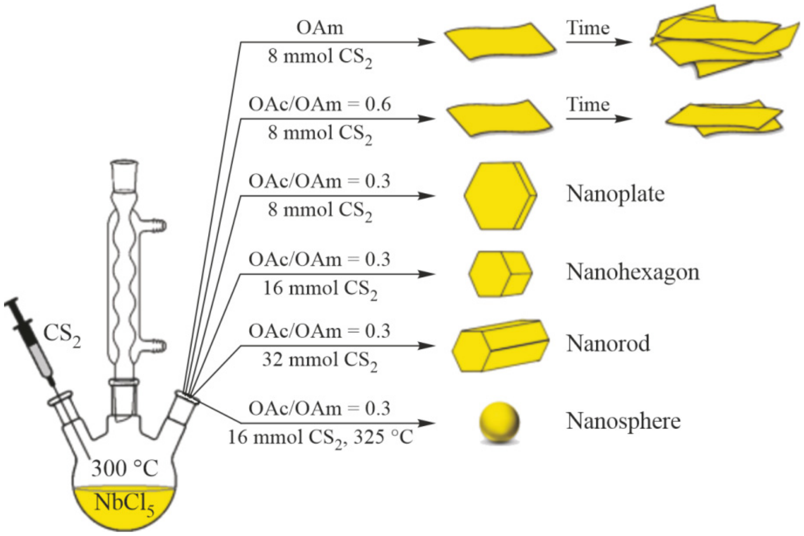

Fig. 1. Various forms of NbS_2 particles prepared from $NbCl_5$ and CS_2. The figure is cited from [60], ©ACS Applied Nano Materials, American Chemical Society, 2018.

authors synthesized doped compounds with several compositions: WS_2 doped with iron or molybdenum and MoS_2 doped with tungsten or rhenium. It was shown in [65] that MoS_2 nanoparticles with a thickness of 3-8 MoS_2 layers with a partial substitution of sulfur by nitrogen (the nitrogen content in different samples was 5.8-7.6 at.%) can be obtained from $MoCl_5$ and thiourea $CS(NH_2)_2$ and subsequent annealing at 650 °C.

"Top-down" synthesis of TMD nanomaterials. Exfoliation of TMDs intercalated with alkali metals (lithium, sodium, potassium) allows obtaining a solution with TMD monolayers [66] or with particles with some other number of layers (2, 3), depending on the order of the intercalate. Intercalate A_xMQ_2 (A is an alkali metal, Q is most often S) is placed in a liquid medium (for example, water) which interacts with alkali metal atoms to form hydrogen that helps to separate the MQ_2 layers from each other. There are many TMDs for which lithium and sodium (less often potassium or magnesium) intercalates have been studied: TiQ_2 (Q = S [67], Se, Te [68]), ZrS_2, $ZrSe_2$ [69], NbS_2, $NbSe_2$ [70], $MoTe_2$ [71], $MoSe_2$, WS_2 and WSe_2 [72], ReS_2 [73]. Most often, these TMDs are used as electrode materials in chemical current sources. Being exfoliated in the presence of a stabilizer, such intercalates can give high yields of solutions with monolayer samples. TMD samples obtained upon deintercalation in solution can serve as matrices for the assembly of new intercalates. Thus, MoS_2 monolayers stabilized in solution are used to prepare intercalates [74] with organic cations [75] and organometallic complexes [76]; some of them have been studied as electrocatalysts in the reaction of water splitting associated with hydrogen formation.

There is a progress in solution methods intended for the exfoliation of TMDs not subjected to chemical modification. Upon such exfoliation, the crystalline powder or TMD crystals are usually located in a liquid medium which promotes the formation of few-layer TMD particles. Similarly to other layered structures (graphite oxide, layered metal hydroxides, clays, etc. [77]), TMDs can exfoliate due to cavitation: emerging bubbles of the gas dissolved in the dispersion medium burst and create high-pressure and high-temperature regions in the space around them to destabilize the crystals of the substance. Dynamic simulations show that the collapse of a 4-5 nm bubble in an isopropanol–water mixture increases the surface temperature of the dichalcogenide (MoS_2) up to 3000 K and the pressure up to 20 GPa [78]. This effect creates a 10 GPa shear stress inside MoS_2 to cause crushing and exfoliation of the crystals. The most common ways to cause cavitation is sonication (with a frequency up to 3 MHz) or, to a lesser extent, boiling TMDs in a liquid dispersion medium. The nanoparticles resulting from such treatment show significant dispersion of lateral sizes (ten to hundreds of nanometers); the thickness of the particles can range from 2, 3 MQ_2 layers to several micrometers. Dispersion media for the preparation of TMD colloidal solutions can stabilize TMD NPs in solutions. The Hansen solubility parameter theory, which can be used to estimate the minimal dispersion energy, is used when choosing the dispersion medium with respect to TMDs [14]. Thus, for disulfides MS_2, efficient dispersion media are isopropanol, N-methylpyrrolidone, N,N′-dimethylformamide; for diselenides MSe_2 such dispersion media are ethanol and acetonitrile. For other media, stabilizers are used: pyrene for the stabilization of MoS_2 in ethanol [79], urea for the stabilization of a wide range of MS_2, MSe_2 and MTe_2 in water [80].

Synthesis of $M'MQ_2$ intercalates

The synthesis of intercalates and doped TMDs allows altering their electronic structure and, consequently, their physicochemical properties by stabilizing polymorphic modifications where TMDs are active in electrocatalysis (1T–MoS_2, WS_2), improving thermoelectric properties of TMDs, increasing the superconducting transition temperature, and other properties. When atoms M' are introduced into the space between the MQ_2 layers, the infinite layers acquire a negative charge. Table 1 summarizes the data on the synthesis and study of properties of group 4-6 TMD intercalates.

We first consider the self-intercalation phenomenon, i.e. formation of superstoichiometric compositions $M_{1+x}Q_2$ where metal atoms (group 4 or 5) constituting infinite MQ_2 layers also enter inside the interlayer space. A small number of interlayer metal atoms are usually arranged randomly but tend to get ordered for stoichiometric $M_{1.25}Q_2$. Thus, self-intercalate 2H–$Nb_{1.25}S_2$ with orderly arrangement interlayer niobium atoms ($\sqrt{3}a \times \sqrt{3}a$ lattice) was obtained by the reaction of niobium with hydrogen sulfide at 1290 °C [81]. The packing of sulfur layers is described as BBCC, and those of sulfur and niobium as …BABA*CACA**BA… The authors of [82] synthesized a series of self-intercalated selenides 2H–$Nb_{1+x}Se_2$

TABLE 1. Summary of the Synthesis, Structure, and Properties of Synthesized Intercalates M'_xMQ_2

Formula	Type	Synthesis method	Properties*	Ref.
1	2	3	4	5
Ni_xZrS_2 $x = 0.7$ and 0.12	1T	Ni, Zr, S St.mix. (≈ 900 °C)	Red shift of absorption edge. Ni in tetrahedral voids in the interlayer space	[90]
$Cu_{0.08}ZrS_2$	1T	Cu, Zr, S St.mix. (≈ 900 °C)	Red shift of absorption edge. Cu in tetrahedral voids in the interlayer space	
$M'ZrS_2$, M'=Fe, Cu; $x < 0.22$	1T	M', Zr, S (900-800 °C)	Red shift of absorption edge	[91]
Fe_xZrS_2 ($0 < x < 1$)	1T	Fe, Zr, S (900-800 °C)	Fe in tetrahedral voids. As x increases, parameter a gradually decreases; parameter c increases with increasing x up to 0.5 and then gradually diminishes. The data of magnetic measurement indicate the formation of $Fe_2^{2+}(Zr^{3+}S_2^{2-})$ clusters	[92]
$M'HfS_2$, M' = Fe, Cu; $x < 0.22$	1T	M', Hf, S (900-800 °C)	Red shift of absorption edge	[91]
$Ag_{0.1}HfS_2$, $Ag_{0.2}HfS_2$	2H	HfS_2 + Ag	Electrical resistivity decreases	[93]
$Ag_{0.1}HfSe_2$ $Ag_{0.2}HfSe_2$	2H	$HfSe_2$ + Ag	High mobility of silver ions	[94]
Cu_xHfSe_2 (x = 0.05, 0.10, 0.18)	-	$HfSe_2$ + Cu	Electrical resistivity increases; localization of charge carriers on Cu atoms; hopping charge transfer mechanism. Copper atom positions are disordered	[95]
Cr_xHfSe_2 (x = 0.05, 0.10, 0.25)	-	$HfSe_2$ + Cr	Electrical resistivity decreases, the type of conductivity is preserved. Paramagnetic above 2 K; the effective magnetic moment remains lower than expected for Cr^{3+}	[96]
Pd_xNbS_2 ($x < 0.23$)	2H	Pd, Nb, S (850 °C); CVT	XRD $Pd_{0.23}NbS_2$. Electrocatalytic properties of hydrogen evolution from an acidic aqueous solution were studied	[97]
$Sn_{1/3}NbS_2$	2H	Sn, Nb, S (900 °C)	XRD. Sn in a trigonal-prismatic voids between the layers. The semiconductor band gap (theor.) is 1.0 eV	[98]
Ga_xNbS_2, x ot 0.1 to 0.33	3R	Ga, Nb, S St.mix. (≈ 900 °C)	Ordered. The electrical resistance minima are found in the temperature range 20-60 K proportional to x; an order of magnitude decrease of electrical resistivity for $x < 0.25$	[20]
$Ag_{0.25}NbS_2$ $Ag_{0.6}NbS_2$	2H	Ag, Nb, S (800-1000 °C)	$Ag_{0.6}NbS_2$:Superstructure $2\sqrt{3}a \times 2\sqrt{3}b \times c$. Thermoelectric and magnetic properties were studied. The temperature dependence of electrical resistivity has an anomaly at 124 K	[100, 101]
Co_xNbS_2, x ot 0.2 to 0.55	2H	Co, Nb, S (1000 °C)	For $x = 1/3$, Co^{2+} ordering in the high-spin state and superstructure $\sqrt{3}a \times \sqrt{3}a$; For $x = 0.49$, metal–semiconductor transition	[102]
$Cu_{0.16}NbS_2$	-	Cu, Nb, S (970 → 940 °C)	EXAFS. Bond lengths within layers do not change	[103]
$Cu_{0.38}NbSe_2$	-	Cu, Nb, Se (850 → 750 °C)	EXAFS The length of the Se–Se bond decreases	

TABLE 1. (Cont.)

1	2	3	4	5
Ga_xNbS_2 (LT) $x = 0.125$, 0.25, 0.33	2H	Ga, Nb, S (1000 and 1150 °C) quenching	XRPD; pronounced ordering of Ga atoms for $x = 0.33$ (inside tetrahedral voids): $\sqrt{3}a \times \sqrt{3}a$. Temperature dependence of electrical resistance ($x = 0.25$): anomaly at $T = 45$ K	[99]
$Ge_{0.3}NbS_2$	$4H_c$	Ge, NbS_2 (1000-1050 °C)	XRD. Atoms Ge in octahedral positions. For $0.1 < x < 0.25$, superstructure $\sqrt{3}a \times \sqrt{3}a$	[104]
$Ge_{0.2}NbSe_2$	2H	Ge, Nb, Se, I_2 (1040 °C)	XRD. Atoms Ge in octahedral positions. For $x \sim 0.15$, superstructures $\sqrt{3}a \times \sqrt{3}a$ and $2a \times 2a$ were observed; for $0.25 < x < 0.33$, the superstructures were more pronounced; for $x = 0.5$, only $\sqrt{3}a \times \sqrt{3}a$ was observed	
Cr_xNbSe_2	-	Cr, $NbSe_2$ (800 °C)	$x < 0.25$: 2H–$NbSe_2$; cluster spin glass for $x = 0.25$: Cr atoms are ordered $x = 0.33$: soft ferromagnet, $T_c \sim 82$ K. The oxidation state of chromium is 4+	[105]
Fe_xNbS_2 ($x = 0.01$, 0.02, 0.04, 0.08)	-	CVT	$x = 0.01$: electrical resistance increased, CDW transition is suppressed. Magnetic moments of Fe are disordered (spin glass)	[106]
$Sn_{1/3}TaS_2$ $SnTaS_2$	2H	Sn, Ta, S (900 °C)	Photoelectron spectra	[107]
$Pb_{1/3}TaS_2$	2H	Pb, Ta, S (900 °C)	XRD. Pb in trigonal prismatic voids between the layers. The semiconductor band gap (theor.) is 1.3 eV	[98]
$Ag_{1/3}TaS_2$ $Ag_{2/3}TaS_2$	2H	Electrochem. Intercalation of Ag into TaS_2	The mobility of silver ions was studied	[108]
Mn_xTaS_2 ($x = 0.02$, 0.05, 0.1)	2H	CVT I_2 (990-900 °C)	Parameter c increases with x. Significant magnetocrystalline anisotropy; magnetic moments of Mn are oriented within the ab plane	[109]
$Ni_{0.05}TaS_2$	2H	Ni, Ta, S (800 °C) recrystallization from a NaCl/KCl melt	CDW transition is suppressed. The superconducting transition temperature increased up to 3.9 K	[110]
$Cu_{0.52}TaSe_2$	2H	CVT, Cu, Ta, Se, I_2 (895 °C)	XRD. Partial ordering of Cu in tetrahedral voids between the layers; superstructure $2a \times 2b \times c$ (space group $P\bar{6}m2$)	[111]
$Cu_{0.16}Ta_{1.08}Se_2$	2H	CVT, Cu, Ta, Se, I_2 (895 °C)	XRD. Cu and Ta are located in the neighbouring interlayer gaps to diminish the symmetry from $P6_3/mmc$ to $P\bar{3}m$	
Fe_xTaSe_2 $x = 0.05$; 0.12	2H	CVT, alloy FeTa + Se	Electrical resistivity increases with increasing x; the CDW formation temperature depends on x; paramagnetic materials	[112]
Pd_xTaSe_2, $0 < x < 0.15$	2H	Pd, Ta, Se (900 °C); crystals CVT, $SeCl_4$	$x = 0.09$, T_c=3.3 K. Electronic phase diagram as a function of x is determined	[113]
Pd_xTaSe_2, $0.01 < x < 0.08$	2H	Pd, Ta, Se (750 °C)	Parameter c increases up together with x. XRD for $x = 0.08$. $T_c = 4.2$ K for $x = 0.04$. The CDW state is suppressed with increasing x and disappears at $x = 0.06$	[114]
$Cu_{0.03}TaSe_2$	2H	Cu, Ta, Se, (CVT, I_2) (950 → 850 °C)	XRD. Cu atoms are disordered; The electronic structure was studied by X-ray spectroscopy	[115]

TABLE 1. (Cont.)

1	2	3	4	5
Cu_xTaSe_2 ($x = 0.05, 0.15$)	-	Cu, Ta, Se, (CVT, I_2) (950 → 750 °C)	T_c increases up to 2.6 K ($x = 0.15$)	[116]
$Cu_{0.15}TaSe_{2-x}S_x$ ($x = 0, 0.5, 1, 1.5$)	-	Cu, Ta, Se, (CVT, I_2) (950 → 750 °C)	Intercalation with copper along with partial substitution of selenium by sulfur increases T_c up to 3.7 K	
$Cu_{0.69}NbTe_2$	-	Cu, Nb, Te (850 °C)	Cu atoms are disordered in tetrahedral voids between the layers; Nb atoms form zigzag chains in the $NbTe_2$ layers; temperature-independent magnetism in a range 4 –300 K	[117]
In_xMoSe_2 ($x = 1/3, 2/3, 1$)	2H	CVT, In, Mo, Se (750 °C)	diamagnetic *p*-type semiconductors	[118]
$M'_{0.5}MoSe_2$ M' = Ga, In, Tl	2H	CVT, Mo + Ga_2Se_3, Mo + In_2Se_3, Mo + Tl_2Se (1000-950 °C)	diamagnetic *p*-type semiconductors. Electrical conductivity increases; the semiconductor band gap decreases	[119]
Cr_xMoSe_2 ($0.1 < x < 0.5$)	2H	$MoSe_2$ + Cr (electrolytically)	Magnetic properties were studied depending on *x*	[120]
Ni_xMoSe_2 ($0.2 < x < 0.6$)	2H	Deposition of Ni, Mo, Se vapors	Scenarios for the deposition of Ni, Mo, Se vapors associated with the formation of double compounds and intercalates Ni_xMoSe_2 were studied.	[121]

---

* Studied properties and their changes compared to initial TMDs as a result of intercalation.

Notes: St.mix. is stoichiometric mixture; T_c is the superconducting transition temperature.

($0.04 < x < 0.29$) in evacuated quartz ampoules at prolonged heating (800-1000 °C) followed by a long-term cooling or quenching at 0 °C. All obtained self-intercalates had larger parameters with than those of $NbSe_2$ (12.55 Å): from 12.56 Å ($x = 0.01$) to 13.02 Å ($x = 0.29$).

Among TMD intercalates, lithium intercalates (less often, intercalates of other alkali metals) seem to be the most popular ones thanks to the study of lithium batteries [7]. There is also a an impressive list of intercalates TiS_2, ZrS_2, NbS_2, TaS_2 with organic cations: amines, amides, phosphines [12], amino acids and polypeptides [83]; N containing organic rigid molecules MoS_2 [75, 84, 85]. We here consider M'_xMQ_2, where M' is a transition or post-transition metal. The most common approaches to the synthesis of intercalates M'_xMQ_2 are preparation from elements and interaction of TMDs with the intercalant metal or with its compound; the use of a transport agent e is also possible. Electrochemical intercalation is less common. The list of intercalant elements is quite wide and includes transition and nontransition metals of groups 4-10. For example, a large series of intercalates M'_xMQ_2 ($x = 1/3, 2/3, 1$) with four TMD matrices MQ_2 (M = Nb, Ta; Q = S, Se) with ordered positions In, Tl, Sn, Pb, Bi were prepared in two ways: by heating mixtures of elements at 700-900 °C and by keeping initial TMDs in the vapors of intercalant metals [86]. Atoms M' are in an octahedral environment, atoms M are in a trigonal prismatic environment, like in the initial 2H–MQ_2 matrices. Series M_xNbSe_2 (M = Bi, Sb, Pb, W, Ge) [87] was prepared by the reduction of salts containing intercalant cations, in organic solvents, and in the presence of crystalline $NbSe_2$. 2H–TaS_2 and 2H–$TaSe_2$ were intercalated by indium upon the diffusion of indium atoms from its bulky sample [88]. Finally, there is a "layer-by-layer deposition" of intercalates for the MoS_2 matrix when intercalate $LiMoS_2$ was exfoliated in a liquid medium, and intercalates M'_xMoS_2 were prepared by adding salts of M' = Fe [89], Cu, Ag, Cd, Hg, Pd, Pb [74].

Synthesis of doped TMDs

In doped compounds $M'_xM_{1-x}Q_2$ or MQ'_yQ_{2-y}, heteroatoms replace some atoms in the cationic or anionic subsystem of initial MQ_2. The methods for preparing doped TMDs depend on the form of the desired product (crystals, NPs, few-layer samples) and vary similarly to the methods of preparing binary TMDs. Crystals of doped TMDs are usually obtained by the formation of the TMD in the presence of from elements or compounds serving as the sources of dopant atoms; NPs are prepared using solution methods (sol-gel, solvothermal synthesis) (Table 2). In some works, doped few-layer TMDs are prepared by introducing atoms into defected sites of TMD samples. Substitution (doping) of atoms in both subsystems (cationic or anionic) can be isovalent or non-isovalent.

Isovalent substitution in the anionic sublattice. Chalcogen-mixed polycrystalline TMDs MQ'_xQ_{2-x} (Q = S, Se, Te) are prepared from stoichiometric mixtures of from elements or corresponding dichalcogenides at the synthesis temperatures of unsubstituted TMDs. The first syntheses of such TMDs date back to 1970. Sulfides and selenides usually form a continuous series of solid solutions for $0 \le x \le 2$: $WS_{(2-x)}Se_x$ [122], $ZrS_{2-x}Se_x$ [123], $ReS_xSe_{(2-x)}$ [124]; the substitution by tellurium leads to the formation of inhomogeneity zones [122].

Non-isovalent substitution in the anionic sublattice. It was shown that MoS_2 NPs with a thickness of 3-8 layers and partial replacement of sulfur by nitrogen (the nitrogen content in different samples ranged from 5.8 at.% to 7.6 at.%) can be obtained by the sol-gel method from $MoCl_5$ and thiourea $CS(NH_2)_2$ and subsequent annealing at 650 °C [65]. There is also an interesting method of preparing phosphorus-, oxygen-, and fluorine-substituted few-layer MoS_2 crystals from a plasma source of these atoms. The fabricated few-layer MoS_2 particles were doped with phosphorus [125] upon the interaction with a PH_3/He plasma; as a result, phosphorus atoms occupied defects in the sulfur sublattice on the surface of the MoS_2 particles. The measured current-voltage characteristics of obtained particles testified that the hole-type of doping. The authors of [126] reported that P doped 3.3 at.% MoS_2 (obtained by the treatment of MoS_2/C NPs by phosphorous acid at 400 °C) had increased electrical conductivity and somewhat improved catalytic properties in the hydrogen evolution reaction. In [127], the interaction of few-layer MoS_2 samples with O and F containing plasmas led to the introduction of oxygen (fluorine) ions into the samples so that the ions took some part of electron density from the MoS_2 layers, resulting in a hole-type doping of the latter. In a similar work [128], few-layer MoS_2 samples were etched by oxygen plasma to prepare monolayers, and it was shown that predominant formation of sulfur vacancies upon such treatment leads to electron doping of MoS_2 layers.

Isovalent substitution in the cationic sublattice. Isovalently substituted TMDs are known for 4-6 group metals. They are usually prepared from elements, but also by other approaches. For example, MoQ_2 (Q = S, Se, Te) was doped with tungsten in a series of works: solid solutions $Mo_xW_{1-x}Q_2$ were obtained by direct vapor transport from elements [129], a $MoQ_2 + WQ_2$ mixture [130], and from halides, e.g., by the interaction of a stoichiometric mixture $MoCl_5$ and WCl_6 with Na_2S [131] or $MoO_3 + WO_3$ oxides with a chalcogen Q [132]; few-layer samples on a substrate can be prepared by CVD [133] and low-temperature solution-phase [134] methods.

Non-isovalent substitution in the cationic sublattice. Non-isovalent substitution in zirconium and hafnium dichalcogenides are mainly studied by theoretical calculations. One example of experimental non-isovalent doping is TaS_2, for which products $1T - M'_xTa_{1-x}S_2$ were obtained from elements using doping by the following metals: Ti, Zr, Hf, [135], Cr, Mn, Fe [136], Co, Cu [137]. For M' = Co, Cu, quenching is needed to stabilize the metastable 1T form.

The MoS_2 nanoparticles doped with manganese [138] or iron [139] can be obtained in solvothermal syntheses from ammonium molybdates and sources of M' and sulfur (M' = Mn: manganese(II) acetate and CS_2; M' = Fe: iron(II) sulfate and cysteine). Doping MoS_2 with manganese is also possible using CVD [140]. MoS_2 doped with cobalt or simultaneously with cobalt and niobium was also synthesized by bombarding MoS_2 crystals by Co^+ and Nb^+ ions [141]. Cobalt doped crystalline MoS_2 was prepared also from elements by chemical vapor transport (CVT) [142]. A $Co_xW_{1-x}S_2$ layer [143] was grown by CVT on tungsten oxide microtubes to fabricate catalyst particles.

Doping MoS_2 with niobium can be carried out by the synthesis from elements: crystals $Nb_{0.005}Mo_{0.995}S_2$ [144] were prepared by CVT at the temperature range 1050-935 °C. The fraction of niobium atoms in the MoS_2 structure increases up to 15% (our work, JSC, 2018); metallic properties increase in all cases: electrical resistance decreases with increasing Nb content.

TABLE 2. Summary of the Synthesis, Structure, and Properties of Synthesized Doped TMDs

Formula	Type	Synthesis method	Properties*	Ref.
1	2	3	4	5
ZrSSe	2H	Zr, S, Se (CVT I_2) (900-850 °C)	Specific electrical resistivity decreases	[123]
$Ta_{1-x}M'_xSe_2$, (M' = Mo, W); $0.07 < x < 0.2$	3R	M', Ta, Se, 800 °C	$x = 0.1$ $T_c = 2$ K. Polymorph 2H changes to 3R	[147]
$Ta_{0.96}Ti_{0.04}S_2$ $Ta_{0.915}Ti_{0.085}S_2$ $Ta_{0.915}V_{0.085}S_2$	1T	-	13-atomic "stars" of metal atoms. Superstructure $\sqrt{13}a \times \sqrt{13}a$ is formed at Ti ~ 0.08	[148, 149]
$Ta_{1-x}M'_xQ_2$, Q = S, Se; M' = Fe, Co, Ni; $0.02 < x < 1/3$	1T	M', Ta, Q, (1000-800 °C)	Electrical resistivity increases at low temperatures; localization potential of doped ions is enhanced by CDW depends on T	[150]
$Ta_{1-x}Fe_xS_2$ (x = 0.01, 0.02, 0.03, 0.04, 0.05)	1T	Ta, Fe, S (CVT, I_2)	Lattice parameter a decreases with increasing x. T_c ~ 2.8 K (at $x = 0.02$). The C–CDW state is suppressed at $x > 0.01$. Seebeck coefficient changes its sign for $x = 0.03$ at 340 K. For $x > 0.04$, the Anderson localization sets in	[136]
$Ta_{1-x}Fe_xS_2$ (x = 0.02, 0.05)	1T	Ta, Fe, S (CVT, I_2)	SEM, ordered superlattice $\sqrt{13}a \times \sqrt{13}a$. The superlattice order degrades with increasing x; for $x = 0.05$, asymmetric 13-atomic "David-stars" were observed	[151]
$Ta_{1-x}M'_xQ_2$, Q = S, Se; M' = Ti, Zr, Hf, V, Nb	1T	M', Ta, S (900-1000 °C). Double heating of tableted solid solution at 900-1000 °C; 1 atm sulfur pressure; quenching	M' = Ti. The only stable 1T at $x >= 0.1$. CDW is observed at room temperature T for $x = 0.9$. Electrical resistivity decreases as x increases up to 0.15. M' = Zr ($x = 0.15$), Hf ($x = 0.085$). The electrical resistance increases more rapidly, the CDW transition is suppressed faster. M' = V (x = 0.085, 0.33), Nb ($0.04 < x < 0.6$). Diamagnetic behavior. M' are disordered, CDW transitions are suppressed	[135]
$Ta_{1-x}Ti_xS_2$ ($0 < x < 1$)	1T	Ta, Ti, S, 950 °C three weeks	XPS and SEM studies. Evolution between the existence of the CDW (TaS_2) and the presence of structural defects (TiS_2) depending on x	[152]
$Ta_{1-x}M'_xS_2$, M' = Hf (0.2, 0.3%), W (0.05, 0.1%)	1T	Ta, M', S (CVT, I_2)	Doping with tungsten suppresses the C–CDW state stronger than doping by hafnium	[153]
$Ta_{1-x}Hf_xS_2$ ($0.0003 < x < 0.069$)	1T	Ta, Hf, S St.mix. (920 °C), annealing in I_2+S (900 °C)	Point defects in the superstructure (up to 1% Hf). The CDW domain superlattice is smeared at x > 1%	[154]
$Nb_{1-x}Ti_xS_2$ $Nb_{1-x}Ti_xSe_2$	1T	Nb, Ti, S (or Se) (900-1000 °C), quenching	$Nb_{1-x}Ti_xS_2$ (x = 0.04, 0.06, 0.1) Transition from the incommensurate superstructure to the commensurate one $\sqrt{13}a \times \sqrt{13}a$ at $x = 0.04$, $T = 320$ K. $Nb_{1-x}Ti_xSe_2$ (x = 0.06, 0.1): weakly pronounced	[135]

TABLE 2. (Cont.)

1	2	3	4	5
			transition associated with the formation of CDW at 600 K (x = 0.1); ordered commensurate state at T = 335 K (x = 0.06)	
$TaS_{2-x}Se_x$ ($0.4 < x < 1.5$)	1T	St. mix. Ta, S, Se (900-1000 °C); quenching	Pronounced transition to C–CDW or NC–CDW state at T =352-473 K depending on x. The NC–CDW state is present up to x = 1. Totally commensurate state was observed for $x > 1$	
$Mn_{0.03}Mo_{0.97}S_2$	2H	Solvothermal synthesis from $(NH_4)_6Mo_7O_{24}$ and $Mn(CH_3COO)_2$ in the H_2O/CS_2 mixture (400 °C, 22 MPa)	The magnetic moment was 0.05 μ_B/Mn; it reversibly increases up to 0.11 μ_B/Mn upon lithium intercalation	[138]
$Mn_{0.017}Mo_{0.983}S_2$		CVD: S, MnO_2/NaCl, MoO_3 700 °C current Ar	Increasing activity of few-layer MoS_2 in the hydrogen evolution reaction	[140]
$Nb_{0.05}Mo_{0.95}S_2$ $Co_{0.04}Nb_{0.02}Mo_{0.94}S_2$		Bombardment of MoS_2 by Co^+, Nb^+ ions (20 keV)	$Nb_{0.05}Mo_{0.95}S_2$ Magnetization 1800 G at 5 K $Co_{0.04}Nb_{0.02}Mo_{0.94}S_2$ Coercive force 9 kOe at 100 K	[141]
$Co_{0.03}Mo_{0.97}S_2$	2H	Co, Mo, S (CVT 700 °C)	Increasing activity of the MoS_2 crystal in the hydrogen evolution reaction	[142]
$Mo_{1-x}Re_xS_2$ (x = 0.05, 0.10, 0.15, 0.20)	2H	Mo, Re, S st.mix. (CVT 850 °C)	Increased electrical resistance and diamagnetism due to the formation of Re_4 clusters	[146]
$W_{1-x}Nb_xS_2$ (x = 0.05, 0.1, 0.15), $W_{1-x}Nb_xSe_2$ (x = 0.01, 0.02, 0.05, 0.1, 0.15), $WS_{2-y}Se_y$ (y = 0.1, 0.2. 0.25), $W_{1-x}Nb_xS_{0.1}Se_{1.9}$ (x = 0.01, 0.02)	2H	W, Nb, S, Se st.mix. (CVT 850 °C)	Thermoelectric properties studied in the range 4.2-300 K More effective suppression of lattice thermal conductivity is possible upon double substitution	[155, 156] and our other works, including those in JSC
$W_{0.98}Nb_{0.02}Se_{2-y}S_y$ (y = 0.2, 0.3, 0.4, 0.5); $W_{1-x}Nb_xSe_{1.7}S_{0.3}$ (x = 0.02, 0.04, 0.06)	2H	W, Nb, S, Se st.mix. (CVT 820°C)	Thermoelectric properties studied in the range 4.2-650 K Replacing Se with S increases the mobility of charge carriers, thermal conductivity, and the Seebeck coefficient. $W_{0.98}Nb_{0.02}Se_{1.7}S_{0.3}$ ZT = 0.26 (T = 650 K). Replacing W by Nb increases the concentration of charge carriers and reduces their mobility.	
$W_{0.98}Nb_{0.02}Se_{2-y}Te_y$ (y = 0.2, 0.3, 0.4, 0.5)	2H	W, Nb, Te, Se st.mix. (CVT 820 °C)	Thermoelectric properties studied in the range 4.2-650 K. Double substitution in WSe_2 for composition $W_{0.98}Nb_{0.02}Se_{1.5}Te_{0.5}$ showed the maximum value of the power factor 444.4 $\mu W/m\cdot K^2$	

---

* Studied properties and their changes as a result of doping compared with unsubstituted TMDs. T_c is the superconducting transition temperature, SEM is scanning electron microscopy; st. mix. is the stoichiometric mixture.

The layers of Re doped MoS_2 (0.1 at.%, 0.20 at.%, 0.4 at.%) [145] were prepared by CVD from oxides ReO_3 and MoO_3 in an S/Ar flow at 700 °C. The photoluminescence spectra demonstrate that the band position depends on the doping density. MoS_2 with high rhenium content (up to 20%) [146] was prepared by CVT from elements. Contrary to the expectation that electrical conductivity would be increase by adding electron-rich rhenium (d^3 vs d^2 for Mo^{4+}), the crystalline samples showed stronger electrical resistance and diamagnetism due to due formation of rhenium clusters (HRTEM and magnetic measurement data), similarly to the clusters in the ReS_2 structure.

CRYSTAL STRUCTURE AND POLYMORPHS OF TMDs, MODIFIED (INTERCALATED AND DOPED) TMDs

Crystal structure and polymorphs of TMDs

The crystal structures of TMDs are packings of infinite $[MQ_2]_{2\infty}$ layers interacting with each other via van der Waals contacts $Q\ldots Q$. Inside the infinite layers, metal atoms are connected with six neighboring ones via bridging chalcogenide ions Q^{2-} located above and below the layer of metal atoms. TMDs can form several types of polymorphs depending on which coordination polyhedron of six chalcogen atoms contains the metal atom (octahedral or trigonal prismatic coordination) and on the arrangement of infinite $[MQ_2]_{2\infty}$ layers relative to each other. The main polymorphic modifications and structural types are shown in Fig. 2. Metal atoms occur in an octahedral environment of chalcogen atoms in the 1T modification (tetrahedral symmetry) and in a trigonal prismatic environment in 2H and 3R modifications. The structure of Re, Tc dichalcogenides slightly differs from other TMDs. It is known that disulfides and diselenides of rhenium and technetium belong to the triclinic crystal system [124], while $TcTe_2$ is monoclinic. Rhenium does not form layered ditelluride; rhenium telluride Re_6Te_{15} is a framework compound [157]. Dichalcogenides ReS_2 and $ReSe_2$ are isostructural, their rhenium atoms are surrounded by octahedra of six sulfur atoms and form metal clusters Re_4 linked in chains along axis *b* to form layers parallel to plane *ab*. Dichalcogenides TcS_2 and $TcSe_2$ are isostructural with each other. The structural motif of the layers is similar to the distorted one of ReS_2, but the packing of the layers is different. Technetium ditelluride $TcTe_2$ is monoclinic; the layers are parallel to the *ab* plane, and the packing resembles that of the high-temperature $MoTe_2$ form [158], but axes *a* and *b* in $TcTe_2$ are doubled.

The fact that the TMD crystal structure has polymorphs with different coordination environments of metal atoms and relative arrangements of infinite layers MQ_2 as well as the electronic structure of TMDs explain the appearance of a large

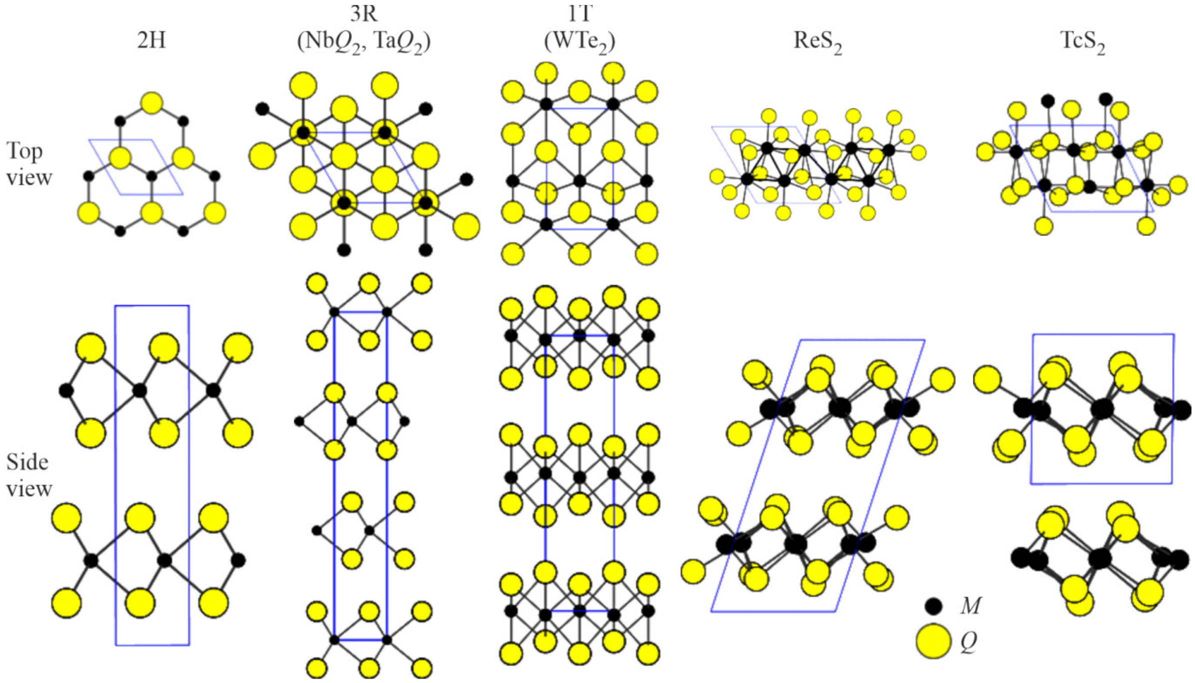

Fig. 2. Main TMD polymorphs.

number of works devoted to the modification of the electronic structure of TMDs to study them as possible functional materials.

Structure of M'_xMQ_2 intercalates

TMDs, being layered compounds, are characterized by weaker $Q\ldots Q$ interactions between the layers than covalent bonds within each layer. Therefore, there have been many successful attempts to intercalate different species into the interlayer space: from lithium atoms to organometallic complexes [159] and long organic molecules [12]. The structure of intercalates M'_xMQ_2 (M' is a transition or post-transition metal) considered in the present work shows a number of interesting features: relative arrangement of MQ_2 layers, ordering or the degree of ordering of intercalant atoms, and consequently, the intercalate order. These characteristics are related to the changes in the unit cell parameters of these compounds compared to initial MQ_2 which can be sometimes used to determine positions of atoms M'; more reliable data are obtained by XRD. As a rule, M' atoms in M'_xMQ_2 intercalates are located in ordered positions between MQ_2 layers after x reaches some value. Such situation is referred to as the unit cell increase (transformation) relative to initial MQ_2 parameters.

Series of intercalates with a variable content of the intercalated metal are of the greatest interest as far as studying the crystal structures and properties of such compounds. The authors of [105] prepared a series of intercalates Cr_xNbSe_2 ($0 < x < 0.5$). Chromium atoms occupied octahedral voids in the interlayer space; at $0 < x \leq 0.25$, the structure remained the same as that of initial 2H–$NbSe_2$. At $x = 0.25$, the ordering of Cr atoms and the $2a_0\times 2a_0$ superlattice (space group $P6_3/mmc$) were observed. At increasing chromium contents ($0.25 < x < 0.5$), another superstructure was found ($\sqrt{3}a_0 \times \sqrt{3}a_0$, space group $P6_322$). At $x > 0.33$, magnetic ordering occurs. According to the ^{53}Cr NMR and magnetic susceptibility data for $Cr_{0.33}NbSe_2$, the oxidation state of Cr is 4+, and there is 0.7 unpaired electrons per one Nb atom. Ordering of intercalant atoms was observed also in 2H–$Fe_{0.25}NbSe_2$ [160] and 2H–$Fe_{0.25}TaS_2$ [161].

Parameters a and c were varied in a series of intercalates M'_xZrS_2 ($0 < x < 1$) $M' = Fe$ [92] (also $M' = Co$, Ni, Cu [162]) containing iron atoms inside tetrahedral voids and exhibiting a relative arrangement of ZrS_2 layers similar to that in initial ZrS_2 (1T modification): while parameter a decreases slightly, parameter c increases at $x = 0.5$ (by 1%) and then gradually diminishes with increasing x. Band structure calculations and comparison of ZrS_2 absorption spectra with those of intercalates Fe_xZrS_2 suggest that intercalation increases the energy of bands p_z and d_{z^2} that are sensitive to the increase of the distance between ZrS_2 layers. According to the magnetic susceptibility data for Fe_xZrS_2 intercalates, their iron ions have a 2+ charge and, presumably, form clusters $Fe_2^{2+}(Zr^{3+}S_2^{2-})$. This system is unusual because iron atoms occupy tetrahedral voids in the interlayer space while a more common situation is octahedral or trigonal prismatic voids, which would be indicative of the 1T to 3R polymorph transition.

In a more difficult case, two types of atoms can be intercalated into the dichalcogenide matrix. In compound 6R–$Cu_xTa_{1+y}S_2$ ($x \approx 0.23$, $y = 0$, 0.06) [163], intercalated atoms of tantalum and copper are located in different interlayer spaces: tantalum and copper atoms occur in octahedral and tetrahedral voids, respectively. Intercalated atoms are partially ordered; 3D superlattice $2a_0\times 2b_0\times 2c_0$ was found. Interestingly, the following dependence of the crystallographic type of matrix on the composition and cooling rate during the intercalate synthesis was determined for $Cu_xTa_{1+y}S_2$ [164]: quenching the ampoule during the synthesis led to the formation of 2H–$Cu_xTa_{1+y}S_2$ ($0.29 < x < 0.34$, $0.28 < y < 0.30$), while slow cooling lead to the formation of 6R–$Cu_xTa_{1+y}S_2$ ($0.30 < x < 0.31$, $0.03 < y < 0.04$). Moreover, transformation of 2H–$Cu_xTa_{1+y}S_2$ into 6R–$Cu_xTa_{1+y}S_2$ was observed upon slow cooling. It was shown for Cu-intercalated $ZrTe_2$ that different crystallographic positions of copper atoms in polycrystalline compounds Cu_xZrTe_2 ($0 < x < 0.4$) are possible depending on temperature. In the temperature range 250-750 °C, Cu atoms occupy mainly tetrahedral positions in the interlayer space and mainly octahedral positions above 900 °C [165].

Most of the works devoted to the intercalation of TMDs reported charge transfer from the intercalant to the host layers while M' atoms acquire a formal positive charge and the negative charge is distributed over the MQ_2 layers. Depending on the nature of the host (i.e., on the electronic configuration of the metal in MQ_2 and the chalcogen nature), the acquired charge (electron density) can provoke changes in the structure of the host layers. Thus, in the intercalate $Cu_{0.69}NbTe_2$ [117], the structure type of the host is CdI_2, but the $NbTe_2$ sublattice is distorted with respect to the trigonal structure so that zigzag chains of niobium atoms are formed in these layers in the same direction within one layer; in this case, the formal electron configuration of Nb atoms is d^2. The authors of [11] prepared copper intercalates for ditellurides of group 5 metals: $Cu_{0.85}VTe_2$, $CuNbTe_2$, and $Cu_{0.89}TaTe_2$. Zigzag chains of V, Nb, Ta atoms were found in their crystal structures, which was confirmed by the calculations of the electron density localization function. A similar behavior would be expected for group 6 TMDs (MoQ_2, WQ_2) with d^2 configuration of metal atoms. In fact, the formation of zigzag chains of molybdenum atoms was observed in MoS_2 as it passed into the 1T modification (for example, upon the intercalation by organic cations [75].

Superstructures are often formed in group 5 and 6 TMD intercalates when at least some intercalant atoms in the interlayer spaces are ordered and superstructures $\sqrt{3}a \times \sqrt{3}a$ or $2a\times2a$ (a is the initial host lattice parameter) are formed (Table 2). Superstructure $\sqrt{13}a \times \sqrt{13}a$ is typical for the case of commensurate charge density wave. Such electronic structure rearrangements were observed both for niobium and tantalum dichalcogenides and for their intercalates (see more details below).

Structure of substituted dichalcogenides

Chalcogen-substituted TMDs form a series of solid solutions, and the structural type in the homogeneity zone is preserved. Sulfides and selenides usually form continuous series of solid solutions at $0 \le x \le 2$: $ZrS_{2-x}Se_x$ [123], ReS_xSe_{2-x} [124] $WS_{2-x}Se_x$ [122]. Lattice parameters a and c increase with increasing selenium content. Telluride-containing TMDs have discontinuities in the homogeneity region and crystallize in different structural types depending on x: $WSe_{2-x}Te_x$ crystallizes in the structural type 2H at $0 \le x \le 0.62$ and in the structure type WTe_2 ($Pnm2_1$) at $1.48 \le x \le 2.0$; $WS_{2-x}Te_x$ are similarly monophasic at $0 \le x \le 0.3$ and $1.8 \le x \le 2.0$ [122].

We now consider isovalent substitution in the cationic sublattice on the example of Mo–WQ_2. It is known that a continuous series of solid solutions 2H–$Mo_xW_{1-x}Q_2$ can be prepared for Q = S, Se [129, 166]. In the case of Q = Te, there are both pure 2H, 1T′, $T_d(\gamma)$ phases and the regions of their coexistence, depending on x, and the reported data vary greatly. Substitution of molybdenum atoms in $MoTe_2$ by tungsten atoms leads to the destabilization of phases 2H and 1T, and tungsten contents exceeding 34-37% lead to the formation of the orthorhombic $T_d(\gamma)$ phase. At the tungsten content 15-34%, both phases 1T and T_d coexist simultaneously; at the tungsten content < 15%, phase 1T is stable; and at the tungsten content < 4%, the 2H phase may exist [167-169]. In this case, according to [170], a low critical tungsten concentration of ~8% stabilizes the orthorhombic $T_d(\gamma)$ phase at room temperature, and the Fermi surface of this phase is similar to that of WTe_2.

Introducing the heteroatom while preserving the structural polytype affects lattice parameters according to Vegard's law: $Mo_{1-x}Nb_xS_2$, $W_{1-x}Nb_xS_{2-y}Se_y$ (our works, JSC 2017 and 2018), $M_xTc_{1-x}S_2$ [171], $Au_xRe_{1-x}Se_2$ [172]. Introducing Au atoms in the main $ReSe_2$ lattice slightly increases its lattice parameters and reduces the stability of the triclinic structure under pressure.

Sometimes the introduction of heteroatoms causes more significant changes. For example, phase 2H is destabilized and phase 3R appears after introducing 1% of Re atoms into the cationic sublattice 2H–WS_2 [173]. It was shown for $Re_xMo_{1-x}S_2$ that high concentration of rhenium atoms leads to the clustering of the latter [147].

PROPERTIES OF TMDs

Electronic structure of TMDs

Electronic structure of binary TMDs. The electronic structure of stoichiometric TMDs MQ_2 depends on the nature of the transition metal and the chalcogen and changes with the number of layers in the crystal so that these compounds can vary from wide-bandgap semiconductors to metals. The band structure of TMDs was qualitatively systematized as far as in 1970-80-x [177]. The evolution of the TMD band structure depending on metal can be schematically considered on the example of disulfides ZrS_2, NbS_2, and MoS_2 (Fig. 3) [174].

Group 4 TMDs (Ti, Zr, Hf) usually crystallize as 1T polymorphs. In ZrS_2 and HfS_2, chemical bonds have a significant ionic component, all *d* electrons of the transition metal are involved in the bonding with sulfur; therefore, it is reasonable to assume that the metal ions have the d^0 configuration, and the charge distribution corresponds to the $M^{4+}S_2^{2-}$ model (Fig. 3) [174]. Metal ions in these compounds occur in an octahedral environment of sulfur, and the crystal-field splitting of *d* orbitals gives a qualitative structure of the unfilled conduction band (Fig. 3) with predominantly d_{z^2} states forming the lower part of the conduction band. In turn, the valence band, which is formed mainly by *p* orbitals of sulfur, is located much lower on the energy scale; thus, both ZrS_2 and HfS_2 with a more pronounced ionic nature of bonding are relatively wide-bandgap semiconductors (~ 1.16 eV and ~ 1.44 eV, respectively [175]). Replacing sulfur with selenium and tellurium leads to a decrease in the ionic component of *M–Q* bonds decrease. The semiconductor band gap between the valence *p* band and the conduction *d* band is still large enough in $ZrSe_2$ and $HfSe_2$ (≈ 0.6-0.7 eV), but ditellurides already show an overlap between *p* and *d* bands equal to several tenths of electronvolts and, respectively, exhibit semimetallic properties [176].

Group 5 TMDs (V, Nb, Ta) form polytypes with trigonal prismatic and octahedral types of metal ion coordination. For 1T – structures , the presence of an additional *d* electron compared with group 4 TMDs, would have resulted in the d^1 metal configuration, i.e. partially filled *d* conduction band and, consequently, good metallic properties. However, special features of TMDs such as pronounced layered structure and, consequently, a quasi-2D electronic subsystem make possible the development of the Peierls instability whereby a superstructural modulation (charge density waves, CDW) is formed with such a period that an additional band gap appears at the Fermi level due to the increased unit cell size (see more details below). In contrast to quasi-1D chained compounds where the Peierls instability can make a system totally dielectric, structural modulation in quasi-2D TMDs affects only a part of charge carriers, and the very possibility of its formation strongly depends on the geometry of the Fermi surface. Among group 5 TMDs, 1T–TaS_2 and 1T–$TaSe_2$ have been found most strongly susceptible to superstructural distortions, and even at room temperature they exhibit only weak metallic properties.

Group 5 TMDs can be also prepared with trigonal prismatic coordination, usually with the 2H polytype. Even though this coordination increases the energy due to the Coulomb repulsion between negatively charged chalcogen atoms located directly above each other in the structure, the splitting of *d* levels of the metal ion in this configuration is such that the

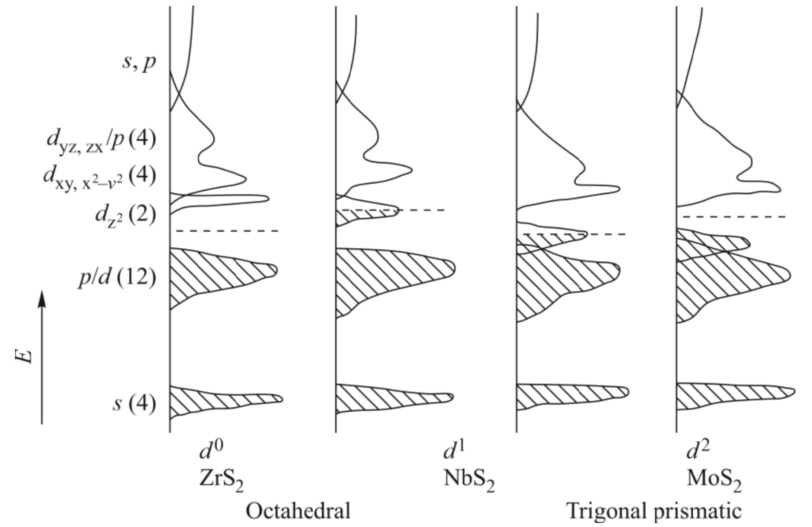

Fig. 3. Band structure of TMDs with octahedral and trigonal prismatic coordinations of metal ions; filled states are dashed; the dashed line shows the Fermi level. The figure is adapted from [174], ©Advances in Physics, Taylor & Francis, 1987.

energy of the d_{z^2} band additionally decreases and, therefore, the total energy balance favors the stabilization of the 2H structure (Fig. 3). Close energies of these two structural types make possible the existence of both 1T and 2H polytypes, for example, for TaS_2 and $TaSe_2$. A more complex topology of the Fermi surface of compounds with the 2H modification reduces the effect of superstructural modulations thus increasing their metallic properties. Some compounds, e.g. $NbSe_2$, are superconductors ([174] and references therein).

Group 6 TMDs usually form trigonal prismatic structures. Since metal ions have the d^2 configuration where the d_{z^2} band is separated from the bands formed by the rest of *d* orbitals (Fig. 3), MoS_2, $MoSe_2$, WS_2, and WSe_2 are semiconductors whose top of the valence band is formed by *p* and *d* electron levels. In contrast to diselenides and disulfides of Mo and W, ditelluride $MoTe_2$ can crystallize also in the polymorphic structure with distorted octahedral (1T′) coordination, and such strongly distorted 1T′ structure is the main one for WTe_2 [177-180]. Owing to the changes in the crystal field splitting of *d* bands in 1T′ and increased *p–d* hybridization, the band gap between valence and conduction bands in Mo and W 1T′ ditellurides disappears and these compounds become semimetallic [174, 177-181].

As the *d* shell of metal ions fills up to the d^3 level in group 7 TMDs such as Re dichalcogenides, electronic instability of the partially filled *d* band leads to structural distortions, a fourfold increase of the unit cell size, and formation of Re ion chains. As a result of the unit cell size increase, six completely filled electron subbands are formed to create semiconducting properties in ReQ_2 with a band gap up to ~1.4 eV [182-184]. Even though the reasons underlying the superstructure and dielectricity in 1T–TaS_2 and ReS_2 are similar (decreasing energy of *d* electrons), the superstructure in ReS_2 does not correlate with the shape of the Fermi surface and more resembles the Jahn–Teller distortion [182].

Although strong chemical bonds in the layered TMD structure are mainly formed within the layers, and the interlayer (van der Waals) interaction is relatively weak, the electronic structure of TMDs (except for group 7 TMDs) depends significantly on the crystal thickness and changes upon the transition from the bulk material to the monolayer (Fig. 4) [175, 185, 186].

For example, bulk MoS_2 is an indirect band gap semiconductor with a band gap of ~1.2-1.3 eV whereas a monolayer of this material is a direct band gap semiconductor whose band gap increases up to ~1.9 eV [185, 186]. Similar changes occur in the band structure of WSe_2 [190] thus providing possibilities of practical application of Mo and W dichalcogenides in semiconductor electronic devices to be used in electroluminescence and photoelectronics [187-189].

The fact that the band structure of Mo and W dichalcogenides changes from indirect band gap semiconductors and direct band gap semiconductor upon the transition to monolayers is more their specific feature rather than a universal property of TMDs. For example, photoemission data and theoretical calculations for Hf and Zr disulfides and diselenides show that they remain indirect band gap semiconductors when their band structures change upon the transition to monolayers [175, 190].

As the thickness of crystallites decreases on the way to monolayers, the band structures of conductive TMD compounds also change significantly. As an illustration, Fig. 5 shows calculated [191] Fermi surfaces for monolayers, bilayers, and bulk crystals of two $TaSe_2$ polytypes. It can be seen that the interlayer interaction in bilayers leads to the appearance of additional sheets of the Fermi surface, its complication, and eventually to the appearance of the “corrugated” along the *c* axis Fermi surface The corrugation, i.e. dependence of the Fermi surface on the wave vector along the axis *c* reflects the dispersion of electrons along the normal to the layers and the degree of electron transport anisotropy.

The band structure of TMDs is highly sensitive not only to interlayer interactions but also to distances between ions within each layer, which gives additional tool for modifying their properties. For example, it was shown for monolayers ZrQ_2 and $HfSe_2$ by theoretical calculations [192] that the band gap and related physical properties can be controlled using deformation. The band gap of the $HfSe_2$ monolayer is 0.6 eV, and calculations show that it should increase approximately linearly up to 1.34 eV with the tensile strain up to 8-9% [192]. In the case of ZrS_2, calculations show that the band gap increases upon the tensile strain up to 6% and starts decreasing after reaching the maximum value of 1.63 eV, while the compound should remain an indirect band gap semiconductor up to 10% deformation. In turn, the band gap decreases

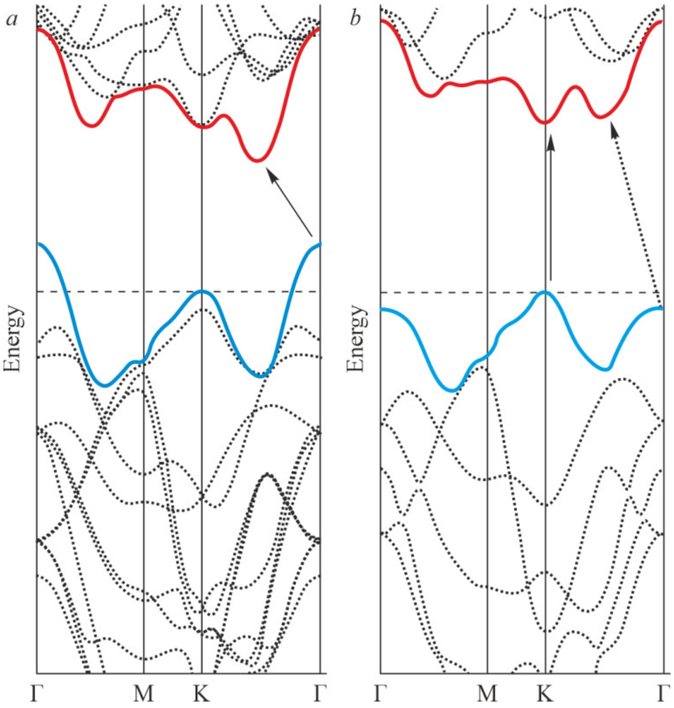

Fig. 4. Band structure calculated for bulk MoS_2 (*a*) and the MoS_2 monolayer (*b*); the arrows show the minimum energy distance between the valence band and the conduction band. In the case *a*, the electron wave vector changes upon the minimal energy transition, i.e. it is an indirect band gap semiconductor; in the case *b*, the transition does not affect the wave vector, i.e. it is a direct band gap semiconductor. The figure is cited from [186], ©ACS Nano, American Chemical Society, 2013.

monotonically as the strain increases upon lattice compression, the semiconductor–metal transition is expected at the 8% compression. By tuning the deformation one should be able to obtain required band gaps and band structure parameters (e.g., band degeneration [193]) that are optimal for the required physical property. For example, a 6% tensile strain should significantly improve thermoelectric properties of the ZrS_2 monolayer: the thermoelectric efficiency increases up to $ZT = 2.4$ at 300 K, which is 4.3 times higher than that of the initial system [194]. According to the theoretical calculations, conductive TMDs should also exhibit high strain sensitivity; for example, biaxial tensile strain in the plane of the $HfTe_2$ monolayer should lead to the metal–semiconductor transition, while uniaxial tensile deformation should preserve the metallic nature [195]. High elasticity and stability of thin TMDs layers make structural deformation an attractive method for modifying TMD properties. In particular, structural deformation can be obtained using epitaxial growth of MQ_2 layers on substrates with different lattice constants.

The sensitivity of TMD physical properties to weak deformations can be used to design various sensors and devices. For example, it was shown that deformation of a MoS_2 monolayer creates piezoelectric response which, in turn, changes the Schottky barrier on metal contacts to MoS_2 and, consequently, their electrical resistance. The electromechanical device based on MoS_2 monolayers with metal contacts demonstrated an unprecedented coefficient of sensitivity to deformations [196]. The change of conductive properties upon strain was also demonstrated on a polycrystalline sample of substituted molybdenum disulfide $Mo_{0.95}Re_{0.05}S_2$ [197].

Influence of intercalation. The most well studied class of intercalates are TMDs intercalated by alkali and alkaline earth metals M'_xMQ_2 ([10, 174, 198] and references therein), which have been widely studied since 1960s. Upon the intercalation by alkaline earth metals and, particularly, alkali metals, the latter occupy positions in the interlayer space and transfer significant part of their outer electron density to the MQ_2 layers, which is the main effect of intercalation on the

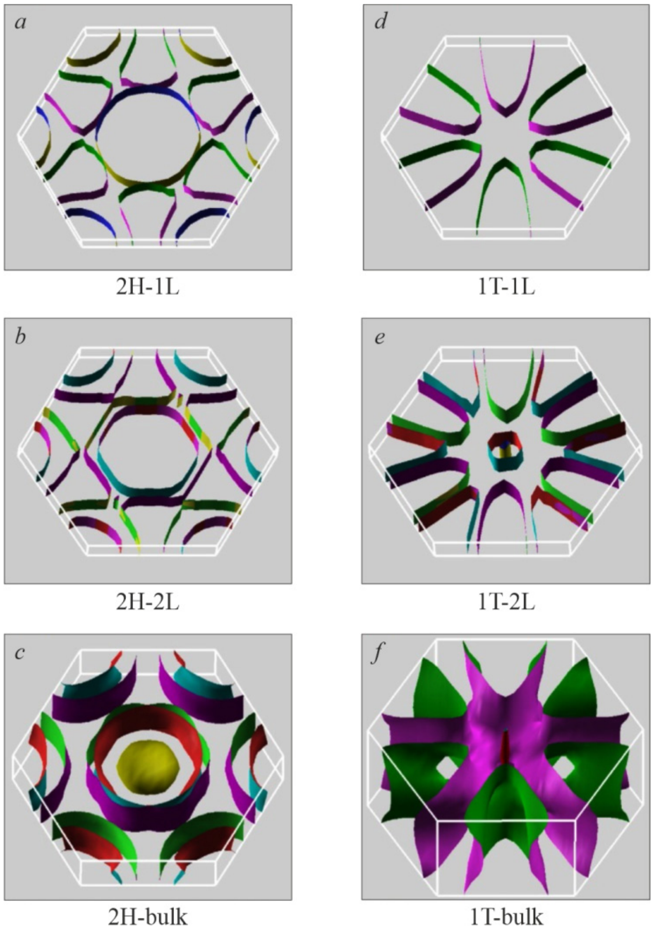

Fig. 5. Evolution of the Fermi surface of 2H–$TaSe_2$ (*a*-*c*) and 1T–$TaSe_2$ (*d*-*f*) upon the transition from monolayers (*a*, *d*) to bilayers (*b*, *e*) and bulk materials (*c*, *f*). The figure is cited from [191], adapted. ©Scientific Reports, Springer Nature, 2015.

physical properties of these compounds [10, 69, 70, 174, 198-203]. (Below, the changes in the degree of electron band filling as a result of changes in the compound's chemical composition or due to the effect of electric field will be referred to as "electron/hole doping"). In semiconductor compounds MQ_2 such as disulfides and diselenides of Hf, Zr, Mo, electron doping leads to the partial filling of the conduction band so that the compound acquires metallic and superconducting at low temperatures properties (Fig. 6) [10, 198, 199, 202]. In turn, intercalation by alkali metals and electron doping of conductive TMDs leads to the gradual conduction band filling and the metal–semiconductor transition [174].

The properties of TMDs intercalated with alkali metals were compared with those of few-layer samples doped with electrons directly by the electrostatic method (like in field effect transistors) and were found completely similar (Fig. 6) [198, 199, 204]. This is another confirmation that the main result of intercalation with alkali metals and alkaline earth metals is the appearance of a negative charge on MQ_2 layers, i.e. supplying the empty or partially filled conduction band with electrons. The fact that intercalated crystals of both group 4 (Hf, Zr) and Mo dichalcogenides (Fig. 6) exhibit superconductivity with close parameters to those of $NbSe_2$, NbS_2, TaS_2, TaSeS [174, 198] prove the similarity in properties of TMDs , that differ basically in the degree of *d* band filling.

The second most important consequence of intercalation of metals and, even more so of, large organic molecules into the TMD interlayer space is the decrease of interlayer interaction, which allows one to control the dimensionality of the system. For example, it was shown by angle-resolved photoemission spectroscopy (ARPES) that even the intercalation with potassium transforms the initial 3D electronic structure of bulk 1T–$HfTe_2$ into an almost purely 2D structure [205]. An even

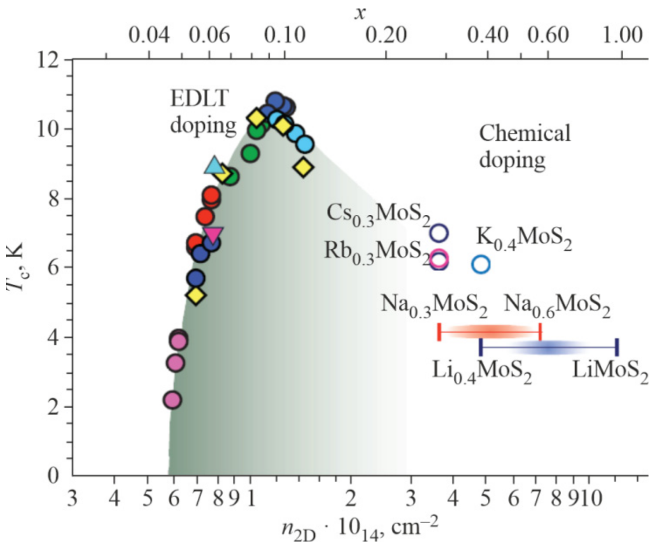

Fig. 6. Superconducting transition temperature of MoS_2 subjected to electrostatic electron doping (up to ~$2{\cdot}10^{14}$ cm^{-2}) and chemical intercalation by alkali metals. The figure is cited from [199], © Science, The American Association for the Advancement of Science, 2012.

more obvious transition to a purely 2D structure was observed in TMDs doped with organic molecules where the interlayer distance could reach 60 Å excluding any significant interlayer interaction [177]. By analogy with the change of the band structure upon the transition from a bulk crystal to a monolayer, the intercalation affects the band structure by increasing, in particular, the band gap between *p* and *d* bands and decreasing the *p-d* hybridization and the width of *d* bands. One most interesting fundamental result obtained for intercalated TMDs and confirmed later for monolayers is the demonstration of the possibility of purely 2D superconductivity [174, 199, 204, 206].

Structural distortions are another example of intercalation effects that are significant for physical properties. For example, deposition of sodium on the surface of $HfSe_2$ single crystals splits the valence band due to the deformations caused by intercalated sodium atoms, while the electrons from sodium atoms pass to the conduction band [207]. $HfTe_2$ and $ZrTe_2$ tend to form non-stoichiometric compounds whose nonstoichiometry is caused by Te vacancies [208, 209]. Upon the intercalation of $HfTe_2$ with lithium using gas-transport reaction, the effect of tellurium vacancies in Li_xHfTe_2 samples (whereby electrons of a defect remain localized near the latter) is weaker than the intercalation effect (whereby electrons from the lithium atom are transferred to the conduction band). Intercalation with Li slightly changes the lattice parameter *a*, while parameter *c* changes, at most, by 0.2 Å for $x = 0.5$ [210].

Intercalation of ReS_2 by alkali metal [211] and fluorine [212] atoms was studied by calculation methods. The calculations show that the changes in the electronic structure caused by alkali metal intercalation can be used to increase the catalytic activity of TMDs in hydrogen production reactions [211]. Fluorine intercalation also affects the band structure. According to the calculations, F atoms located above Re chains induce metallic states in the middle of the forbidden band, and the states are coupled ferromagnetically within Re chains and antiferromagnetically between the chains. In turn, F atoms between the Re chains should induce non-magnetic semiconductor states in the forbidden band [212].

Intercalates M'_xMQ_2 can be prepared also with 3*d* transition metals. In addition to the high-temperature synthesis, their specific feature is that ions intercalated in the interlayer space preserve electrons in their magnetic *d* shell when transferring outer electrons to the conduction band (Mn, Fe, Co, Ni acquire the 2+ state and V, Cr acquire the 3+ state [174]). As a result, the intercalates become ferro- or antiferromagnets with magnetic moments of intercalated ions interacting through superexchange interactions via M'–Q bonds or via conduction electrons of MQ_2 layers.

Changes in the electronic structure and properties of TMDs upon intercalation with organic molecules are determined by the same main factors as in the case of alkali metals: changed band fillings and decreased interlayer interactions, though with a different priority. Introducing organic molecules between the layers pushes MQ_2 layers apart thus turning them almost into the monolayer state with the corresponding changes in their electronic structure, while the changes in the degree of band filling are significantly weaker compared to alkali metals and depend on the ability of a particular intercalated molecule to transfer electron density or to withdraw it from the MQ_2 layer [174].

Effect of cationic and anionic substitutions on the electronic structure. Isovalent substitution of chalcogen atoms in the anion sublattice of dichalcogenides decreases the band gap in the series S → Se → Te [213, 214]. In the case of $HfSe_{2-x}S_x$, the band gap decreases with decreasing sulfur content, independently on chalcogen positions in the calculated structure [215].

The band gap also depends on the substitutions in the transition metal sublattice. For example, isovalent substitution of molybdenum for tungsten in $Mo_xW_{1-x}Se_2$ ($0 \le x \le 1$) leads to the formation of a solid solution where the optical band gap systematically changes depending on the composition [216]. In turn, non-isovalent cationic substitutions have a more complex effect that strongly depends on the nature of the dichalcogenide and the dopant. For instance, band structure calculations show that doping monolayer HfS_2 with different atoms can lead to a) hole doping and the Fermi level shift in the valence band, e.g. upon doping with La, Ce, Pr, Gd, Tb, Dy, Ho, Lu [217]; b) appearance of new states in the forbidden band upon doping with Nd, Pm, Sm, Eu, Er, Tm, Yb [217] as well as by transition metal atoms [218, 219] and P, As atoms [220].

The effect of substitution of rhenium atoms in rhenium disulfide and rhenium diselenide by metal atoms (V, Cr, Mn, Fe Co, Nb, Mo, Ta, W) on the band structure was studied by calculation methods in Refs. [221, 222]. In the case of dilute solutions, the least energy favorable dopant is Co both for rhenium disulfide and for rhenium diselenide; Ta is most energy favorable for ReS_2, and Nb for $ReSe_2$. It was shown that the band gap decreases significantly for all the studied dopants, with the exception of Mn. It is predicted that the electronic structure of ReQ_2 compounds doped with Cr, Fe, and Co is to be unstable with respect to spontaneous spin polarization; as a result, the ground state becomes ferromagnetic thus making these compounds 2D ferromagnetic semiconductors that can be possibly used in spintronics. Ferromagnetism of iron-doped ZrS_2 was demonstrated experimentally [223].

According to the calculations [223], doping a TcS_2 monolayer with transition metals Sc, Ti, V, Cr, Mn, Fe, Co, Ni, Cu, Zn leads to the formation of additional states in the form of sharp peaks near the host's valence band or conduction band due to the electronic levels of introduced atoms. In general, the band gap decreases: it reaches the smallest value (0.03 eV) when Tc is substituted by Fe, then by Cr (0.07 eV), Mn (0.14 eV), Co (0.15 eV), Sc (0.18 eV), Zn (0.22 eV), Cu (0.28 eV), Ni (0.35 eV), V (0.44 eV), and the largest value is reached for Ti (0.62 eV) [223].

Experimental studies of $Mo_xRe_{1-x}S_2$ single crystals ($x \le 0.01$) have shown that doping ReS_2 with a small amount of molybdenum leads to the formation of deep impurity levels, which has almost no effect on the magnitude of the indirect band gap between the valence band and the conduction band, but diminishes the mobility of charge carriers and, consequently, decreases the electrical conductivity [224]. Optical studies of single crystals $Nb_{0.01}Re_{0.99}S_2$ [225] also showed that the introduction of niobium into the ReS_2 lattice only slightly decreases the indirect band gap.

In the case of niobium and tantalum dichalcogenides, doping leads to additional changes due to the existence of CDW regions on the phase diagram (see below) and superconducting states. For example, in 1T–TaS_2 doped with copper (1T–$Cu_xTa_{1-x}S_2$, homogeneity region $0 \le x \le 0.25$), copper in the Cu^{+1} state, similarly to some other doping atoms of higher valencies, leads to the Anderson localization of charge carriers remaining after the CDW formation; as a result, the electrical resistance increases strongly and Curie paramagnetism emerges at low temperatures [137]. Substituting tantalum in 1T–TaS_2 with titanium (having one *d* electron less) changes the concentration of charge carriers and, respectively, the CDW period determined by the Fermi surface geometry. However, substituting Ta by Hf does not affect the CDW period [154]. Instead of changing the concentration of charge carriers, the Hf ion (which has significantly higher energies of *d* orbitals) creates a point defect with a hole localized near the ion. Thus, the effect of Hf ions on the CDW is that they cause spatial pinning of the charge density wave thus preventing the CDW to transform from the incommensurate state into the commensurate one, broadening the transition, and lowering its temperature [154].

CDW ordering

The instability of the metallic state of 1D conductors, which was predicted by Peierls in 1930s and experimentally confirmed by numerous studies of quasi-1D chain compounds, is necessarily associated with a structural distortion with wave vector $\mathbf{q}$ twice the Fermi wave vector ($\mathbf{q} = 2\mathbf{k}_F$) [226]. Such a structural distortion in 1D conductors leads to an increase in the unit cell size and the opening of the gap exactly at the Fermi level, with the decreased energy of occupied electronic states due to the band gap being the driving force of the structural transition. In 1D systems, the Fermi surface is two planes separated by a distance of $2\mathbf{k}_F$, which are perfectly superimposed by the CDW wave vector $\mathbf{q} = 2\mathbf{k}_F$; as a result, the emerged band gap covers the entire Fermi surface, and the compound becomes dielectric. More generally, the appearance of the Peierls instability and the CDW in compounds that are not 1D conductors is due to the presence of significant flat areas of the Fermi surface which can be superimposed using some translation vector $\mathbf{q}$. Historically, TMDs were found to be most suitable objects for the studies of CDW and related phenomena in 2D systems [227]. The Peierls instability and CDW formation are clearly manifested in dichalcogenides MQ_2 with the 1T structure, whose Fermi surfaces have quite a simple structure with large flat areas (Fig. 7*a*).

Fig. 7*a* schematically shows the Fermi surface of 1T–TaS_2 (and 1T–$TaSe_2$) formed by six electronic “pockets” having large nearly flat areas. The appearance of flat Fermi surface areas in TMDs is is directly related to the weakness of the interlayer interaction, i.e. their quasi-2D nature which makes the electron dispersion along the *c* axis negligible, while the Fermi surface very weakly depends on the wave vector components along axis *c* (line LM in Fig. 7*a*). Flat areas of electronic pockets can be superimposed by the translation vector directed along lines ΓM and ΓK (Fig. 7*b*), but in the first case flat areas of four pockets out of six are superimposed [227]. Detailed electron diffraction experiments showed that 1T–TaS_2 and 1T–$TaSe_2$ always exhibit superposition of charge density waves with three vectors $\mathbf{q}_i$ rotated by 120° relative to each other; as a result, a periodic superstructure $\sqrt{13}a \times \sqrt{13}a$ is formed and the unit cell size in the plane increases by 13 times (Fig. 8*a*). In fact, such superstructure is a result of three CDWs with vectors $\mathbf{q}_1$, $\mathbf{q}_2$, $\mathbf{q}_3$ formed in individual TaS_2 monolayers packed in the crystal as repeating stacks (the unit cell triples along axis *c*) [227, 228]. Such CDW superposition allows encompassing maximum of the initial Fermi surface and excluding the maximum fraction of charge carriers from the conduction so that the electrical resistance of 1T–TaS_2, for example, increases by dozens of times (Fig. 8*b*).

Being optimal with respect to the Fermi surface topology, the CDW periodicity does not necessarily imply commensurability of the resulting wave with the crystal lattice. However, in the case of an incommensurate CDW

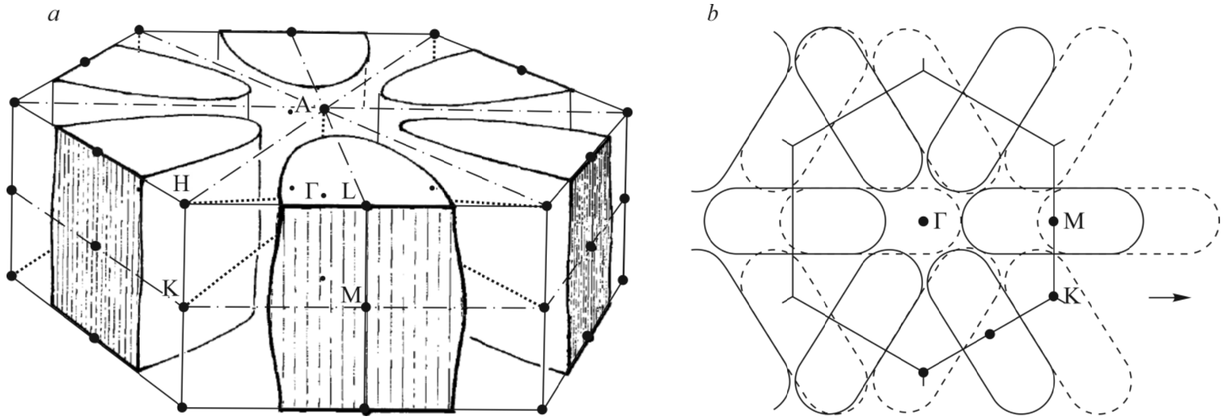

Fig. 7. Fermi surface of 1T–TaS_2 [230] formed by six electronic “pockets” with a close to cylindrical shape (*a*); displacement of the Fermi surface by vector $\mathbf{q}_1$ directed along axis ΓM resulting in the superimposition of flat areas of four out of six electronic “pockets” (*b*). The figures from [227] are adapted, ©Advances in Physics, Taylor & Francis, 1975.

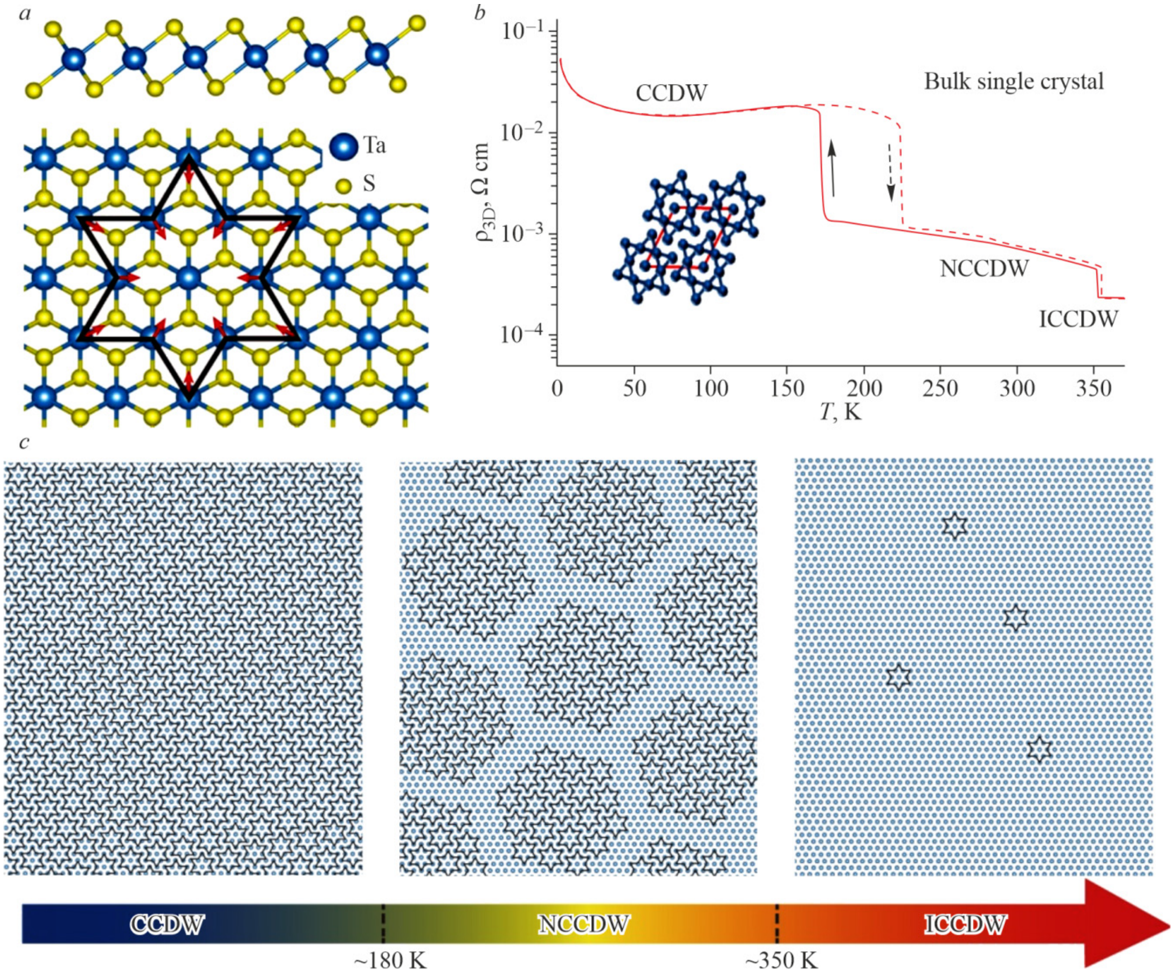

Fig. 8. Structure of 1T–TaS_2 with indicated CDW induced local ionic displacements: 12 ions of a cluster shift to the central one to form a periodic $\sqrt{13}a \times \sqrt{13}a$ [229] superstructure (*a*); temperature dependence of the electrical resistance of TaS_2 single crystal showing two stages of commensurate CDW (CCDW) formation with the transition from the incommensurate CDW (ICCDW) to the nearly commensurate CDW (NCCDW) phase at ~355 K and the first-order phase transition at ~200 K to the CCDW phase [230] (*b*); crystal structure evolution with varying temperature: asterisks indicate the clusters where the CDW period is commensurate with the crystal lattice [229] (*c*). The figure is compiled from works [229], ©Chinese Physics B, IOP Publishing, 2019 and [230], ©Scientific Reports, Springer Nature, 2014.

(IC–CDW), spatial positions of the maxima of CDW electron density do not coincide with positively charged ions, thus resulting in a loss in the Coulomb interaction energy. As a result, CDWs in most cases undergo significant evolution with temperature changes: (a) at high temperatures (above 500-600 K), the initial Fermi surface with no signs of CDW can be observed, (b) at lower temperatures, IC–CDW with a weak lattice response appears, (c) the tendency to minimize the separation between the charges of the electron density wave and the ion core changes the CDW period so that the CDW is adjusted to the crystal lattice, i.e. transition to the commensurate CDW state (C–CDW) at T_d takes place. In particular, such evolution was observed for 1T–$TaSe_2$ [227] where the CDW wavelength decreases by ~5% to adjust to the lattice. Sulfide 1T–TaS_2 shows a more complex CDW evolution. Instead of a direct transition to the C–CDW phase, 1T–TaS_2 first demonstrates a transition to nearly commensurate phase (NC–CDW) at ~355 K, and totally commensurate CDW is established only at ~200 K (Fig. 8*b*, *c*) [227, 229, 230]. In the NC–CDW phase, a quasi-periodic superstructure is formed from the domains of commensurate CDW (Fig. 8*c*): inside the domains, the CDW phase adjusts to the lattice to provide the maximum possible dielectric state, and the excess electron density is pushed off to the domain boundaries where the metallic state is preserved [231].

In other polytypes such as 2H and 4Hb, the CDW formation is complicated by a more complex Fermi surface which decreases the transition temperature to the CDW phase and diminishes its influence on electron transport characteristics. However, these polytypes preserve the same characteristic features of CDW formation. For example, in 2H–TaSe$_2$ at $T_{\mathrm{ICCDW}} \sim 120$ K, IC–CDW with a similar set of three wave vectors $\mathbf{q}_i$ appears [227, 232, 233] and passes to the commensurate state at ~90 K. Similarly to 1T–TaS$_2$, the CDW adjustment to the lattice proceeds through the formation of commensurate domains and the expulsion of "excessive" electron density (hindering the commensurability) to the domain boundaries. The only difference is the domain topology, which has a shape of stripes in 2H–TaSe$_2$ [232, 233].

Sensitivity of the band structure to polymorphism (packing of layers in the crystal) suggests a rich variety of electronic states in TMDs. An X-ray microdiffraction study of thin (7-36 nm) crystalline plates prepared by mechanical exfoliation of a bulk single crystal 2Ha–TaS$_2$ [234] revealed a number of polymorphs, including those not observed in bulk samples. All the polymorphs had significantly different properties with the CDW transition temperature ranging from 0 K to 300 K; depending on the polymorph, the electrical resistivity could increase or decrease with the CDW formation [234].One regularity exhibited by the TMD series is increasing temperature of transition to the commensurate CDW phase as the chalcogen atom is replaced by a heavier one: this is due to the changes in the phonon spectrum (CDW adjustment to the lattice is caused by the electron-phonon interaction) [227].

The main method of direct CDW observation is X-ray and electron diffraction allowing one to detect and determine parameters of lattice superstructures [227, 228]. Significant ionic displacements by CDW, e.g. Ta ions in the C–CDW phase in 1T–TaSe$_2$, makes it possible to directly observe the ionic superstructure in real space using high-resolution transmission electron microscopy [235].

After clarifying the basic principles of CDW formation in TMDs, extensive research has been undertaken to develop the methods for the control of CDW and transitions between its various states, since the possibility of obtaining and controlling various exotic electronic states provides possibility of their practical use, in particular, in nanoelectronics.

The most obvious way to influence a CDW state is to change the concentration of charge carriers in the sample using intercalation, cationic substitutions, electric field applied along or across the layers , and optical excitation [229-231, 234, 236, 237]. Changes in the concentration of charge carriers affects the topology of the Fermi surface and, consequently, affects the possibility of superimposing the flat regions of the Fermi surface to form the CDW and modify the superstructure vectors required for such a superimposition [174, 227]. The relation between the wave vector of the IC–CDW superstructure and the degree of conduction band filling was visually demonstrated for samples 1T–Ta$_{1-x}$Ti$_x$Se$_2$ where the wave vector of the CDW superstructure perfectly fitted dependency $q^2 \propto (1-x)$ from $q^2 \sim 1/13$ at $x = 0$ to $q^2 \sim 1/100$ at $x = 0.9$ [227], i.e. a tenfold decrease of conduction band filling upon the substitution of 90% Ta by Ti (Ti does not supply electrons to the conduction band) caused almost as many times increase of the superstructure cell's size.

Whereas the appearance and periodicity of IC–CDW are determined almost solely by the Fermi surface topology, the CDW transition to the nearly commensurate state and, even more so to the commensurate state is related to the interaction of the electron wave with the lattice. Even small changes of the IC–CDW wave vector $\mathbf{q}$ can significantly affect the ability of the CDW to adjust its period to the crystal lattice period. Consequently, the temperature of CDW transition to nearly commensurate state and commensurate states is extremely sensitive to any influences affecting the Fermi surface topology and the IC–CDW wave vector. For example, transition to the C–CDW state in 1T–TaS$_2$ is easily suppressed by the electric field applied in the field-effect transistor geometry and causing hole doping [230, 231]. Changes in the Fermi surface topology upon the transition to thin crystallites or under pressure enhancing the interlayer interaction also significantly affect the temperature of CDW transition to the commensurate state. In 1T–TaS$_2$ crystals, the NC–CDW to C–CDW transition disappears at a crystal thickness less than 30 nm, while transition IC–CDW to NC–CDW survives at least up to 7 nm [230]. Vice versa, in the diselenide crystal of 1T–TaSe$_2$ the temperature of CDW transition to the commensurate state increases with decreasing film thickness and reaches 570 K for a thickness of 3 nm (about 100 K higher than in bulk crystals) [238].

The impurity potential due to ionic substitutions or structural defects relatively weakly affects the appearance of IC–CDW but can easily suppress CDW transition to the commensurate state. When trying to adjust its phase to the chaotic

Coulomb potential of impurities, CDW breaks down into fragments and can no more form a wave that would be commensurate with the lattice. In titanium doped crystals 1T–$Ta_{1-x}Ti_xS_2$, the transition temperature to NC–CDW decreases with a rate of ~10 K/at.%, while the transition to C–CDW is totally suppressed already at $x = 0.5\%$ [230]. Doping with copper in 1T–$Cu_xTa_{1-x}S_2$ also suppresses CDW transition to the commensurate phase [137].

Most interesting is the possibility of rapid and reversible impact on the CDW state in TMDs. This possibility is provided by the above mentioned charge doping of thin crystallites or monolayers by a perpendicular electric field in the field-effect transistor configuration. In fact, hole doping of crystals with C–CDW removes electrons from the static commensurate wave, and the CDW breaks down into commensurate domains separated by domain boundaries [231]. The percolation network of domain walls accumulating the introduced holes provides an integral metallic state of the sample, similarly to the NC–CDW state (Fig. 8). It was found out that the same effect can be achieved by applying electric field along the layers [237]. It takes several picoseconds for a current pulse passing through a layer to transform the C–CDW into a set of nanodomains separated by conducting boundaries (Fig. 9), i.e. it switches the crystal from the dielectric state into the metallic state. After the passage of the current pulse, the conductive state may preserve for quite a long time, depending on temperature. Similar metastable conducting states can be obtained in thin (< 60 nm) 1T–TaS_2 crystals by rapid cooling of nearly commensurate CDW states to temperatures below 100 K [230].

An effect similar to charge doping can be achieved by irradiating a thin crystal with a femtosecond laser pulse [236, 239]. The irradiation-induced conductive state in 1T–TaS_2 turned out to be long-term stable below 60-80 K [236]. Super fast switching [239], several orders of magnitude change of electrical conductivity, and long-term stability (at low T) make effects related to the switching of CDW states highly attractive for applications. At higher temperatures, where the lifetime of the conducting state decreases to the nanosecond level, switching the CDW state in TMD nanolayers can be used to create highly sensitive bolometers, i.e. broadband radiation detectors [229, 240, 241].

The authors of [242] demonstrated the possibility to "draw" conductive nanogrids on a thin 1T–TaS_2 crystal existing in the insulating ground state by using voltage pulses from the tip of a scanning tunneling microscope to transform the CDW into a metastable incommensurate state.

From viewpoint of fundamental science, of considerable interest is the influence of CDW on the appearance of superconductivity in TMDs, in particular, in 2H–$NbSe_2$, 2H–TaS_2, and 2H–$TaSe_2$ where coexistence and competition of CDW and superconductivity were observed [229, 243]. For example, the temperatures of CDW and superconductivity occurrence in 2H–TaS_2 are $T_{\mathrm{CDW}} = 78$ K and $T_c = 0.8$ K. In 3R–$TaSe_2$, superconductivity with $T_c = 1.6$ K was observed along

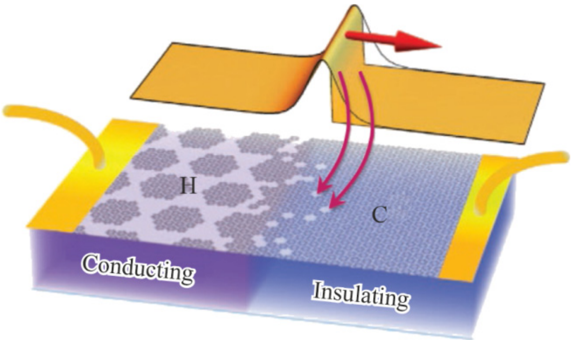

Fig. 9. Schematic illustration of the changes in the CDW state in a 1T–TaS_2 nanocrystal under the action of a current pulse along the layers: the injected charge carriers at the pulse front transform the dielectric state of C–CDW into the metastable conducting state (Hidden CWD) consisting of C–CDW nanoclusters separated by conducting domain boundaries. The figure is cited from [237], ©Nature Communications, Springer Nature, 2016.

with a weak CDW transition [244]. The maximal $T_c = 7$ K was observed in 2H–$NbSe_2$ [245]. The charge density wave and superconductivity compete for the areas of the Fermi surface where the dielectric or superconducting band gap is to be formed. However, Fig. 6 shows that the maximum concentration of charge carriers neither facilitates the establishment of the superconducting state; the dependence of the superconducting transition temperature on the charge carrier concentration has a characteristic dome-like shape. Apparently, parameters required for the superconducting state can be optimized by affecting the CDW parameters. As discussed above, intercalation and cationic substitutions suppress C–CDW, and 2H–Cu_xTaS_2 single crystals with low concentrations of intercalated copper become superconductors ($T_c = 4.2$ K at $x = 0.03$) [246], but no superconducting transition is observed at high concentrations of intercalated copper. With the suppression of CDW in Na_xTaS_2 crystals , T_c increases and reaches 4.4 K for $Na_{0.1}TaS_2$ [247]. In the series of Pd_xTaS_2 samples ($0.01 \le x \le 0.08$), the maximum value of $T_c = 4.2$ K is reached in $Pd_{0.04}TaS_2$. In this case, the charge density wave is gradually suppressed and disappears only in $Pd_{0.06}TaS_2$ [114]. CDW suppression was also observed upon doping with Fe in 1T–$Fe_xTa_{1-x}S_2$ single crystals ($0 \le x \le 0.05$) [136, 151]; superconductivity strongly depends on x in a narrow range, while the maximum T_c is 2.8 K at $x = 0.02$ [136]. This suggests that there superconductivity and CDW compete with each other, but complete suppression of the latter is not necessary for the former to reach maximal values.

Conductive properties

In terms of electrical conductivity, most interesting are conducting dichalcogenides of group 5 metals due to various CDW manifestations and semiconductor TMDs of groups 4, 6, and 7 owing to the possible usage of thin crystals and monolayers in semiconductor nanoelectronics.

HfQ_2, ZrQ_2. In accordance with the previously considered electronic structure, bulk ZrS_2, HfS_2, $ZrSe_2$, and $HfSe_2$ crystals are indirect band gap semiconductors with the band gap varying from ~1.2-1.5 eV for disulfides to ~0.6-1.0 eV for diselenides [175]. The band gap increases by a few tenths of electronvolts as the crystal thickness decreases down to monolayers, but dichalcogenides of Zr and Hf, in contrast to MoS_2, remain indirect band gap semiconductors [175]. Strong dependence of the band gap width on the choice of chalcogen and existence of a continuous series of solid solutions $ZrS_{2-x}Se_x$ and $HfS_{2-x}Se_x$ open the possibility of preparing a semiconductor material with optimal characteristics for each specific device [123]. Few-layer crystals and monolayers of $HfSe_2$ and $ZrSe_2$ were among the first 2D materials to demonstrated a whole complex of properties technologically important for semiconductor micro- and nano-electronics; earlier available only by silicon: optimal band gap values (~1-1.5 eV), high current ratio in open and closed field-effect transistor modes (10^6-10^8), and physico-chemical compatibility with technologically suitable dielectrics such as HfO_2 and ZrO_2 oxides [190].

In addition to the direct use of Zr and Hf disulfides and diselenides as semiconductor materials, various possibilities of chemical modification of their properties were also considered. Intercalation of HfQ_2, ZrQ_2 by alkali metals leads to the addition of electrons into MQ_2 layers, conduction band filling, and the transition to the metallic state [69]. At low temperatures, metallic intercalates demonstrate transition to the superconducting state [174]. A semiconductor–metal transition was observed in $ZrSe_2$ single crystals also upon the intercalation with Cu [248]. In the case of polycrystalline samples HfS_2, $HfSe_2$, intercalation with Cu, Fe, and Cr significantly decreased electrical resistance [96], but the conductivity preserved its hopping character, apparently, due to the localization of charge carriers on the potential of defects. Interestingly, the semiconductor–metal transition in single crystal $ZrSe_2$ was initiated by the intercalation (not substitution) with only 1.3 at.% Re introduced into the structure in the Re^{2+} state [249].

In contrast to disulfides and diselenides, $ZrTe_2$ and $HfTe_2$ are semimetals due to the valence/conduction bands overlap [174, 203, 250, 251]. $HfTe_2$ is a semimetal with a relatively high concentration of charge carriers ~10^{20}-10^{21}/cm^3 [203, 250] and the mobility of hole carriers increasing from ~30 cm^2/V·s at room temperature to ~1500 cm^2/V·s at $T = 2$ K. Hydrostatic pressure (up to ~5 GPa), that increases interlayer interactions, expectedly increases the overlap between the bands and the concentration of charge carriers, while the electrical resistance decreases several-fold. For single crystals $HfTe_2$, the obtained resistivity values along the layers $\rho_{//}(300\ K)$ were 0.17-2.7 mΩ·cm and decreased upon cooling by 36-120 times depending on growth conditions and, consequently, the crystal quality (amount of impurities and defects)

[250, 251]. Single crystals $ZrTe_2$ have very similar semi-metallic properties (electrical resistivity $\rho_{//}$(300 K) ~ 0.5 mΩ·cm) [251]. The authors of [252] reported the transition of $ZrTe_2$ to the superconducting state at T_c = 2 K.

Similarly to the use of intercalation and doping to transform semiconducting TMDs into the metallic state, similar approaches can be used to modify the properties of semimetallic $ZrTe_2$ and $HfTe_2$. For example, it was shown in [252] that intercalation of $ZrTe_2$ with Cr not only leads to the expected electron doping, increased number of electrons in the conduction band, and gradual disappearance of holes in the valence band, but also reduces the overlap between the bands. As a result, single crystals $Cr_{0.4}ZrTe_2$ transformed from semi-metals to metals with a partially filled conduction band separated from the valence band by an indirect band gap. Interestingly, despite the impurity potential of chromium, the superconducting transition temperature in $Cr_{0.4}ZrTe_2$ increased up to 5.4 K [252]. Intercalation with Ni increases the superconducting transition temperature up to T_c = 4.1 K in $Ni_{0.5}ZrTe_2$ [253]. The transition of $ZrTe_{2-x}Se_x$ to the semiconducting state associated with the appearance of an indirect band gap was induced by the isovalent substitution of the chalcogen atom [254].

NbQ_2, TaQ_2. At high temperatures, above the CDW formation point, dichalcogenides of Nb and Ta are quasi-2D metals with a half-filled conduction band whose resistivity values along the layers vary from several tens to several hundreds μΩ·cm [174, 227]. The CDW formation due to the Peierls instability (see above) leads to the formation of a band gap on a part of the Fermi surface and, consequently, abrupt decrease of the Pauli paramagnetic susceptibility due to the decreased density of states at the Fermi level, abrupt increase of electrical resistivity, changes in the Hall density of charge carriers and the thermal Seebeck coefficient. The magnitude of magnetic susceptibility jumps is determined by the percentage of the Fermi surface covered by the Peierls band gap. For electrical resistance, this dependence is more complicated since the reconfiguration of the Fermi surface affects not only the density of charge carriers but also the electron scattering parameters.

The Fermi surface of 2H and 4Hb polymorphs of NbS_2, $NbSe_2$, TaS_2, and $TaSe_2$ has a fairly complex topology. Their CDWs, which are formed at ~30-120 K mainly with the $3a \times 3a$ periodicity within a layer (see Refs. [174, 227] and references therein), lead to the formation of a band gap that covers only a small part of the Fermi surface. As a result, these compounds preserve metallic nature of electron transport and small electrical resistivity $\rho_{//}$ at low temperatures (from one tenth to several μΩ·cm). At low temperatures, all these metallic compounds (bulk crystals or individual monolayers obtained, in particular, by the intercalation of organic molecules) become superconducting; the maximum T_c = 7.2 K was observed in $NbSe_2$ (Ref. [174] and references therein).

Much more substantial electronic changes are caused by CDWs in ditellurides $NbTe_2$, $TaTe_2$ [255-257]. Besides CDWs with a period of $3a \times 3a$ formed in ditellurides above room temperature, a commensurate superstructure $\sqrt{19}a \times \sqrt{19}a$ was observed (see Ref. [255] and references therein). As a result of the CDW influence, the electrical resistivity of $NbTe_2$, $TaTe_2$ significantly exceeds that in disulfides and diselenides with the 2H structure: for example, $TaTe_2$ single crystals exhibit $\rho_{//}$(300 K) ≈ 200 μΩ·cm and $\rho_{//}$(3.5 K) ≈ 110 μΩ·cm [256].

The formation of CDW is most well manifested in the electrical resistance of polymorphs 1T–TaS_2 and 1T–$TaSe_2$ where the CDW-induced dielectric band gap covers the most part of the Fermi surface to cause an abrupt (by 1-2 orders of magnitude) increase of the electrical resistivity (Fig. 8*b*). In 1T–$TaSe_2$, the IC–CDW appears above 600 K and transforms directly into the C–CDW with the $\sqrt{13}a \times \sqrt{13}a$ period at 473 K. Upon the transition into the commensurate state, the amplitude of structural modulation (ion displacements) grows sharply, the band gap increases, and the curve of electrical resistivity shows a sharp jump [174, 227]. The remaining charge carriers provide metallic behavior down to low temperatures with electrical resistance $\rho_{//}$(5 K) ≈ 100 μΩ·cm. In 1T–TaS_2, the C–CDW state is achieved in several steps with two jumps of the electrical resistivity (at ~350 K and 200 K). The mechanisms of CDW formation and the methods of transition control were discussed in detail above.

Note that properties of 1T polymorphs cannot be explained only by considering the changes in the Fermi surface under the CDW action. Indeed, detailed ARPES (angle-resolved photoemission spectroscopy) studies of 1T–TaS_2 crystals [258] showed that, in agreement with calculations, the CDW with a $\sqrt{13}a \times \sqrt{13}a$ periodicity splits the 5*d* band of Ta into narrow subbands. The d^1 state and the 13-fold unit cell increase within the plane lead to the formation of six narrow filled subbands, six empty subbands, and one half-filled subband. The latter should have provided metallic conductivity; however, 1T–TaS_2 at low temperatures is dielectric. This behavior was explained (and experimentally confirmed) by strong correlations between electrons in the partially filled subband leading to the Mott transition [258]. In fact, in the C–CDW state in 1T–TaS_2, the cluster of 13 Ta ions (Fig. 8*a*) has only one electron located in its center. Coulomb electron correlations, forbidding two electrons to be in one cluster, "freeze" the order where the clusters form a periodic structure, with strictly one electron being localized in each cluster. Similar Mott dielectric states are well known in oxides with formally half-filled bands [259]. The violation of the Mott order, e.g. by the cationic substitution of Ta with Fe in 1T–$Fe_xTa_{1-x}S_2$, cancels the forbiddance of charge motion and leads to the formation of metallic and superconducting states [258]. Photoemission studies show that superconductivity coexists with CDW and arises in one of partially filled subbands out of 13 subbands formed by the CDW [258].

Conductive properties of NbQ_2 and TaQ_2 can be chemically modified using the same approaches as those for group 4 TMDs: intercalation with alkali, alkaline earth, and transition metals, organic molecules. For example, intercalation of silver and palladium into polymorphs 2H and 4Hb of TaS_2 can be used to modify their conductive properties and thee superconducting transition temperature [260]. In Pd-intercalated 2H–TaS_2, the superconducting state coexists and competes with the CDW; the maximal $T_c = 4.2$ K is reached in $Pd_{0.04}TaS_2$ [114].

The experimental data on the electron transport anisotropy associated with the layered crystal structure are very scarce because of the difficulty in preparing large single crystals without defects in their layer packing. However, it was noted that the anisotropy of group 5 TMD crystals is significantly lower than in their analogs of groups 4 and 6 due to the presence of an unpaired electron on the *d* shell. The anisotropy of electrical resistivity in stoichiometric crystals ranges from 10 to 100 and increases by orders of magnitude after the crystals are intercalated by metals or organic molecules [174, 227].

MoQ_2, WQ_2. Similarly to group 4 TMDs, bulk crystals MoS_2, WS_2, $MoSe_2$, and WSe_2 are indirect band gap semiconductors with a band gap of ~1.1-1.3 eV [185, 186, 216]; however, in contrast to the former, decreasing the crystal thickness to a monolayer not only increases the band gap up to ~1.9-2.0 eV but also transforms them into direct band gap semiconductors [185, 186, 261]. Consequently, the possible use of group 6 TMD monolayers, compared to those of group 4 TMDs, includes various devices related to electroluminescence and photovoltaics.

Like in the case of group 4 TMDs, the band gap of Mo and W disulfides and diselenides can be adjusted using its dependence on the choice of the metal and the chalcogen and by utilizing the possibility of preparing solid solutions. For example, it was shown that the band gap monotonously increases with x in the series $Mo_{1-x}W_xSe_2$ ($0 \le x \le 1$) [216]; additional increase can be achieved by substituting S with Se. At low temperatures, semiconducting compounds MoQ_2 and WQ_2 can be easily switched to metallic and superconducting states by intercalating them with metals or organic molecules (see above). The possibility of modifying electrical conductive properties by replacing Mo and W with group 5 and 7 elements is widely studied. For example, the study of Re-doped WSe_2 crystals showed that Re creates electronic levels in the forbidden band and switches *p*-type conductivity to *n*-type [262]. It was also demonstrated that electrical and optical anisotropy of single crystals of Mo and W dichalcogenides decreases by tens times with Re-doping [263, 264]. In turn, cationic substitution of Mo and W by Nb and Ta atoms, having one electron less on their outer shells, leads to the formation of acceptor impurities and increases the number of hole charge carriers [155, 265-267]. As the Nb concentration increases, the nature of electron transport changes to the metallic one.

The properties of $MoTe_2$ and WTe_2 qualitatively differ from those of disulfides and diselenides due to their ability to crystallize not only as the 2H polymorph but also as 1T′ and Td polymorphs [177-181, 268]. Similarly to disulfides and diselenides, 2H–$MoTe_2$ is a semiconductor with a band gap of ~0.9-1.0 eV and a charge carriers mobility of ~40 $cm^2/V{\cdot}s$ at 300 K [179-181]. However, bulk crystals structural 1T′ and Td modifications of $MoTe_2$ and Td–WTe_2 are semimetals. According to early research, the band overlap in semi-metallic phases is ~0.5 eV [177]; however, revised data showed that it is as small as ~0.05-0.06 eV [178-181]. Structurally, 1T′ –phase of $MoTe_2$ and WTe_2 can be considered as distorted 1T, and the nature of this distortion is related to the Peierls instability of the hypothetical 1T phase and to superstructural distortions leading to the formation of Mo–Mo or W–W chains. The resulting Fermi surface is composed of electronic and hole pockets along the axis corresponding to the direction of *M–M* chains. The concentration of charge carriers in $MoTe_2$ and WTe_2 is relatively low ($\sim10^{21}/cm^3$) with an electrical resistivity at room temperature of ~600-700 μΩ·cm in Td–WTe_2 [178] and ~400-1000 μΩ·cm in 1T′–$MoTe_2$ [179, 196, 268]. With decreasing temperature, the electrical resistivity decreases by hundreds of times: e.g., the mobility of charge carriers in 1T′–$MoTe_2$ increases from ~1 $cm^2/V{\cdot}s$ to 4000 $cm^2/V{\cdot}s$ [179]. Similarly to other TMDs, the degree of band overlap in 1T′ and Td phases depends on thickness: the overlap disappears in thin crystals (less than 10 layers) and the semi-metallic state switches to the semiconducting one.

It was shown that all three $MoTe_2$ polymorphs have very close energies. The reversible structural transition between structural modifications 2H and 1T′ occurs in the $MoTe_2$ crystal at 500-600 °C [179], yet under the action of a ~0.05% tensile deformation it takes place at 100°C, and under the action of a ~0.2% deformation it occurs at room temperature. As a result of such reversible transition, the electrical resistivity changes by four orders of magnitude [180].

In recent years, $MoTe_2$ and WTe_2 have attracted much attention due their to unusual electron transport properties. Compared to other non-magnetic materials, WTe_2 showed exceptional magnetoresistance values: its low-temperature electrical resistivity increases by $1.3\cdot10^5$ times in the 60 T magnetic field [178]; huge magnetoresistance was also observed in $MoTe_2$. The superconducting transition temperature T_c in semimetallic $MoTe_2$ crystals increases up to 8.2 K (by 80 times) under pressure [181].

Unusual properties of Td phases of $MoTe_2$ and WTe_2 are explained by the theoretically predicted “Weyl semimetal” state which added to the list of exotic and potentially practically useful electronic states such as: “topological insulators”, “topological superconductors”, “Dirac fermions” in graphene whose discussion goes beyond the scope of this review.

TcQ_2, ReQ_2. Group 7 TMDs are semiconductors with band gaps ~0.7-1.1 eV and ~1.0-1.4 eV for TcQ_2 and ReQ_2, respectively [182-184, 269]. Similarly to most other TMDs, the band gap decreases in the series S → Se → Te. Although first papers reported contradictory conclusions about the forbidden band structure, photoluminescence studies [183] showed that at least ReS_2 is a direct band gap semiconductor.

The properties of TcQ_2 and ReQ_2 are very close to other semiconducting TMDs, except for two significant features.

a. The semiconducting state in TcQ_2 and ReQ_2 is caused by *M–M* interactions that increase the unit cell size and lead to the formation of metal double-chains within the layer planes. As a result, electronic and optical properties of TcQ_2 and ReQ_2 exhibit significant in-plane anisotropy [182-184, 269].

b. In fact, the chains formed by metal ions close interionic interactions within the layer thus drastically weakening the interlayer bonds [183]. As a result, the electronic structure of TcQ_2 and ReQ_2, in contrast to other TMDs, is virtually independent of the crystal thickness, including the case of monolayers: weakly connected MQ_2 layers in these crystals *already* behave as virtually isolated monolayers. Therefore, the use of TcQ_2 and ReQ_2 does not require taking into account the dependence of their electronic properties on the crystal thickness and interlayer interactions.

Chemical modification of TcQ_2 and ReQ_2 is performed with standard approaches for TMDs. In particular, the studies of cationic substitutions in $Mo_xRe_{(1-x)}Se_2$ and $W_xRe_{(1-x)}Se_2$ showed that cationic substitutions not only increased the number of charge carriers and electrical conductivity but also reduced the in-plane anisotropy, apparently distorting the structure of Re–Re chains [270, 271].

Thermoelectric properties. Due to low thermal conductivity values κ, TMDs are attractive for thermoelectric applications. Among the TMDs considered in this review, thermoelectric properties were most well studied for molybdenum and tungsten dichalcogenides and their thermoelectric properties. Electrical conductivity of MoS_2 was increased to the required level by doping with Cu [272], Re, and Nb [197, 266]; however, no desired values of the thermoelectric figure of merit (*ZT*) have been achieved so far. Films prepared by mechanical exfoliation of MoS_2 crystal an subsequent deposition had a *ZT* value of $\approx 2\cdot10^{-4}$ at room temperature (the required value being $ZT > 1$ [273]), apparently, due to the defects at the boundaries of crystallites forming the film. The contacts between the crystallites were improved using annealing [274] and the method of introducing Cu into the defect areas [275] in order to increase the mobility of charge carriers and the Seebeck coefficient. Since one of the limitations for the use of flexible TMD films is weak charge transfer along *c* axis, the authors of [276] prepared a 3D structure of MoS_2 layers interpenetrated by carbon nanotubes (CNTs). Increasing the CNT content increased electrical conductivity by several orders of magnitude and decreased thermal conductivity. The maximal $ZT = 0.17$ at room temperature was obtained for the 20% CNT content.

The highest electrical conductivity increase in tungsten disulfide and diselenide was achieved using the acceptor substitution by group 5 elements (V, Nb, Ta) [267]. The authors of Refs. [155, 156, 265, 277] described the effect of substitutions in cationic and anionic sublattices and double substitutions in WQ_2. The maximal value $ZT = 0.26$ was obtained for sample $W_{0.98}Nb_{0.02}Se_{1.7}S_{0.3}$ at 650 K. In composite samples WS_2/MCNTs (multi-walled CNTs) $ZT = 0.22$ at $T = 800$ K was obtained for the CNT content ~0.75 wt.% [278].

Magnetism

Stoichiometric TMDs are weakly magnetic materials, since neither metal ions nor chalcogen ions have localized magnetic moments. In semiconducting TMD of groups 4 and 6 elements, the transition metal ions occur either in the d^0 state with no *d* electrons at all or in the d^2 state with a pair of electrons on the d_{z^2} orbital (see above), all other orbitals being empty. In semiconducting group 7 TMDs with metal ions in the d^3 state, the unit cell quadrupling leads to the formation of six completely filled subbands, which also excludes the magnetism of *d* shell electrons. In turn, in the case of metallic TMDs, mobile electrons in the conduction band can demonstrate only weak Pauli paramagnetism whose magnitude provides data on the density of states at the Fermi level. This is widely used to characterize phase transitions associated with the CDW formation when the density of states is decreased due to the emerging band gap (Fig. 10) [227].

The possibility to intercalate various magnetic ions with unfilled *d* or *f* shells into the interlayer space of TMDs was widely used to “design” various magnetic materials M'_xMQ_2 consisting of alternating magnetic layers M'_x and non-magnetic MQ_2 layers (see refs. [96, 174, 279-281] and references therein). The over-exchange interaction of M' ions via M'–Q bonds and indirect RKKY (Ruderman–Kittel–Kasuya–Yosida) interaction via conduction electrons of the MQ_2 layer lead to the formation of antiferromagnetic states in ordered intercalates $M'_{1/3}MQ_2$ and $M'_{1/4}MQ_2$ as well as various cluster spin glasses in the case of intermediate compositions and multicomponent doping. Magnetic intercalates attracted much interest due to the

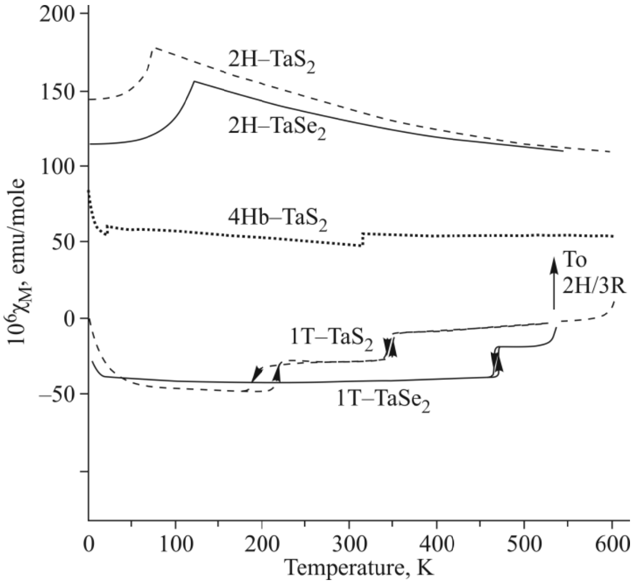

Fig. 10. Impact of CDW transitions on magnetic susceptibilities of various TaS_2 polymorphs. The figure is cited from [227], ©Advances in Physics, Taylor & Francis, 1975.

possibility of studying the physics of quasi-2D magnets and the interaction between the magnetic order and the electronic subsystem of MQ_2 layers.

High interest in the research and application of thin TMD crystals and monolayers has raised a problem of obtaining magnetic states directly in the electronic subsystem of MQ_2 layers. In particular, the preparation of semiconducting and metal monolayers with spin-polarized charge carriers is of exceptional interest for spintronics. One possible approach is cationic substitutions. For example, the ferromagnetic state of ZrS_2 single crystals is obtained by doping with iron [282]. Detailed theoretical calculations prove the possibility of obtaining FM semiconducting and FM semimetallic states upon cationic substitution with various 3*d* metals [218-220, 283, 284]. An interesting method for obtaining ferromagnetic states was proposed in [178] where it was shown that a certain tensile strain applied to the monolayers of Zr and Hf dichalcogenides, the hole carriers doped into the monolayer should exhibit spontaneous ferromagnetic polarization.

Raman spectroscopy

Raman spectroscopy has been very useful in the study of layered TMDs. Upon the transition from bulk samples to few-layer ones and upon the decrease in the number of layers, the samples demonstrate, among other things, symmetry changes while forbidden vibrations become allowed, possibly causing shifts in the positions of modes and the appearance of new modes. The Raman spectra of Mo and W dichalcogenides are most sensitive to the number of layers. The main vibrational modes of MoS_2 are A_{1g} 408 cm^{-1} and E^1_{2g} 383 cm^{-1}. The decrease in the number of layers leads to the blue shift of A_{1g} to 403 cm^{-1} and the red shift of E^1_{2g} to ~385 cm^{-1} and to the band broadening [285]. $MoSe_2$ shows a similar band shifts as the number of layers decreases. However, A_{1g} splits into two bands at a thickness of 3-4 layers and into three bands at a thickness of five layers. The spectral positions of two peaks for three $MoSe_2$ layers are located almost symmetrically with respect to the monolayer line. The observed splittings range from 2.4 cm^{-1} to 3.2 cm^{-1}. This effect is caused by the so-called Davydov splitting due to the presence of more than one molecule in the $MoSe_2$ unit cell. At a thickness of two layers, mode B^1_{2g} appears at 353 cm^{-1}, which was not active in the bulk sample [286]. Another interesting effect was observed in the case of applying dichalcogenide layers on a substrate. For example, mode E_{1g}, which is usually forbidden in the Raman configuration, was observed in supported $TaSe_2$ layers and disappears in suspended layers, thus suggesting that this mode may be activated due to symmetry breaking caused by the interaction with the substrate. A systematic low-temperature Raman study revealed some phonon features related to the NC–CDW formation in monolayer layer and double layer 2H–$TaSe_2$, namely, softening of a wide second-order Raman mode near the phase transition point as a result of strong electron-phonon coupling (Kohn anomaly) [287]. The Raman spectra of dichalcogenides $ZrSe_2$ [288], HfS_2 [289, 290], $HfSe_2$ [290, 291], ReS_2 [183, 292], $ReSe_2$ [293] show no significant changes upon the transition from bulk to nanostructured few-layer samples. Note however that rhenium dichalcogenides exhibit significant in-plane anisotropy of optical properties caused by the chains of Re ions in their structure [293]. For dichalcogenides $ZrTe_2$ [294], $HfTe_2$ [295], $TaTe_2$ [295], and TcS_2 [296], some spectroscopic data were reported without considering the effect of sample thickness. Table 3 summarizes the data on TMDs whose Raman spectra depend on the sample thickness along with the general changes exhibited by the spectra upon the transition from bulk to few-layer samples.

Chemical modification (doping, intercalation) causes more significant changes in Raman spectra. As a result of isovalent substitution in the anion sublattice of sulfur atoms with selenium, the frequency of Raman modes $A_{1g}(M\text{–}Q)$ decreases as the content of the heavier Se atom increases, i.e. there is an evident red shift of A_{1g} in M–Se and blue shift in M–S accompanied by corresponding intensities changes in TMDs: $ZrS_{2-x}Se_x$ [123], $HfS_{2-x}Se_x$ [308], 1T–$TaS_{2-x}Se_x$ [309], $MoS_{2-x}Se_x$ [310], $WS_{2-x}Se_x$ [311]. A similar behavior is exhibited also by Te-substited chalcogenides, provided that the 2H modification, e.g. $MoTe_xSe_{2-x}$, is preserved [312]. At increasing x, the A_{1g} mode is red shifted from 240 cm^{-1} to 230 cm^{-1} and is asymmetrically broadened towards low frequencies; the E^1_{2g} frequency is not changed and only shows the band broadening. The changes of phonon energy in mixed rhenium dichalcogenide $ReS_{2-x}Se_x$ were studied by optical methods [313].

TABLE 3. General Changes in the Raman Spectra with Decreasing Number of TMD Layers

Composition	Main modes in the bulk sample, cm^{-1}	Changes with decreasing number of layers	Additional data	Ref.
ZrS_2	A_{1g} 334	Intensity decreases	-	[288]
NbS_2	A_1 384	Red shift, 1L 376 cm^{-1}	-	[31]
$NbSe_2$	28	Red shift, to 1L 20 cm^{-1}	The number and position of bands is very sensitive to the irradiation wavelength	[297, 298]
	A_{1g} 230	Red shift		
	E_{2g} 240	Blue shift, to 1L 250 cm^{-1}		
$NbTe_2$	A_g^3 263	Intensity decreases	-	[257, 299]
	A_g^7 217			
TaS_2	A_{1g} 400 E_{2g}^1 280	Increased intensity and sharpness of the peaks	-	[206]
$TaSe_2$	A_g^1 235	Blue shift, 1L 233 cm^{-1}	-	[199, 287]
MoS_2	E_{2g}^1, 383	Blue shift, intensity decreases, broadening	-	[285]
	A_{1g}, 408	Red shift, broadening		
$MoSe_2$	E_{2g}^1, 285	Blue shift, broadening, 3-4L splits into two modes, 5L splits into three modes	2L appearance of B_{2g}^1 353	[286]
	A_{1g}, 242	Red shift, intensity increases		
$MoTe_2$	A_g^1 77, A_g^2 86, B_g^1 91, A_{1g} 170, E_{2g}^1 234	Increases intensity bands at 260 cm^{-1} and 100-120 cm^{-1}	B_{2g}^1 283 is absent in bulk and 1L, maximal in 2L, and decreases with increasing L	[300, 301]
WS_2	A_{1g} 420	Red shift to 1L 417 cm^{-1}, broadening	LA(M) Band appears at 176 cm^{-1}	[302, 303]
	E_{2g}^1 354	Intensity increases		
WSe_2	E_{2g}^1 249		E_{1g} 176 and B_{2g}^1 310 appear, blue shift upon thickness decrease	[304-306]
WTe_2	A_1^2 ($A_g^1 + A_g^2$) 208	Red shift, broadening	Blue shift of A_g^3, B_g^2	[307]

Notes: L is the number of layers, 1L is a single-layer sample, *n*L is a sample with *n* layers (*n* = 1, 2, 3, etc.)

The effect of isovalent substitution in the cationic sublattice was studied on the example of $Mo_{1-x}W_xQ_2$ in bulk [314] and few-layer samples [134, 315]; all the samples showed the same tendency. The A_{1g} modes exhibit a single-mode behavior and E_{2g}^1 exhibit a double-mode behavior for the entire series caused not only by sulfur vibrations but also by the metal atom vibrations. The double-mode behavior is caused by the difference between the weights of vibrating cations Mo and W. At increasing *x*, A_{1g} is red shifted and its intensity increases, whereas E_{2g}^1 is blue shifted and splits into two modes. The Raman spectrum of $Nb_{0.5}Ta_{0.5}Q_2$ (Q = S or Se) is a superposition of spectra of corresponding NbQ_2 and TaQ_2 [316].

The Raman shift upon non-isovalent substitution with atoms from other groups can be explained by the reduction of bond lengths and by the changes in electron-phonon interactions. For example, doping ZrS_2 with iron makes modes E_g (246.78 cm^{-1}) and A_{1g} (332.23 cm^{-1}) shift to 257.5 cm^{-1} and 343.43 cm^{-1}, respectively, and the Raman shift is a result of reduced metal–chalcogen bond lengths [282]. Non-isovalent doping of the *p*/*n* type leads to the blue/red shift of A_{1g} due to the changes in electron-phonon interactions, while the frequency of E_{2g} should undergo almost no changes [317]. This was shown on the example of $Nb_xMo_{1-x}S_2$ in [318, 319]. Two optical phonon modes corresponding to A_{1g} and E_{2g} were observed for a $Nb_xW_{1-x}S_2$ monolayer at 413 cm^{-1} and 353 cm^{-1} with a small blue shift compared to pure WS_2. Doping WS_2 with Nb leads to the formation of a large number of hole charge carriers that interact with incoming photons, thus possibly causing blue shifts of Raman peaks, similarly to the changes observed in ReS_2 doped with Mo [320].

There are examples of some other Raman spectra of non-isovalently substituted TMDs: MoS_2 doped with Nb [318, 319], Re [321, 322], Sb [323], Pd [324], Ni [325]; $Re_xMo_{1-x}Se_2$ [326], WS_2, doped with Nb [327], V [328], Au [329]; WSe_2 doped with Co [330]; WQ_2 (Q = S, Se, Te) doped with Nb (our works, JSC 2017 and 2020).

Raman spectroscopy of intercalated compounds can reveal phonon energy shifts of active phonon modes A_{1g} and E_g, disappearance of double-phonon modes, and appearance of new modes with low wavenumbers caused by the fact that the presence of an intercalant superlattice reorganizes the Brillouin zone [331]. A shift of phonon modes A_{1g} and E_g was observed upon the intercalation of TMDs both by alkali metal atoms and by transition metals: M_xZrSe_2 (M = Li, K, Cs) [202], Li_xHfQ_2 [203], Fe_xNbS_2 [332], Fe_xNbSe_2 [333], Fe_xTaSe_2 [334], Mn_xMoSe_2 [334].

APPLICATIONS: CATALYSIS, SENSORS, DETECTORS

Due to unique properties, in particular, the possibility of preparing stable crystals of monomolecular thickness, TMDs are promising materials for electronics, spintronics, optoelectronics and as sensor materials. Thin-layer dichalcogenides of Zr and Hf are studying in as semiconductor materials for electronics [190, 335], solar panels (ZrS_2 [109]), photodetectors, matrices for Li^+- and Na^+- ion batteries, photocatalysts [336], and thermoelectric materials [32]. NbQ_2 (Q = S, Se) and its modifications are used for energy storage (Li-ion batteries) [337], as conductive electrodes for nanoelectronic devices, including field effect transistors [338]. $NbSe_2$ can be used as a material for superconducting photodetectors [339] and monopole RF antennas [340]. 2H–TaS_2 is studied in HER electrocatalysis [341, 342]. 1T–TaS_2 was proposed as a material that can be switched between metastable (conductive and dielectric) CDW states by applying electric field or optical excitation [229, 343]. MQ_2 (M = Mo, W; Q = S, Se) are used in energy storage devices (Li^+, Na-ion batteries), sensors (NO, glucose, DNA, small molecules), photoelectronic and piezoelectric devices, biosensors, transistors [186, 188, 189, 344-346].

Morphology changes and chemical modification provide fine tuning of practically important TMD properties to be used more effectively. For example, the ratio of currents in open and closed states of field-effect transistors made of Nb-doped MoS_2 significantly varies depending on the flake thickness, and even ultra-thin heavily doped 2D semiconductors cannot be completely depleted and behave like a 3D material when used in the FET geometry [347].

Electrocatalysis, photocatalysis, hydrogen evolution reactions

Over the past decade, TMDs have attracted increasing attention as electrode materials for electrocatalytic decomposition of water. It was shown on the example of MoS_2 that, even though the basal plane of MoS_2 is catalytically inert, its sulfided Mo edges are active in hydrogen evolution reactions (HERs) with a suitable energy $\Delta G_H = 0.1$ V, which is close to that of several efficient HER electrocatalysts, including Pt, nitrogenase, and hydrogenase [348]. Electrocatalytic properties of TMD materials are improved by two main approaches: increasing the number of active centers with the help of structural engineering ("extrinsic" approach) and modifying chemical composition to reduce ΔG_H ("intrinsic" approach) [349].

The "extrinsic" approach of TMD modification includes morphology change, i.e. size and shape of catalyst particles and the addition of electrically conductive substrates such as graphene. The effect of morphology on the catalytic activity in HERs was studied by experimental and calculation methods on the example of MoS_2: dependence of catalytic activity on the number of layers [2, 350], hollow MoS_2 nanoparticles doped with oxygen [351], MoS_2 flakes on carbon [352] and graphene nanosheets [353, 354], monolayers doped with transition metals [35], etc.

The “intrinsic” approach to increase catalytic activity is aimed at changing the ΔG_H value either by isovalent substitution in cationic and anionic sublattices or by non-isovalent substitution (doping) in the cationic sublattice, which also affects electrical conductivity.

Catalytic activity of isovalently substituted TMDs is fairly well studied for Mo and W: $MoS_{2-x}Se_x$ [356], $MoSe_{2-x}Te_x$ [357], $WS_{2-x}Se_x$ [358], $Mo_xW_{1-x}(S_ySe_{1-y})_2$ [359]. There are examples of other TMDs. Thus, the calculated band gap of ZrS_2 and Janus ZrSSe monolayers is 1.58 eV and 1.08 eV, respectively; therefore, they can be used in as photocatalysts, whereas $ZrSe_2$ has a small band gap of 0.84 eV and hence can be possibly used as an electrocatalyst. Calculations of the hydrogen adsorption energy and the Gibbs free energy showed that Janus ZrSSe exhibits better catalytic activity than ZrS_2 and $ZrSe_2$ [360]. The catalytic activity of $ReS_xSe_{(2-x)}$ composites with substituted anionic sublattices on carbon fiber paper (CFP) were studied in HER reactions. Doping $ReSe_2$ with sulfur atoms increases the number of active sites and enhances electrical conductivity; electrocatalyst $ReSe_{1.78}S_{0.22}$/CFP provides better HER characteristics than $ReSe_2$ with a low overvoltage of 123 mV to achieve a current density of 10 mA/cm^2 as well as long-term stability for 30 h [361].

The catalytic activity of doped TMDs in HER reactions was shown both by calculation and experimental methods. For example, introducing Na^+, Ca^{2+}, Ni^{2+}, Co^{2+} cations between the layers of 1T–MoS_2 is an effective strategy to reduce overvoltage in hydrogen evolution reactions. Thus, the initial potential of 1T–MoS_2 with intercalated ions decreases by ~60 mV in acidic environment compared with the initial 1T–MoS_2 potential (beginning at ~180 mV) [362]. A presence of Fe, Co, Ni, Pd, and Pt dopants in the TcS_2 monolayer affects the profiles of electron density of states which may be important for HER. It was found out that ΔG_H in the case of vacancy complexes Ni, Pd, and Pt is very close to the thermoneutral point $\Delta G_H = 0$ eV. This indicates that the activity of TcS_2 in HERs can be significantly improved by Ni, Pd, and Pt doping [363]. Doping ZrQ_2 with Nb, Pt, and W atoms adjusts the electronic properties of these systems by switching their nature to the metallic one; as a result, its catalytic activity is improved compared to the semiconductor catalyst. Calculations of the Gibbs free energy showed that Nb–$ZrSe_2$ is the best material for HER, the next ones are Pt–ZrS_2, Nb–ZrSSe, Nb–ZrS_2, and ZrSSe, and the introduction of W atoms does not lead to significant improvements [360]. A ReS_2 sample doped with 2% of Co atoms was found highly effective both in acidic (149 mV) and in alkaline electrolytes (240 mV): its current density reached 10 mA/cm^2, and it demonstrated excellent long-term durability in hydrogen evolution reactions [364].

Sorption, gas sensors, and detectors

In the field of gas sensors, current studies focus on the development of miniaturized high-performance gas sensors operating at room temperature. Layered semiconductor TMDs have attracted particular attention, in particular, due to the possibility to prepare flexible and compact sensors [365, 366]. Characteristics of MoS_2 based gas sensors (Fig. 11) with proposed mechanisms are discussed in the context of a wide range of different morphologies/nanostructures, nanocomposites, van der Waals heterostructures, and photoactivation effects [367].

The ability of doped TMDs, in particular MoS_2, to adsorb various molecules was studied by Calculation methods (Table 4).

It was established that the defectiveness of TMD structures with respect to chalcogen may improve the sensor response. Thus, DFT calculations showed that defected monolayers of ZrS_2 with S vacancies demonstrate better gas adsorption (NO, NO_2, CO, SO_2, N_2, H_2, O_2, CO_2) than pure ZrS_2 structures. Among these gases, CO_2, CO, and N_2 molecules are physically adsorbed on the S vacancies of defected ZrS_2 monolayers, while O_2, NO, SO_2 molecules are chemically adsorbed in the areas that are closed for S vacancies of ZrS_2 monolayers. Also, an NO_2 molecule can be separated by an S vacancies of the defected ZrS_2 monolayer. The results of this work suggest that defected ZrS_2 monolayers with S vacancies can be used as adsorbents in gas sensors to determine the content of CO_2, CO and are particularly sensitive to N_2 [380].

It was shown on the example of tungsten dichalcogenides that doping and functionalization also improve the sensor response. Adsorption of gas molecules CO_2, NO_2, and SO_2 on a WSe_2 monolayer doped with Pd, Ag, Au, Pt was studied in terms of adsorption energy, charge transfer, and band structures. It was shown that NO_2 adsorption on a Ag–WSe_2 monolayer

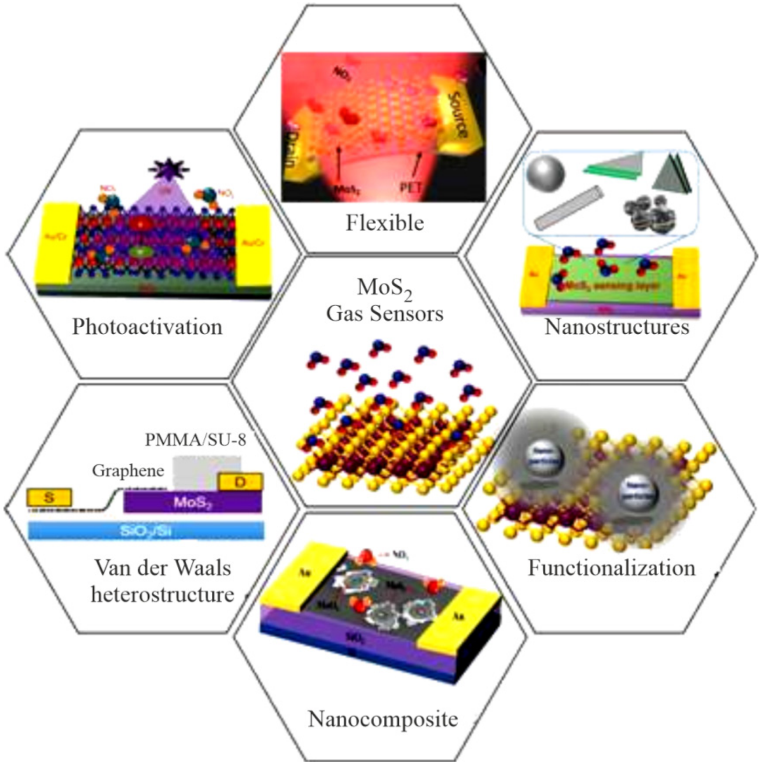

Fig. 11. Schematic illustration of strategies for the fabrication of the MoS_2 based gas sensor. The figure is cited from [367], ©Advanced Materials Technologies, John Wiley & Sons, Ltd, 2020.

TABLE 4. Ability of Doped MoS_2 Samples to Adsorb Various Molecules

Doping	Sorption	Ref.
-	H_2, O_2, H_2O, NH_3, NO, NO_2, CO_2, CO	[368, 369]
Al	H_2O	[370]
O	Thiophene	[371]
Ni, Si, P	H_2	[372]
V, Nb, Ta	CO, NO_2, H_2O, NH_3	[373]
Co, Ni, Cu	O_2	[374]
Al, Si, P	NO_2, NH_3	[375]
Cl, P, Si	H_2CO (formaldehyde)	[376]
B, P, Cl	NO	[377]
	From Sc to Zn	[378]
WS_2	CO, H_2O, NH_3, NO, NO_2	[379]

is energetically favorable and that chemisorption is achieved [381]. Functionalization of the 2D surface of WS_2 nanoflakes proved a possibility of fabricating flexible CO gas sensors with a low power consumption [382].

The possibility of combining TMDs possessing unique sorbent and electrophysical properties with other functional materials opens up opportunities of designing FET-based gas sensors. To prepare a thin film transistor gas sensor based on the *p*-*n* heterojunction, a WS_2 monolayer grown by the CVD process was transferred onto an indium–gallium–zinc-oxide (IGZO) film [383]. The authors of [383] reported that the resulting device had the best NO_2 gas sensor response compared to all the gas sensors based on transition metal dichalcogenide materials.

FUNDING

The reported study was funded by RFBR, project number 20-13-50231.

CONFLICT OF INTERESTS

The authors declare that they have no conflict of interests.

REFERENCES

1. Q. Ding, B. Song, P. Xu, and S. Jin. *Chem*, **2016**, *1*(5), 699. https://doi.org/10.1016/j.chempr.2016.10.007
2. Y. Yu, S.-Y. Huang, Y. Li, S.N. Steinmann, W. Yang, and L. Cao. *Nano Lett*., **2014**, *14*(2), 553. https://doi.org/10.1021/nl403620g
3. X. Chia, A. Ambrosi, P. Lazar, Z. Sofer, and M. Pumera. *J. Mater. Chem. A*, **2016**, *4*(37), 14241. https://doi.org/10.1039/C6TA05110C
4. Y. Kim, K. C. Kwon, S. Kang, C. Kim, T. H. Kim, S.-P. Hong, S. Y. Park, J. M. Suh, M.-J. Choi, S. Han, and H. W. Jang. *ACS Sensors*, **2019**, *4*(9), 2395. https://doi.org/10.1021/acssensors.9b00992
5. E. Zhang, Y. B. Jin, X. Yuan, W. Y. Wang, C. Zhang, L. Tang, S. S. Liu, P. Zhou, W. D. Hu, and F. X. Xiu. *Adv. Funct. Mater*., **2015**, *25*(26), 4076. https://doi.org/10.1002/adfm.201500969
6. J. Xiao, D. Choi, L. Cosimbescu, P. Koech, J. Liu, and J. P. Lemmon. *Chem. Mater*., **2010**, *22*(16), 4522. https://doi.org/10.1021/cm101254j
7. T. Stephenson, Z. Li, B. Olsen, and D. Mitlin. *Energy Environ. Sci*., **2014**, *7*(1), 209. https://doi.org/10.1039/C3EE42591F
8. A. A. Tedstone, D. J. Lewis, and P. O′Brien. *Chem. Mater*., **2016**, *28*(7), 1965. https://doi.org/10.1021/acs.chemmater.6b00430
9. J. T. Li, M. M. Naiini, S. Vaziri, M. C. Lemme, and M. Ostling. *Adv. Funct. Mater*., **2014**, *24*(41), 6524. https://doi.org/10.1002/adfm.201400984
10. M. S. Whittingham. *Prog. Solid. State Chem*., **1978**, *12*(1), 41. https://doi.org/10.1016/0079-6786(78)90003-1
11. T. Sörgel and M. Jansen. *Solid State Sci*., **2004**, *6*(11), 1259. https://doi.org/10.1016/j.solidstatesciences.2004.07.017
12. F. R. Gamble, J. H. Osiecki, M. Cais, R. Pisharody, F. J. DiSalvo, and T. H. Geballe. *Science*, **1971**, *174*(4008), 493. https://doi.org/10.1126/science.174.4008.493
13. H. S. S. Ramakrishna Matte, A. Gomathi, A. K. Manna, D. J. Late, R. Datta, S. K. Pati, and C. N. R. Rao. *Angew. Chem., Int. Ed*., **2010**, *49*(24), 4059. https://doi.org/10.1002/anie.201000009
14. J. N. Coleman, M. Lotya, A. O′Neill, S. D. Bergin, P. J. King, U. Khan, K. Young, A. Gaucher, S. De, R. J. Smith, I. V. Shvets, S. K. Arora, G. Stanton, H.-Y. Kim, K. Lee, G. T. Kim, G. S. Duesberg, T. Hallam, J. J. Boland, J. J. Wang, J. F. Donegan, J. C. Grunlan, G. Moriarty, A. Shmeliov, R. J. Nicholls, J. M. Perkins, E. M. Grieveson, K. Theuwissen, D. W. McComb, P. D. Nellist, and V. Nicolosi. *Science*, **2011**, *331*(6017), 568. https://doi.org/10.1126/science.1194975
15. G. Cunningham, M. Lotya, C. S. Cucinotta, S. Sanvito, S. D. Bergin, R. Menzel, M. S. P. Shaffer, and J. N. Coleman. *ACS Nano*, **2012**, *6*(4), 3468. https://doi.org/10.1021/nn300503e
16. S. B. Artemkina, T. Y. Podlipskaya, A. I. Bulavchenko, A. I. Komonov, Y. V. Mironov, and V. E. Fedorov. *Colloids Surf. A*, **2014**, *461*, 30. https://doi.org/10.1016/j.colsurfa.2014.07.021
17. J.-Y. Kim, S. M. Choi, W.-S. Seo, and W.-S. Cho. *Bull. Kor. Chem. Soc*., **2010**, *31*(11), 3225. https://doi.org/10.5012/bkcs.2010.31.11.3225
18. N. Onofrio, D. Guzman, and A. Strachan. *J. Appl. Phys*., **2017**, *122*(18), 185102. https://doi.org/10.1063/1.4994997

19. Z. Sofer, D. Sedmidubský, J. Luxa, D. Bouša, Š. Huber, P. Lazar, M. Veselý, and M. Pumera. *Chem. Eur. J.*, **2017**, *23*(42), 10177. https://doi.org/10.1002/chem.201701628
20. A. Niazi and A. K. Rastogi. *J. Condens. Matter Phys.*, **2001**, *13*(31), 6787. https://doi.org/10.1088/0953-8984/13/31/315
21. M. Inoue, M. Koyano, H. Negishi, Y. Ueda, and H. Sato. *Phys. Status Solidi B*, **1985**, *132*(1), 295. https://doi.org/10.1002/pssb.2221320130
22. M. Inoue, H. Negishi, T. Fujii, K. Takase, Y. Hara, and M. Sasaki. *J. Phys. Chem. Solids*, **1996**, *57*(6), 1109. https://doi.org/10.1016/0022-3697(95)00405-X
23. F. L. Deepak, R. Popovitz-Biro, Y. Feldman, H. Cohen, A. Enyashin, G. Seifert, and R. Tenne. *Chem. Asian J.*, **2008**, *3*(8/9), 1568. https://doi.org/10.1002/asia.200800083
24. Y. Huan, J. Shi, X. Zou, Y. Gong, C. Xie, Z. Yang, Z. Zhang, Y. Gao, Y. Shi, M. Li, P. Yang, S. Jiang, M. Hong, L. Gu, Q. Zhang, X. Yan, and Y. Zhang. *J. Am. Chem. Soc.*, **2019**, *141*(47), 18694. https://doi.org/10.1021/jacs.9b06044
25. G. Leicht, H. Berger, and F. Levy. *Solid State Commun.*, **1987**, *61*(9), 531. https://doi.org/10.1016/0038-1098(87)90162-1
26. A. Ubaldini, J. Jacimovic, N. Ubrig, and E. Giannini. *Cryst. Growth Des.*, **2013**, *13*(10), 4453. https://doi.org/10.1021/cg400953e
27. M. Rahman, K. Davey, and S.-Z. Qiao. *Adv. Funct. Mater.*, **2017**, *27*(10), 1606129. https://doi.org/10.1002/adfm.201606129
28. D. A. Chareev, P. Evstigneeva, D. Phuyal, G. J. Man, H. Rensmo, A. N. Vasiliev, and M. Abdel-Hafiez. *Cryst. Growth Des.*, **2020**, *20*(10), 6930. https://doi.org/10.1021/acs.cgd.0c00980
29. M. Zhang, Y. Zhu, X. Wang, Q. Feng, S. Qiao, W. Wen, Y. Chen, M. Cui, J. Zhang, C. Cai, and L. Xie. *J. Am. Chem. Soc.*, **2015**, *137*(22), 7051. http://doi.org/10.1021/jacs.5b03807
30. C. Yan, L. Gan, X. Zhou, J. Guo, W. Huang, J. Huang, B. Jin, J. Xiong, T. Zhai, and Y. Li. *Adv. Funct. Mater.*, **2017**, *27*(39), 1702918. https://doi.org/10.1002/adfm.201702918
31. Q. Lv, X. Qin, and R. Lv. *Front. Mater.*, **2019**, *6*, 279, https://doi.org/10.3389/fmats.2019.00279
32. C. Yan, C. Gong, P. Wangyang, J. Chu, K. Hu, C. Li, X. Wang, X. Du, T. Zhai, Y. Li, and J. Xiong. *Adv. Funct. Mater.*, **2018**, *28*(39), 1803305. https://doi.org/10.1002/adfm.201803305
33. X. Wang, H. Feng, Y. Wu, and L. Jiao. *J. Am. Chem. Soc.*, **2013**, *135*(14), 5304. https://doi.org/10.1021/ja4013485
34. C. Lan, C. Li, Y. Yin, and Y. Liu. *Nanoscale*, **2015**, *7*(14), 5974. https://doi.org/10.1039/C5NR01205H
35. N. Briggs, S. Subramanian, Y. C. Lin, S. Eichfeld, B. Jariwala, G. Bhimanapati, and K. Zhang, J.A. Robinson. *ECS Trans.*, **2016**, *75*(8), 725. https://doi.org/10.1149/07508.0725ecst
36. Y. Yu, C. Li, Y. Liu, L. Su, Y. Zhang, and L. Cao. *Sci. Rep.*, **2013**, *3*(1), 1866. https://doi.org/10.1038/srep01866
37. M. Krbal, J. Prikryl, R. Zazpe, F. Dvorak, F. Bures, and J. M. Macak. *Phys. Status Solidi RRL*, **2018**, *12*(5), 1800023. https://doi.org/10.1002/pssr.201800023
38. B. Groven, M. Heyne, A. Nalin Mehta, H. Bender, T. Nuytten, J. Meersschaut, T. Conard, P. Verdonck, S. Van Elshocht, W. Vandervorst, S. De Gendt, M. Heyns, I. Radu, M. Caymax, and A. Delabie. *Chem. Mater.*, **2017**, *29*(7), 2927. https://doi.org/10.1021/acs.chemmater.6b05214
39. N. Arya, P. Avasthi, and V. Balakrishnan. *Nanoscale Adv.*, **2021**, *3*(7), 2089. https://doi.org/10.1039/D0NA00901F
40. Z. Safaei Mahmoudabadi, A. Rashidi, and M. Panahi. *Int. J. Hydrog. Energy*, **2021**, *46*(7), 5270. https://doi.org/10.1016/j.ijhydene.2020.11.077
41. F. Cui, C. Wang, X. Li, G. Wang, K. Liu, Z. Yang, Q. Feng, X. Liang, Z. Zhang, S. Liu, Z. Lei, Z. Liu, H. Xu, and J. Zhang. *Adv. Mater.*, **2016**, *28*(25), 5019. https://doi.org/10.1002/adma.201600722
42. J. Su, K. Liu, F. Wang, B. Jin, Y. Guo, G. Liu, H. Li, and T. Zhai. *Adv. Mater. Interfaces*, **2019**, *6*(19), 1900741. https://doi.org/10.1002/admi.201900741

43. C. J. Carmalt, E. S. Peters, I. P. Parkin, T. D. Manning, and A. L. Hector. *Eur. J. Inorg. Chem.*, **2004**, *2004*(22), 4470. https://doi.org/10.1002/ejic.200400308
44. E. S. Peters, C. J. Carmalt, I. P. Parkin, and D. A. Tocher. *Eur. J. Inorg. Chem.*, **2005**, *2005*(20), 4179. https://doi.org/10.1002/ejic.200500400
45. N. D. Boscher, C. J. Carmalt, and I. P. Parkin. *Eur. J. Inorg. Chem.*, **2006**, *2006*(6), 1255. https://doi.org/10.1002/ejic.200500857
46. T. Shimada, H. Nishikawa, A. Koma, Y. Furukawa, E. Arakawa, K. Takeshita, and T.. Matsushita. *Surface Sci.*, **1996**, *369*(1), 379. https://doi.org/10.1016/S0039-6028(96)00915-6
47. F. Cheng, Z. Ding, H. Xu, S. J. R. Tan, I. Abdelwahab, J. Su, P. Zhou, J. Martin, and K. P. Loh. *Adv. Mater. Interfaces*, **2018**, *5*(15), 1800429. https://doi.org/10.1002/admi.201800429
48. O. Ávalos-Ovando, D. Mastrogiuseppe, and S. E. Ulloa. *J. Condens. Matter Phys.*, **2019**, *31*(21), 213001. https://doi.org/10.1088/1361-648X/ab0970
49. C. Schuffenhauer, R. Popovitz-Biro, and R. Tenne. *J. Mater. Chem.*, **2002**, *12*(5), 1587. https://doi.org/10.1039/B110240K
50. C. Schuffenhauer, B. A. Parkinson, N. Y. Jin-Phillipp, L. Joly-Pottuz, J.-M. Martin, R. Popovitz-Biro, and R. Tenne. *Small*, **2005**, *1*(11), 1100. https://doi.org/10.1002/smll.200500133
51. L. Margulis, G. Salitra, R. Tenne, and M. Talianker. *Nature*, **1993**, *365*(6442), 113. https://doi.org/10.1038/365113b0
52. R. Tenne, L. Margulis, M. Genut, and G. Hodes. *Nature*, **1992**, *360*(6403), 444. https://doi.org/10.1038/360444a0
53. K. S. Coleman, J. Sloan, N. A. Hanson, G. Brown, G. P. Clancy, M. Terrones, H. Terrones, and M. L. H. Green. *J. Am. Chem. Soc.*, **2002**, *124*(39), 11580. https://doi.org/10.1021/ja0261630
54. E. Bi, H. Chen, X. Yang, F. Ye, M. Yin, and L. Han. *Sci. Rep.*, **2015**, *5*(1), 13214. https://doi.org/10.1038/srep13214
55. T. Tsirlina, Y. Feldman, M. Homyonfer, J. Sloan, J. L. Hutchison, and R. Tenne. *Fullerene Sci. Techn.*, **1998**, *6*(1), 157. https://doi.org/10.1080/10641229809350191
56. M. Nath, A. Govindaraj, and C. N. R. Rao. *Adv. Mater.*, **2001**, *13*(4), 283. https://doi.org/10.1002/1521-4095(200102)13:4<283::AID-ADMA283>3.0.CO;2-H
57. D. H. Galvan, J.-H. Kim, M. B. Maple, M. Avalos-Borja, and E. Adem. *Fullerene Sci. Techn.*, **2000**, *8*(3), 143. https://doi.org/10.1080/10641220009351405
58. M. A. Sriram and P. N. Kumta. *J. Mater. Chem.*, **1998**, *8*(11), 2441. https://doi.org/10.1039/A802564I
59. C. J. Carmalt, C. W. Dinnage, I. P. Parkin, A. J. P. White, and D. J. Williams. *Inorg. Chem.*, **2002**, *41*(14), 3668. https://doi.org/10.1021/ic020097l
60. A. Mansouri and N. Semagina. *ACS Appl. Nano Mater.*, **2018**, *1*(9), 4408. https://doi.org/10.1021/acsanm.8b01353
61. M. V. Nardi, M. Timpel, G. Ligorio, N. Zorn Morales, A. Chiappini, T. Toccoli, R. Verucchi, R. Ceccato, L. Pasquali, E. J. W. List-Kratochvil, A. Quaranta, and S. Dirè. *ACS Appl. Mater. Interfaces*, **2018**, *10*(40), 34392. https://doi.org/10.1021/acsami.8b12596
62. X. Guo, P. Yin, Z. Wang, and H. Yang. *J. Sol-Gel Sci. Technol.*, **2018**, *85*(1), 140. https://doi.org/10.1007/s10971-017-4531-8
63. X. Ren, Y. Yao, P. Ren, Y. Wang, and Y. Peng. *Mater. Lett.*, **2019**, *238*, 286. https://doi.org/10.1016/j.matlet.2018.12.036
64. T. Zhang, K. Fujisawa, F. Zhang, M. Liu, M. C. Lucking, R. N. Gontijo, Y. Lei, H. Liu, K. Crust, T. Granzier-Nakajima, H. Terrones, A. L. Elías, and M. Terrones. *ACS Nano*, **2020**, *14*(4), 4326. https://doi.org/10.1021/acsnano.9b09857
65. S. Qin, W. Lei, D. Liu, and Y. Chen. *Sci. Rep.*, **2014**, *4*(1), 7582. https://doi.org/10.1038/srep07582
66. Q. Zhang, L. Mei, X. Cao, Y. Tang, and Z. Zeng. *J. Mater. Chem. A*, **2020**, *8*(31), 15417. https://doi.org/10.1039/D0TA03727C

67. J. Ren, L. E. Camacho-Forero, D. Rossi, Y. Park, P. B. Balbuena, and D. H. Son. *Nanoscale*, **2016**, *8*(21), 11248. https://doi.org/10.1039/C6NR02125E
68. Y.-S. Kim, Y. Koyama, I. Tanaka, and H. Adachi. *Jpn. J. Appl. Phys.*, **1998**, *37*, 6440. https://doi.org/10.1143/JJAP.37.6440
69. T. C. Holgate, Y. Liu, D. Hitchcock, T. M. Tritt, and J. He. *J. Electron. Mater.*, **2013**, *42*(7), 1751. https://doi.org/10.1007/s11664-012-2410-1
70. C. Peng, H. Lyu, L. Wu, T. Xiong, F. Xiong, Z. Liu, Q. An, and L. Mai. *ACS Appl. Mater. Interfaces*, **2018**, *10*(43), 36988. https://doi.org/10.1021/acsami.8b12662
71. S. Mukherjee, J. Turnley, E. Mansfield, J. Holm, D. Soares, L. David, and G. Singh. *R. Soc. Open Sci.*, **2019**, *6*(8), 190437. https://doi.org/10.1098/rsos.190437
72. Y. Yu, G. Li, L. Huang, A. Barrette, Y.-Q. Cai, Y. Yu, K. Gundogdu, Y.-W. Zhang, and L. Cao. *ACS Nano*, **2017**, *11*(9), 9390. https://doi.org/10.1021/acsnano.7b04880
73. B. Chen, H. Li, H. Liu, X. Wang, F. Xie, Y. Deng, W. Hu, K. Davey, N. Zhao, and S.-Z. Qiao. *Adv. Energy Mater*, **2019**, *9*(30), 1901146. https://doi.org/10.1002/aenm.201901146
74. A. Golub, Y. Zubavichus, Y. Slovokhotov, and Y. Novikov. *Russ. Chem. Rev.*, **2003**, *72*(2), 123. https://doi.org/10.1070/RC2003v072n02ABEH000789
75. A. S. Goloveshkin, I. S. Bushmarinov, A. A. Korlyukov, M. I. Buzin, V. I. Zaikovskii, N. D. Lenenko, and A. S. Golub. *Langmuir*, **2015**, *31*(32), 8953. https://doi.org/10.1021/acs.langmuir.5b02344
76. A. S. Golub, I. B. Shumilova, Y. V. Zubavichus, M. Jahncke, G. Süss-Fink, M. Danot, and Y. N. Novikov. *J. Mater. Chem.*, **1997**, *7*(1), 163. https://doi.org/10.1039/A604733E
77. V. Nicolosi, M. Chhowalla, M. G. Kanatzidis, M. S. Strano, and J. N. Coleman. *Science*, **2013**, *340*(6139), 1226419. https://doi.org/10.1126/science.1226419
78. G. Zhou, P. Rajak, S. Susarla, P. M. Ajayan, R. K. Kalia, A. Nakano, and P. Vashishta. *Sci. Rep.*, **2018**, *8*(1), 16761. https://doi.org/10.1038/s41598-018-35008-z
79. D. Wang, F. Wu, Y. Song, C. Li, and L. Zhou. *J. Alloys Compd.*, **2017**, *728*, 1030. https://doi.org/10.1016/j.jallcom.2017.09.074
80. L. Zhang, C. Chen, J. Zhou, G. Yang, J. Wang, D. Liu, Z. Chen, and W. Lei. *Adv. Funct. Mater.*, **2020**, *30*(45), 2004139. https://doi.org/10.1002/adfm.202004139
81. J. Huster and H. F. Franzen. *J. Less. Common Met.*, **1985**, *113*(1), 119. https://doi.org/10.1016/0022-5088(85)90154-7
82. K. Selte and A. Kjekshus. *Acta Chem. Scand.*, **1964**, *18*(3), 697. https://doi.org/10.3891/acta.chem.scand.18-0697
83. V. M. Chapela and G. S. Parry. *Nature*, **1979**, *281*(5727), 134. https://doi.org/10.1038/281134a0
84. I. E. Ushakov, A. S. Goloveshkin, N. D. Lenenko, M. G. Ezernitskaya, A. A. Korlyukov, V. I. Zaikovskii, and A. S. Golub. *Cryst. Growth Des.*, **2018**, *18*(9), 5116. https://doi.org/10.1021/acs.cgd.8b00551
85. A. S. Goloveshkin, N. D. Lenenko, A. A. Korlyukov, and A. S. Golub. *ACS Omega*, **2020**, *5*(9), 4603. https://doi.org/10.1021/acsomega.9b04161
86. R. Eppinga and G. A. Wiegers. *Physica B+C*, **1980**, *99*(1), 121. https://doi.org/10.1016/0378-4363(80)90219-3
87. Z. Zhang, P. Yang, M. Hong, S. Jiang, G. Zhao, J. Shi, Q. Xie, and Y. Zhang. *Nanotechnology*, **2019**, *30*(18), 182002. https://doi.org/10.1088/1361-6528/aaff19
88. O. Rajora. *Phys. Status Solidi A*, **2006**, *203*(3), 493. https://doi.org/10.1002/pssa.200521041
89. M. Danot, J. L. Mansot, A. S. Golub, G. A. Protzenko, P. B. Fabritchnyi, Y. N. Novikov, and J. Rouxel. *Mater. Res. Bull.*, **1994**, *29*(8), 833. https://doi.org/10.1016/0025-5408(94)90003-5
90. B. G. Yacobi, F. W. Boswell, and J. M. Corbett. *Mater. Res. Bull.*, **1979**, *14*(8), 1033. https://doi.org/10.1016/0025-5408(79)90068-0

91. B. G. Yacobi, F. W. Boswell, and J. M. Corbett. *J. Phys. C: Solid State Phys.*, **1979**, *12*(11), 2189. https://doi.org/10.1088/0022-3719/12/11/028
92. T. Iwasaki, N. Kuroda, and Y. Nishina. *Synth. Met.*, **1983**, *6*, 157. https://doi.org/10.1016/0379-6779(83)90150-9
93. V. G. Pleshchev and N. V. Melnikova. *Phys. Solid State*, **2014**, *56*(9), 1761. https://doi.org/10.1134/S1063783414090236
94. V. G. Pleshchev, N. V. Selezneva, and N. V. Baranov. *Phys. Solid State*, **2013**, *55*(1), 21. https://doi.org/10.1134/S1063783413010253
95. V. G. Pleshchev, N. V. Baranov, N. V. Melnikova, and N. V. Selezneva. *Phys. Solid State*, **2012**, *54*(7), 1348. https://doi.org/10.1134/S1063783412070293
96. V. G. Pleshchev, N. V. Baranov, D. A. Shishkin, A. V. Korolev, and A. D. Gorlov. *Phys. Solid State*, **2011**, *53*(10), 2054. https://doi.org/10.1134/S1063783411100210
97. C. Huang, X. Wang, D. Wang, W. Zhao, K. Bu, J. Xu, X. Huang, Q. Bi, J. Huang, and F. Huang. *Chem. Mater.*, **2019**, *31*(13), 4726. https://doi.org/10.1021/acs.chemmater.9b00821
98. C. M. Fang, G. A. Wiegers, A. Meetsma, R. A. de Groot, and C. Haas. *Phys. B*, **1996**, *226*(4), 259. https://doi.org/10.1016/0921-4526(96)00271-2
99. A. Niazi and A. K. Rastogi. *Phys. B*, **1996**, *223/224*, 591. https://doi.org/10.1016/0921-4526(96)00182-2
100. A. van der Lee, S. van Smaalen, G. A. Wiegers, and J.L. de Boer. *Phys. Rev. B*, **1991**, *43*(12), 9420. https://doi.org/10.1103/PhysRevB.43.9420
101. H. J. M. Bouwmeester, A. van der Lee, S. van Smaalen, and G. A. Wiegers. *Phys. Rev. B*, **1991**, *43*(12), 9431. https://doi.org/10.1103/PhysRevB.43.9431
102. M. Nakayama, K. Miwa, H. Ikuta, H. Hinode, and M. Wakihara. *Chem. Mater.*, **2006**, *18*(21), 4996. https://doi.org/10.1021/cm060932n
103. J. Freund, G. Wortmann, W. Paulus, and W. Krone. *J. Alloys Compd.*, **1992**, *187*(1), 157. https://doi.org/10.1016/0925-8388(92)90530-M
104. M. Kars, A. Gomez-Herrero, A. Rebbah, and L. C. Otero-Diaz. *Mater. Res. Bull.*, **2009**, *44*(7), 1601. https://doi.org/10.1016/j.materresbull.2009.01.020
105. N. M. Toporova, E. M. Sherokalova, N. V. Selezneva, V. V. Ogloblichev, and N. V. Baranov. *J. Alloys Compd.*, **2020**, *848*, 156534. https://doi.org/10.1016/j.jallcom.2020.156534
106. H. Nobukane, Y. Tabata, T. Kurosawa, D. Sakabe, and S. Tanda. *J. Condens. Matter Phys.*, **2020**, *32*(16), 165803. https://doi.org/10.1088/1361-648X/ab622a
107. R. Eppinga, G. A. Sawatzky, C. Haas, and C. F. v. Bruggen. *J. Phys. C: Solid State Phys.*, **1976**, *9*(17), 3371. https://doi.org/10.1088/0022-3719/9/17/028
108. G. A. Scholz. *Solid State Ionics*, **1993**, *62*(3), 235. https://doi.org/10.1016/0167-2738(93)90377-F
109. L. J. Li, W. J. Lu, X. D. Zhu, X. B. Zhu, Z. R. Yang, W. H. Song, and Y. P. Sun. *J. Magn. Magn. Mater.*, **2011**, *323*(21), 2536. https://doi.org/10.1016/j.jmmm.2011.04.002
110. X. D. Zhu, Y. P. Sun, S. B. Zhang, H. C. Lei, L .J. Li, X. B. Zhu, Z. R. Yang, W. H. Song, and J. M. Dai. *Solid State Commun.*, **2009**, *149*(31), 1296. https://doi.org/10.1016/j.ssc.2009.05.007
111. S. I. Ali, S. Mondal, and S. van Smaalen. *Z. Anorg. Allg. Chem.*, **2015**, *641*(2), 464. https://doi.org/10.1002/zaac.201400335
112. T. Kanno, T. Matsumoto, K. Ichimura, T. Matsuura, and S. Tanda. *J. Low Temp. Phys.*, **2016**, *183*, 41-49. https://doi.org/10.1007/s10909-016-1502-3
113. D. Bhoi, S. Khim, W. Nam, B. S. Lee, C. Kim, B. G. Jeon, B. H. Min, S. Park, and K. H. Kim. *Sci. Rep.*, **2016**, *6*(1), 24068. https://doi.org/10.1038/srep24068
114. M. H. Zhou, X. C. Li, and C. Dong. *Supercond. Sci. Technol.*, **2018**, *31*(6), 065001. https://doi.org/10.1088/1361-6668/aab93d

115. P. Wang, R. Khan, Z. Liu, B. Zhang, Y. Li, S. Wang, Y. Wu, H. Zhu, Y. Liu, G. Zhang, D. Liu, S. Chen, L. Song, and Z. Sun. *Nano Res*., **2020**, *13*(2), 353. https://doi.org/10.1007/s12274-020-2613-3
116. X. Yao, Z. Liu, J. Shao, L. Zhang, S. Tan, C. Zhang, and Y. Zhang. *J. Supercond. Novel Magn*., **2016**, *29*(9), 2281. https://doi.org/10.1007/s10948-016-3597-9
117. W. Tremel, U. Wortmann, T. Vomhof, and W. Jeitschko. *Chem. Ber*., **1994**, *127*(1), 15. https://doi.org/10.1002/cber.19941270104
118. S. K. Srivastava and B. N. Avasthi. *J. Mater. Sci*., **1989**, *24*(6), 1919. https://doi.org/10.1007/BF02385399
119. W. Sienicki. *Mater. Chem. Phys*., **2001**, *68*(1), 119. https://doi.org/10.1016/S0254-0584(00)00285-6
120. V. G. Pleshchev and N. V. Selezneva. *Phys. Solid State*, **2019**, *61*(3), 339. https://doi.org/10.1134/S1063783419030259
121. P. A. Berseth, T. A. Hughes, R. Schneidmiller, A. Smalley, and D. C. Johnson. *Solid State Sci*., **2002**, *4*(5), 717. https://doi.org/10.1016/S1293-2558(02)01318-3
122. B. F. Mentzen and M. J. Sienko. *Inorg. Chem*., **1976**, *15*(9), 2198. https://doi.org/10.1021/ic50163a040
123. T. M. Herninda and C.-H. Ho. *Crystals*, **2020**, *10*(4), 327. https://doi.org/10.3390/cryst10040327
124. H. J. Lamfers, A. Meetsma, G. A. Wiegers, and J. L. de Boer. *J. Alloys Compd*., **1996**, *241*(1), 34. https://doi.org/10.1016/0925-8388(96)02313-4
125. A. Nipane, D. Karmakar, N. Kaushik, S. Karande, and S. Lodha. *ACS Nano*, **2016**, *10*(2), 2128. https://doi.org/10.1021/acsnano.5b06529
126. L. Bian, W. Gao, J. Sun, M. Han, F. Li, Z. Gao, L. Shu, N. Han, Z.-X. Yang, A. Song, Y. Qu, and J. C. Ho. *ChemCatChem*, **2018**, *10*(7), 1571. https://doi.org/10.1002/cctc.201701680
127. M. Chen, H. Nam, S. Wi, L. Ji, X. Ren, L. Bian, S. Lu, and X. Liang. *Appl. Phys. Lett*., **2013**, *103*(1)4, 142110. https://doi.org/10.1063/1.4824205
128. S. Kim, M. S. Choi, D. Qu, C. H. Ra, X. Liu, M. Kim, Y. J. Song, and W. J. Yoo. *2D Mater*., **2016**, *3*(3), 035002. https://doi.org/10.1088/2053-1583/3/3/035002
129. M. K. Agarwal and P. A. Wani. *Mater. Res. Bull*., **1979**, *14*(6), 825. https://doi.org/10.1016/0025-5408(79)90144-2
130. W. K. Hofmann, H. J. Lewerenz, and C. Pettenkofer. *Sol. Energy Mater*., **1988**, *17*(3), 165. https://doi.org/10.1016/0165-1633(88)90023-8
131. P. R. Bonneau and R. B. Kaner. *Inorg. Chem*., **1993**, *32*(26), 6084. https://doi.org/10.1021/ic00078a028
132. R. J. Mathew, C.-P. Lee, C.-A. Tseng, P. K. Chand, Y.-J. Huang, H.-T. Chen, K.-C. Ho, A. K. Anbalagan, C.-H. Lee, and Y.-T. Chen. *ACS Appl. Mater. Interfaces*, **2020**, *12*(31), 34815. https://doi.org/10.1021/acsami.0c07075
133. S.-J. Liu, Y.-C. Zou, X.-L. Shi, Q.-Z. Li, Y.-Z. Yang, W.-D. Liu, Z.-G. Chen, and J. Zou. *J. Alloys Compd*., **2019**, *777*, 926. https://doi.org/10.1016/j.jallcom.2018.11.068
134. Y. Sun, K. Fujisawa, Z. Lin, Y. Lei, J. S. Mondschein, M. Terrones, and R. E. Schaak. *J. Am. Chem. Soc*., **2017**, *139*(32), 11096. https://doi.org/10.1021/jacs.7b04443
135. F. J. Di Salvo, J. A. Wilson, B. G. Bagley, and J. V. Waszczak. *Phys. Rev. B*, **1975**, *12*(6), 2220. https://doi.org/10.1103/PhysRevB.12.2220
136. L. J. Li, W. J. Lu, X. D. Zhu, L. S. Ling, Z. Qu, and Y. P. Sun. *EPL Europhys. Lett*., **2012**, *97*(6), 67005. https://doi.org/10.1209/0295-5075/97/67005
137. M. Sachs, K. Bohnen, M. Conrad, B. Klein, C. Krug, C. Pietzonka, M. Schmid, S. Zörb, J. M. Gottfried, and B. Harbrecht. *J. Condens. Matter Phys*., **2018**, *30*, 385501. https://doi.org/10.1088/1361-648X/aad9c6
138. H. Tan, W. Hu, C. Wang, C. Ma, H. Duan, W. Yan, L. Cai, P. Guo, Z. Sun, Q. Liu, X. Zheng, F. Hu, and S. Wei. *Small*, **2017**, *13*(39), 1701389. https://doi.org/10.1002/smll.201701389

139. K. Qi, Z. Yuan, Y. Hou, R. Zhao, and B. Zhang. *Appl. Surf. Sci.*, **2019**, *483*, 688. https://doi.org/10.1016/j.apsusc.2019.04.021

140. Z. Cai, T. Shen, Q. Zhu, S. Feng, Q. Yu, J. Liu, L. Tang, Y. Zhao, J. Wang, B. Liu, and H.-M. Cheng. *Small*, **2020**, *16*(15), 1903181. https://doi.org/10.1002/smll.201903181

141. S. Ahmed, X.-Y. Carl Cui, X. Ding, P. P. Murmu, N. Bao, X. Geng, S. Xi, R. Liu, J. Kennedy, T. Wu, L. Wang, K. Suzuki, J. Ding, X. Chu, S. R. Clastinrusselraj Indirathankam, M. Peng, A. Vinu, S. P. Ringer, and J. Yi. *ACS Appl. Mater. Interfaces*, **2020**, *12*(52), 58140. https://doi.org/10.1021/acsami.0c18150

142. J. Pan, C. Song, X. Wang, X. Yuan, Y. Fang, C. Guo, W. Zhao, and F. Huang. *Inorg. Chem. Front.*, **2017**, *4*(11), 1895. https://doi.org/10.1039/C7QI00432J

143. X. Shi, M. Fields, J. Park, J. M. McEnaney, H. Yan, Y. Zhang, C. Tsai, T. F. Jaramillo, R. Sinclair, J. K. Nørskov, and X. Zheng. *Energy Environ. Sci.*, **2018**, *11*(8), 2270. https://doi.org/10.1039/C8EE01111G

144. J. Suh, T.-E. Park, D.-Y. Lin, D. Fu, J. Park, H. J. Jung, Y. Chen, C. Ko, C. Jang, Y. Sun, R. Sinclair, J. Chang, S. Tongay, and J. Wu. *Nano Lett.*, **2014**, *14*(12), 6976. https://doi.org/10.1021/nl503251h

145. D. Ghoshal, R. Kumar, and N. Koratkar. *Inorg. Chem. Commun.*, **2021**, *123*, 108329. https://doi.org/10.1016/j.inoche.2020.108329

146. S. A. Dalmatova, A. D. Fedorenko, L. N. Mazalov, I. P. Asanov, A. Y. Ledneva, M. S. Tarasenko, A. N. Enyashin, V. I. Zaikovskii, and V. E. Fedorov. *Nanoscale*, **2018**, *10*(21), 10232. https://doi.org/10.1039/C8NR01661E

147. H. Luo, W. Xie, E. Seibel, and R. Cava. *J. Condens. Matter Phys.*, **2015**, *27*, 365701. https://doi.org/10.1088/0953-8984/27/36/365701

148. P. Fazekas and E. Tosatti. *Physica B+C*, **1980**, *99*(1), 183. https://doi.org/10.1016/0378-4363(80)90229-6

149. P. Fazekas and E. Tosatti. *Philos. Mag. B*, **1979**, *39*(3), 229. https://doi.org/10.1080/13642817908245359

150. F. J. Di Salvo, J. A. Wilson, and J. V. Waszczak. *Phys. Rev. Lett.*, **1976**, *36*(15), 885. https://doi.org/10.1103/PhysRevLett.36.885

151. Y. Fujisawa, T. Shimabukuro, H. Kojima, K. Kobayashi, S. Demura, and H. Sakata. *J. Phys. Conf. Ser.*, **2017**, *871*, 012003. https://doi.org/10.1088/1742-6596/871/1/012003

152. Y. Tison, H. Martinez, I. Baraille, M. Loudet, and D. Gonbeau. *Surface Sci.*, **2004**, *563*, 83. https://doi.org/10.1016/j.susc.2004.05.134

153. H. Fujimoto and H. Ozaki. *Solid State Commun.*, **1984**, *49*(12), 1117. https://doi.org/10.1016/0038-1098(84)91043-3

154. H. Bando, K. Koizumi, Y. Miyahara, and H. Ozaki. *J. Condens. Matter Phys.*, **2000**, *12*(19), 4353. https://doi.org/10.1088/0953-8984/12/19/306

155. G. E. Yakovleva, A. I. Romanenko, A. S. Berdinsky, V. A. Kuznetsov, A. Y. Ledneva, S. B. Artemkina, and V. E. Fe dorov. *Semiconductors*, **2017**, *51*(6), 725. https://doi.org/10.1134/S1063782617060288

156. G. E. Yakovleva, A. I. Romanenko, A. Y. Ledneva, V. A. Belyavin, V. A. Kuznetsov, A. S. Berdinsky, A. T. Burkov, P. P. Konstantinov, S. V. Novikov, M.-K. Han, S.-J. Kim, and V. E. Fedorov. *J. Am. Ceram. Soc.*, **2019**, *102*(10), 6060. https://doi.org/10.1111/jace.16455

157. V. E. Fedorov, N. V. Podberezskaya, A. V. Mischenko, G. F. Khudorozko, and I. P. Asanov. *Mater. Res. Bull.*, **1986**, *21*(11), 1335. https://doi.org/10.1016/0025-5408(86)90068-1

158. B. E. Brown. *Acta Crystallogr.*, **1966**, *20*(2), 268. https://doi.org/10.1107/S0365110X66000513

159. H.-V. Wong, R. Millett, J. S. O. Evans, S. Barlow, and D. O′Hare. *Chem. Mater.*, **1995**, *7*(1), 210. https://doi.org/10.1021/cm00049a032

160. Y. Koh, S. Cho, J. Lee, L.-X. Yang, Y. Zhang, C. He, F. Chen, D.-L. Feng, M. Arita, K. Shimada, H. Namatame, M. Taniguchi, and C. Kim. *Jpn. J. Appl. Phys.*, **2013**, *52*(10S), 10MC15. https://doi.org/10.7567/JJAP.52.10MC15

161. T. Danz, Q. Liu, X. D. Zhu, L. H. Wang, S. W. Cheong, I. Radu, C. Ropers, and R. I. Tobey. *J. Condens. Matter Phys.*, **2016**, *28*(35), 356002. https://doi.org/10.1088/0953-8984/28/35/356002

162. A. Mendiboure, C. Delmas, and P. Hagenmuller. *Mater. Res. Bull.*, **1984**, *19*(10), 1383. https://doi.org/10.1016/0025-5408(84)90204-6
163. S. I. Ali, S. Mondal, S. J. Prathapa, S. van Smaalen, S. Zörb, and B. Harbrecht. *Z. Anorg. Allg. Chem.*, **2012**, *638*(15), 2625. https://doi.org/10.1002/zaac.201200314
164. V. Antal, V. Kavečanský, J. Kačmarčík, and P. Diko. *Phys. C*, **2017**, *539*, 35. https://doi.org/10.1016/j.physc.2017.06.007
165. A. S. Shkvarin, A. A. Titov, M. S. Postnikov, J. R. Plaisier, L. Gigli, M. Gaboardi, A. N. Titov, and E. G. Shkvarina. *J. Mol. Struct.*, **2020**, *1205*, 127644. https://doi.org/10.1016/j.molstruc.2019.127644
166. X. F. Li, M. W. Lin, L. Basile, S. M. Hus, A. A. Puretzky, J. Lee, Y. C. Kuo, L. Y. Chang, K. Wang, J. C. Idrobo, A. P. Li, C. H. Chen, C. M. Rouleau, D. B. Geohegan, and K. Xiao. *Adv. Mater.*, **2016**, *28*(37), 8240. https://doi.org/10.1002/adma.201601991
167. S. M. Oliver, R. Beams, S. Krylyuk, I. Kalish, A. K. Singh, A. Bruma, F. Tavazza, J. Joshi, I. R. Stone, S. J. Stranick, A. V. Davydov, and P. M. Vora. *2D Mater.*, **2017**, *4*(4), 045008. https://doi.org/10.1088/2053-1583/aa7a32
168. E. Revolinsky and D. Beerntsen. *J. Appl. Phys.*, **1964**, *35*(7), 2086. http://doi.org/10.1063/1.1702795
169. K.-A. N. Duerloo and E. J. Reed. *ACS Nano*, **2016**, *10*(1), 289. https://doi.org/10.1021/acsnano.5b04359
170. D. Rhodes, D. A. Chenet, B. E. Janicek, C. Nyby, Y. Lin, W. Jin, D. Edelberg, E. Mannebach, N. Finney, A. Antony, T. Schiros, T. Klarr, A. Mazzoni, M. Chin, Y. C. Chiu, W. Zheng, Q. R. Zhang, F. Ernst, J. I. Dadap, X. Tong, J. Ma, R. Lou, S. Wang, T. Qian, H. Ding, R. M. Osgood, D. W. Paley, A. M. Lindenberg, P. Y. Huang, A. N. Pasupathy, M. Dubey, J. Hone, and L. Balicas. *Nano Lett.*, **2017**, *17*(3), 1616. https://doi.org/10.1021/acs.nanolett.6b04814
171. Q. Zhao, Y. Guo, Y. Zhou, X. Xu, Z. Ren, J. Bai, and X. Xu. *J. Phys. Chem. C*, **2017**, *121*(42), 23744. https://doi.org/10.1021/acs.jpcc.7b07939
172. Y.-C. Kao, T. Huang, D.-Y. Lin, Y.-S. Huang, K.-K. Tiong, H.-Y. Lee, J.-M. Lin, H.-S. Sheu, and C.-M. Lin. *J. Chem. Phys.*, **2012**, *137*(2), 024509. https://doi.org/10.1063/1.4733985
173. P. Yen, Y.-S. Huang, and K. Tiong. *J. Condens. Matter Phys.*, **2004**, *16*, 2171. http://doi.org/10.1088/0953-8984/16/12/025
174. R. H. Friend and A. D. Yoffe. *Adv. Phys.*, **1987**, *36*(1), 1. https://doi.org/10.1080/00018738700101951
175. H. Xiang, B. Xu, W. Zhao, Y. Xia, J. Yin, X. Zhang, and Z. Liu. *RSC Adv.*, **2019**, *9*(24), 13561. https://doi.org/10.1039/C9RA01218D
176. P. C. Klipstein, D. R. P. Guy, E. A. Marseglia, J. I. Meakin, R. H. Friend, and A. D. Yoffe. *J. Phys. C: Solid State Phys.*, **1986**, *19*(25), 4953. https://doi.org/10.1088/0022-3719/19/25/012
177. J. Augustin, V. Eyert, T. Böker, W. Frentrup, H. Dwelk, C. Janowitz, and R. Manzke. *Phys. Rev. B*, **2000**, *62*(16), 10812. https://doi.org/10.1103/PhysRevB.62.10812
178. M. N. Ali, J. Xiong, S. Flynn, J. Tao, Q. D. Gibson, L. M. Schoop, T. Liang, N. Haldolaarachchige, M. Hirschberger, N. P. Ong, and R. J. Cava. *Nature*, **2014**, *514*(7521), 205. https://doi.org/10.1038/nature13763
179. D. H. Keum, S. Cho, J. H. Kim, D.-H. Choe, H.-J. Sung, M. Kan, H. Kang, J.-Y. Hwang, S. W. Kim, H. Yang, K. J. Chang, and Y. H. Lee. *Nat. Phys.*, **2015**, *11*(6), 482. https://doi.org/10.1038/nphys3314
180. S. Song, D. H. Keum, S. Cho, D. Perello, Y. Kim, and Y. H. Lee. *Nano Lett.*, **2016**, *16*(1), 188. https://doi.org/10.1021/acs.nanolett.5b03481
181. Y. Qi, P. G. Naumov, M. N. Ali, C. R. Rajamathi, W. Schnelle, O. Barkalov, M. Hanfland, S.-C. Wu, C. Shekhar, Y. Sun, V. Süß, M. Schmidt, U. Schwarz, E. Pippel, P. Werner, R. Hillebrand, T. Förster, E. Kampert, S. Parkin, R. J. Cava, C. Felser, B. Yan, and S. A. Medvedev. *Nat. Commun.*, **2016**, *7*(1), 11038. https://doi.org/10.1038/ncomms11038
182. M. Kertesz and R. Hoffmann. *J. Am. Chem. Soc.*, **1984**, *106*(12), 3453. https://doi.org/10.1021/ja00324a012
183. S. Tongay, H. Sahin, C. Ko, A. Luce, W. Fan, K. Liu, J. Zhou, Y.-S. Huang, C.-H. Ho, J. Yan, D. F. Ogletree, S. Aloni, J. Ji, S. Li, J. Li, F. M. Peeters, and J. Wu. *Nat. Commun.*, **2014**, *5*(1), 3252. https://doi.org/10.1038/ncomms4252

184. C. H. Ho, Y. S. Huang, K. K. Tiong, and P. C. Liao. *Phys*. *Rev*. *B*, **1998**, *58*(24), 16130. https://doi.org/10.1103/PhysRevB.58.16130

185. K. F. Mak, C. Lee, J. Hone, J. Shan, and T. F. Heinz. *Phys*. *Rev*. *Lett*., **2010**, *105*(13), 136805. https://doi.org/10.1103/PhysRevLett.105.136805

186. S. Z. Butler, S. M. Hollen, L. Cao, Y. Cui, J. A. Gupta, H. R. Gutiérrez, T. F. Heinz, S. S. Hong, J. Huang, A. F. Ismach, E. Johnston-Halperin, M. Kuno, V. V. Plashnitsa, R. D. Robinson, R. S. Ruoff, S. Salahuddin, J. Shan, L. Shi, M. G. Spencer, M. Terrones, W. Windl, and J. E. Goldberger. *ACS Nano*, **2013**, *7*(4), 2898. https://doi.org/10.1021/nn400280c

187. J. S. Ross, P. Klement, A. M. Jones, N. J. Ghimire, J. Yan, D. G. Mandrus, T. Taniguchi, K. Watanabe, K. Kitamura, W. Yao, D. H. Cobden, and X. Xu. *Nat. Nanotechnol.*, **2014**, *9*(4), 268. https://doi.org/10.1038/nnano.2014.26

188. H. Wang, L. Yu, Y.-H. Lee, Y. Shi, A. Hsu, M. L. Chin, L.-J. Li, M. Dubey, J. Kong, and T. Palacios. *Nano Lett*., **2012**, *12*(9), 4674. https://doi.org/10.1021/nl302015v

189. R. S. Sundaram, M. Engel, A. Lombardo, R. Krupke, A. C. Ferrari, P. Avouris, and M. Steiner. *Nano Lett*., **2013**, *13*(4), 1416. https://doi.org/10.1021/nl400516a

190. M. J. Mleczko, C. Zhang, H. R. Lee, H.-H. Kuo, B. Magyari-Köpe, R. G. Moore, Z.-X. Shen, I. R. Fisher, Y. Nishi, and E. Pop. *Sci. Adv*., **2017**, *3*(8), e1700481. https://doi.org/10.1126/sciadv.1700481

191. J.-A. Yan, M. A. D. Cruz, B. Cook, and K. Varga. *Sci. Rep*., **2015**, *5*(1), 16646. https://doi.org/10.1038/srep16646

192. S. Li, M. Zhou, X. Wang, F. Zheng, X. Shao, and P. Zhang. *Phys*. *Lett*. *A*, **2020**, *384*(23), 126534. https://doi.org/10.1016/j.physleta.2020.126534

193. D. Qin, X.-J. Ge, G.. Ding, G Gao, and J.-T. Lü. *RSC Adv*., **2017**, *7*(75), 47243. https://doi.org/10.1039/C7RA08828K

194. H. Y. Lv, W. J. Lu, D. F. Shao, H. Y. Lu, and Y.P. Sun. *J. Mater*. *Chem*. *C*, **2016**, *4*(20), 4538. https://doi.org/10.1039/C6TC01135G

195. H. Guo, N. Lu, L. Wang, X. Wu, and X. C. Zeng. *J. Phys*. *Chem*. *C*, **2014**, *118*(13), 7242. https://doi.org/10.1021/jp501734s

196. J. Qi, Y. W. Lan, A. Stieg, J.-H. Chen, Y.-L. Zhong, L. Li, C.-D. Chen, Y. Zhang, Kang, and K. Wang. *Nat*. *Commun*., **2015**, *6*, 7430. https://doi.org/10.1038/ncomms8430

197. V. A. Kuznetsov, A. S. Berdinsky, A. Y. Ledneva, S. B. Artemkina, M. S. Tarasenko, and V. E. Fedorov. *Sens*. *Actuator A: Phys*., **2015**, *226*, 5. https://doi.org/10.1016/j.sna.2015.02.020

198. J. A. Woollam and R. B. Somoano. *Phys*. *Rev*. *B*, **1976**, *13*(9), 3843. https://doi.org/10.1103/PhysRevB.13.3843

199. J. T. Ye, Y. J. Zhang, R. Akashi, M. S. Bahramy, R. Arita, and Y. Iwasa. *Science*, **2012**, *338*(6111), 1193. http://doi.org/10.1126/science.1228006

200. C. Habenicht, J. Simon, M. Richter, R. Schuster, M. Knupfer, and B. Büchner. *Phys*. *Rev*. *Mater*., **2020**, *4*(6), 064002. https://doi.org/10.1103/PhysRevMaterials.4.064002

201. P. Deniard, P. Chevalier, L. Trichet, and J. Rouxel. *Synth*. *Met*., **1983**, *5*(2), 141. https://doi.org/10.1016/0379-6779(83)90127-3

202. K. Nikonov, N. Ehlen, B. Senkovskiy, N. Saigal, A. Fedorov, A. Nefedov, C. Wöll, G. Di Santo, L. Petaccia, and A. Grüneis. *Dalton Trans*., **2018**, *47*(9), 2986. https://doi.org/10.1039/C7DT03756B

203. P. C. Klipstein, C. M. Pereira, and R. H. Friend. *Philos*. *Mag*. *B*, **1987**, *56*(5), 531. https://doi.org/10.1080/13642818708220162

204. D. Costanzo, S. Jo, H. Berger, and A. F. Morpurgo. *Nat*. *Nanotechnol*., **2016**, *11*(4), 339. https://doi.org/10.1038/nnano.2015.314

205. Y. Nakata, K. Sugawara, A. Chainani, K. Yamauchi, K. Nakayama, S. Souma, P. Y. Chuang, C. M. Cheng, T. Oguchi, K. Ueno, T. Takahashi, and T. Sato. *Phys*. *Rev*. *Mater*., **2019**, *3*(7), 071001. https://doi.org/10.1103/PhysRevMaterials.3.071001

206. E. Navarro-Moratalla, J. O. Island, S. Mañas-Valero, E. Pinilla-Cienfuegos, A. Castellanos-Gomez, J. Quereda, G. Rubio-Bollinger, L. Chirolli, J. A. Silva-Guillén, N. Agraït, G. A. Steele, F. Guinea, H. S. J. van der Zant, and E. Coronado. *Nat. Commun.*, **2016**, *7*, 11043. https://doi.rg/10.1038/ncomms11043
207. T. Eknapakul, I. Fongkaew, S. Siriroj, W. Jindata, S. Chaiyachad, S. K. Mo, S. Thakur, L. Petaccia, H. Takagi, S. Limpijumnong, and W. Meevasana. *Phys. Rev. B*, **2018**, *97*(20), 201104. https://doi.org/10.1103/PhysRevB.97.201104
208. D. Hodul and M. J. Sienko. *Physica B+C*, **1980**, *99*(1), 215. https://doi.org/10.1016/0378-4363(80)90235-1
209. J. G. Smeggil and S. Bartram. *J. Solid State Chem.*, **1972**, *5*(3), 391. https://doi.org/10.1016/0022-4596(72)90083-7
210. D. T. Hodul and A. M. Stacy. *J. Phys. Chem. Solids*, **1985**, *46*(12), 1447. https://doi.org/10.1016/0022-3697(85)90084-8
211. G. Zhou, T. Xiong, Y. Shan, and L. Z. Liu. *J. Phys. D: Appl. Phys.*, **2019**, *52*(16), https://doi.org/10.1088/1361-6463/aaff47
212. G. C. Loh and R. Pandey. *Phys. Chem. Chem. Phys.*, **2015**, *17*(28), 18843. https://doi.org/10.1039/C5CP02593A
213. D. N. Gujarathi, G. K. Solanki, M. P. Deshpande, and M. K. Agarwal. *Mater. Sci. Semicond. Process.*, **2005**, *8*(5), 576. https://doi.org/10.1016/j.mssp.2005.07.001
214. J. Kang, S. Tongay, J. Li, and J. Wu. *J. Appl. Phys.*, **2013**, *113*(14), 143703. https://doi.org/10.1063/1.4799126
215. X. Zhao, Y. Gao, H. Zhang, H. Wang, T. Wang, and S. Wei. *J. Magn. Magn. Mater.*, **2019**, *479*, 192. https://doi.org/10.1016/j.jmmm.2019.02.029
216. G. H. Yousefi. *Mater. Lett.*, **1989**, *9*(1), 38. https://doi.org/10.1016/0167-577X(89)90128-6
217. K. O. Obodo, G. Gebreyesus, C. N. M. Ouma, J. T. Obodo, S. O. Ezeonu, D. P. Rai, and B. Bouhafs. *RSC Adv.*, **2020**, *10*(27), 15670. https://doi.org/10.1039/D0RA02464C
218. X. Ma, X. Zhao, N. Wu, Q. Xin, X. Liu, T. Wang, and S. Wei. *Solid State Commun.*, **2017**, *268*, 15. https://doi.org/10.1016/j.ssc.2017.09.012
219. X. Zhao, T. Wang, G. Wang, X. Dai, C. Xia, and L. Yang. *Appl. Surf. Sci.*, **2016**, *383*, 151. https://doi.org/10.1016/j.apsusc.2016.04.063
220. X. Zhao, C. Xia, T. Wang, X. Dai, and L. Yang. *J. Alloys Compd.*, **2016**, *689*, 302. https://doi.org/10.1016/j.jallcom.2016.07.331
221. D. Çakır, H. Sahin, and F. M. Peeters. *Phys. Chem. Chem. Phys.*, **2014**, *16*(31), 16771. https://doi.org/10.1039/C4CP02007C
222. K. O. Obodo, C. N. M. Ouma, J. T. Obodo, and M. Braun. *Phys. Chem. Chem. Phys.*, **2017**, *19*(29), 19050. https://doi.org/10.1039/C7CP03455E
223. C. N. M. Ouma, K. O. Obodo, C. Parlak, and G. O. Amolo. *Physica E*, **2020**, *123*, 114165. https://doi.org/10.1016/j.physe.2020.114165
224. P. C. Yen, M. J. Chen, Y. S. Huang, C. H. Ho, and K. K. Tiong. *J. Condens. Matter Phys.*, **2002**, *14*(18), 4737. https://doi.org/10.1088/0953-8984/14/18/308
225. D. O. Dumcenco, Y. S. Huang, C. H. Liang, and K. K. Tiong. *J. Appl. Phys.*, **2007**, *102*(8), 083523. https://doi.org/10.1063/1.2798923
226. R. E. Peierls. Quantum Theory of Solids. Oxford: Clarendon Press, **1956**.
227. J. A. Wilson, F. J. Di Salvo, and S. Mahajan. *Adv. Phys.*, **1975**, *24*(2), 117. https://doi.org/10.1080/00018737500101391
228. A. Spijkerman, J. L. de Boer, A. Meetsma, G. A. Wiegers, and S. van Smaalen. *Phys. Rev. B*, **1997**, *56*(21), 13757. https://doi.org/10.1103/PhysRevB.56.13757
229. W. Wen, C. Dang, and L. Xie. *Chin. Phys. B*, **2019**, *28*(5), 058504. http:/doi.org/10.1088/1674-1056/28/5/058504
230. M. Yoshida, Y. Zhang, J. Ye, R. Suzuki, Y. Imai, S. Kimura, A. Fujiwara, and Y. Iwasa. *Sci. Rep.*, **2014**, *4*(1), 7302. https://doi.org/10.1038/srep07302

231. D. F. Shao, R. C. Xiao, W. J. Lu, H. Y. Lv, J. Y. Li, X. B. Zhu, and Y. P. Sun. *Phys. Rev. B*, **2016**, *94*(12), 125126. https://doi.org/10.1103/PhysRevB.94.125126

232. C. H. Chen, J. M. Gibson, and R. M. Fleming. *Phys. Rev. Lett.*, **1981**, *47*(10), 723. https://doi.org/10.1103/PhysRevLett.47.723

233. Y. Koyama, Z. P. Zhang, and H. Sato. *Phys. Rev. B*, **1987**, *36*(7), 3701. https://doi.org/10.1103/PhysRevB.36.3701

234. M. Yoshida, J. Ye, Y. Zhang, Y. Imai, S. Kimura, A. Fujiwara, T. Nishizaki, N. Kobayashi, M. Nakano, and Y. Iwasa. *Nano Lett.*, **2017**, *17*(9), 5567. https://doi.org/10.1021/acs.nanolett.7b02374

235. K. Kobayashi and H. Yasuda. *Phys. Rev. B*, **2016**, *94*, 201409(R). https://doi.org/10.1103/PhysRevB.94.201409

236. L. Stojchevska, I. Vaskivskyi, T. Mertelj, P. Kusar, D. Svetin, S. Brazovskii, and D. Mihailovic. *Science*, **2014**, *344*(6180), 177. http://doi.org/10.1126/science.1241591

237. I. Vaskivskyi, I. A. Mihailovic, S. Brazovskii, J. Gospodaric, T. Mertelj, D. Svetin, P. Sutar, and D. Mihailovic. *Nat. Commun.*, **2016**, *7*(1), 11442. https://doi.org/10.1038/ncomms11442

238. H. Wang, Y. Chen, C. Zhu, X. Wang, H. Zhang, S. H. Tsang, H. Li, J. Lin, T. Yu, Z. Liu, and E. H. T. Teo. *Adv. Funct. Mater.*, **2020**, *30*(34), 2001903. https://doi.org/10.1002/adfm.202001903

239. S. Sun, L. Wei, Z. Li, G. Cao, Y. Liu, W. J. Lu, Y. P. Sun, H. Tian, H. Yang, and J. Li. *Phys. Rev. B*, **2015**, *92*(22), 224303. https:/doi.org/10.1103/PhysRevB.92.224303

240. D. Wu, Y. Ma, Y. Niu, Q. Liu, T. Dong, S. Zhang, J. Niu, H. Zhou, J. Wei, Y. Wang, Z. Zhao, and N. Wang. *Sci. Adv.*, **2018**, *4*(8), eaao3057. https://doi.org/10.1126/sciadv.aao3057

241. C. Dang, M. Guan, S. Hussain, W. Wen, Y. Zhu, L. Jiao, S. Meng, and L. Xie. *Nano Lett.*, **2020**, *20*(9), 6725. https://doi.org/10.1021/acs.nanolett.0c02613

242. L. Ma, C. Ye, Y. Yu, X. F. Lu, X. Niu, S. Kim, D. Feng, D. Tománek, Y.-W. Son, X. H. Chen, and Y. Zhang. *Nat. Commun.*, **2016**, *7*(1), 10956. https://doi.org/10.1038/ncomms10956

243. K. Zhang, Z.-Y. Cao, and X.-J. Chen. *Appl. Phys. Lett.*, **2019**, *114*(14), 141901. https://doi.org/10.1063/1.5086951

244. Y. Deng, Y. Lai, X. Zhao, X. Wang, C. Zhu, K. Huang, C. Zhu, J. Zhou, Q. Zeng, R. Duan, Q. Fu, L. Kang, Y. Liu, S. J. Pennycook, X. R. Wang, and Z. Liu. *J. Am. Chem. Soc.*, **2020**, *142*(6), 2948. https://doi.org/10.1021/jacs.9b11673

245. F. L. Givens and G. E. Fredericks. *J. Phys. Chem. Solids*, **1977**, *38*(12), 1363. https://doi.org/10.1016/0022-3697(77)90008-7

246. X. Zhu, Y. Sun, X. Zhu, X. Luo, B. Wang, G. Li, Z. Yang, W. Song, and J. Dai. *J. Cryst. Growth*, **2008**, *311*, 218. https://doi.org/10.1016/j.jcrysgro.2008.10.023

247. L. Fang, Y. Wang, P. Y. Zou, L. Tang, Z. Xu, H. Chen, C. Dong, L. Shan, and H. H. Wen. *Phys. Rev. B*, **2005**, *72*(1), 014534. https://doi.org/10.1103/PhysRevB.72.014534

248. Z. Muhammad, K. Mu, H. Lv, C. Wu, Z. ur Rehman, M. Habib, Z. Sun, X. Wu, and L. Song. *Nano Res.*, **2018**, *11*(9), 4914. https://doi.org/10.1007/s12274-018-2081-1

249. Z. ur Rehman, S. Wang, M. A. Lawan, S. Zareen, O. A. Moses, W. Zhu, X. Wu, Z. Sun, and L. Song. *Appl. Phys. Lett.*, **2019**, *115*(21), 213102. https://doi.org/10.1063/1.5115280

250. S. Mangelsen, P. G. Naumov, O. I. Barkalov, S. A. Medvedev, W. Schnelle, M. Bobnar, S. Mankovsky, S. Polesya, C. Näther, H. Ebert, and W. Bensch. *Phys. Rev. B*, **2017**, *96*(20), 205148. https://doi.org/10.1103/PhysRevB.96.205148

251. Y. Aoki, T. Sambongi, F. Levy, and H. Berger. *J. Phys. Soc. Jpn.*, **1996**, *65*(8), 2590. https://doi.org/10.1143/JPSJ.65.2590

252. B. Zhang, Z. Muhammad, P. Wang, S. Cui, Y. Li, S. Wang, Y. Wu, Z. Liu, H. Zhu, Y. Liu, G. Zhang, D. Liu, L. Song, and Z. Sun. *J. Phys. Chem. C*, **2020**, *124*(30), 16561. https://doi.org/10.1021/acs.jpcc.0c04168

253. Lucas E. Correa, Pedro P. Ferreira, Leandro R. de Faria, Thiago T. Dorini, Zachary Fisk, Milton S. Torikachvili, Luiz T. F. Eleno, and A. J. S. Machado. *Condens. Matter*, **2021**, https://arxiv.org/abs/2102.04812

254. Z. Muhammad, B. Zhang, H. Lv, H. Shan, Z. u. Rehman, S. Chen, Z. Sun, X. Wu, A. Zhao, and L. Song. *ACS Nano*, **2020**, *14*(1), 835. https://doi.org/10.1021/acsnano.9b07931

255. C. Battaglia, H. Cercellier, F. Clerc, L. Despont, M. G. Garnier, C. Koitzsch, P. Aebi, H. Berger, L. Forró, and C. Ambrosch-Draxl. *Phys. Rev. B*, **2005**, *72*(19), 195114. https://doi.org/10.1103/PhysRevB.72.195114

256. A. Vernes, H. Ebert, W. Bensch, W. Heid, and C. Näther. *J. Condens. Matter Phys.*, **1998**, *10*(4), 761. https://doi.org/10.1088/0953-8984/10/4/006

257. A. H. Barajas-Aguilar, J. C. Irwin, A. M. Garay-Tapia, T. Schwarz, F. Paraguay Delgado, P. M. Brodersen, R. Prinja, N. Kherani, and S. J. Jiménez Sandoval. *Sci. Rep.*, **2018**, *8*(1), 16984. https://doi.org/10.1038/s41598-018-35308-4

258. R. Ang, Y. Tanaka, E. Ieki, K. Nakayama, T. Sato, L. J. Li, W. J. Lu, Y. P. Sun, and T. Takahashi. *Phys. Rev. Lett.*, **2012**, *109*(17), 176403. https://doi.org/10.1103/PhysRevLett.109.176403

259. M. Imada, A. Fujimori, and Y. Tokura. *Rev. Mod. Phys.*, **1998**, *70*(4), 1039. https://doi.org/10.1103/RevModPhys.70.1039

260. M. Fujioka, N. Kubo, M. Nagao, R. Msiska, N. Shirakawa, S. Demura, H. Sakata, H. Kaiju, and J. Nishii. *J. Ceram. Soc. Jpn.*, **2018**, *126*(12), 963. https://doi.org/10.2109/jcersj2.18148

261. Y. Sheng, T. Chen, Y. Lu, R.-J. Chang, S. Sinha, and J. H. Warner. *ACS Nano*, **2019**, *13*(4), 4530. https://doi.org/10.1021/acsnano.9b00211

262. M. P. Deshpande, J. B. Patel, N. N. Pandya, M. N. Parmar, and G. K. Solanki. *Mater. Chem. Phys.*, **2009**, *117*(2), 350. https://doi.org/10.1016/j.matchemphys.2009.05.058

263. S. Y. Hu, M. C. Cheng, K. K. Tiong, and Y. S. Huang. *J. Condens. Matter Phys.*, **2005**, *17*(23), 3575. https://doi.org/10.1088/0953-8984/17/23/010

264. K. K. Tiong, Y. S. Huang, and C. H. Ho. *J. Alloys Compd.*, **2001**, *317/318*, 208. https://doi.org/10.1016/S0925-8388(00)01327-X

265. G. E. Yakovleva, A. I. Romanenko, A. S. Berdinsky, V. A. Kuznetsov, A. Y. Ledneva, and A. Y. Fedorov. *J. Sib. Fed. Univ.: Math. Phys.*, **2018**, *11*(4), 459. https://doi.org/10.17516/1997-1397-2018-11-4-459-464

266. V. E. Fedorov, N. G. Naumov, A. N. Lavrov, M. S. Tarasenko, S. B. Artemkina, A. I. Romanenko, and M. V. Medvedev. In: 36th International Convention on Information and Communication Technology, Electronics and Microelectronics (MIPRO): Conf. Proc., Opatija, Croatia, May 20-24, 2013. IEEE, **2013**, 11-14.

267. W. T. Hick. *J. Electrochem. Soc.*, **1964**, *111*(9), 1058. https://doi.org/10.1149/1.2426317

268. H. Sakai, K. Ikeura, M. S. Bahramy, N. Ogawa, D. Hashizume, J. Fujioka, Y. Tokura, and S. Ishiwata. *Sci. Adv.*, **2016**, *2*(11), e1601378. http://doi.org/10.1126/sciadv.1601378

269. M. Abdulsalam and D. Joubert. *Comput. Mater. Sci.*, **2016**, *115*, 177. https://doi.org/10.1016/j.commatsci.2015.12.053

270. S. Y. Hu, S. C. Lin, K. K. Tiong, P. C. Yen, Y. S. Huang, C. H. Ho, and P. C. Liao. *J. Alloys Compd.*, **2004**, *383*(1), 63. https://doi.org/10.1016/j.jallcom.2004.04.009

271. S. Hu, C. Liang, K. Tiong, Y.-S. Huang, and Y. Lee. *J. Electrochem. Soc.*, **2006**, *153*, J100. https://doi.org/10.1149/1.2209589

272. D. Joseph, M. Navaneethan, R. Abinaya, S. Harish, J. Archana, S. Ponnusamy, K. Hara, and Y. Hayakawa. *Appl. Surf. Sci.*, **2020**, *505*, 144066. https://doi.org/10.1016/j.apsusc.2019.144066

273. S. Ashraf, V. Forsberg, C. G. Mattsson, and G. Thungström. *Materials*, **2019**, *12*(21), 3521. https://doi.org/10.3390/ma12213521

274. M. Piao, J. Chu, X. Wang, Y. Chi, H. Zhang, C. Li, H. Shi, and M.-K. Joo. *Nanotechnology*, **2017**, *29*(2), 025705. https://doi.org/10.1088/1361-6528/aa9bfe

275. W. Ding, X. Li, F. Jiang, P. Liu, P. Liu, S. Zhu, G. Zhang, C. Liu, and J. Xu. *J. Mater. Chem. C*, **2020**, *8*(6), 1909. https://doi.org/10.1039/C9TC06012J

276. J. Li, Q. Shi, J. A. Röhr, H. Wu, B. Wu, Y. Guo, Q. Zhang, C. Hou, Y. Li, and H. Wang. *Adv. Funct. Mater.*, **2020**, *30*(36), 2002508. https://doi.org/10.1002/adfm.202002508

277. G. E. Yakovleva, A. I. Romanenko, A. S. Berdinsky, A. Y. Ledneva, V. A. Kuznetsov, M. K. Han, S. J. Kim, and V. E. Fedorov. In: 39th International Convention on Information and Communication Technology, Electronics and Microelectronics (MIPRO): Conf. Proc., Opatija, Croatia, May 30-June 3, 2016. IEEE, **2016**, 5-9.
278. D. Suh, D. Lee, C. Kang, I.-J. Shon, W. Kim, and S. Baik. *J. Mater. Chem.*, **2012**, *22*(40), 21376. https://doi.org/10.1039/C2JM34510B
279. V. G. Pleshchev and N. V. Selezneva. *Phys. Solid State*, **2018**, *60*(2), 250. https://doi.org/10.1134/S1063783418020191
280. P. M. Shand, C. Cooling, C. Mellinger, J. J. Danker, T. E. Kidd, K. R. Boyle, and L. H. Strauss. *J. Magn. Magn. Mater.*, **2015**, *382*, 49. https://doi.org/10.1016/j.jmmm.2015.01.023
281. H. Zhang, W. Wei, G. Zheng, J. Lu, M. Wu, X. Zhu, J. Tang, W. Ning, Y. Han, L. Ling, J. Yang, W. Gao, Y. Qin, and M. Tian. *Appl. Phys. Lett.*, **2018**, *113*(7), 072402. https://doi.org/10.1063/1.5034502
282. Z. Muhammad, H. Lv, C. Wu, M. Habib, Z. ur Rehman, R. Khan, S. Chen, X. Wu, and L. Song. *Mater. Res. Express.*, **2018**, *5*(4), 046110. https://doi.org/10.1088/2053-1591/aabe65
283. B. Yang, H. Zheng, R. Han, X. Du, and Y. Yan. *RSC Adv.*, **2014**, *4*(97), 54335. https://doi.org/10.1039/C4RA08513B
284. X. Zhao, T. Wang, C. Xia, X. Dai, S. Wei, and L. Yang. *J. Alloys Compd.*, **2017**, *698*, 611. https://doi.org/10.1016/j.jallcom.2016.12.260
285. H. Li, Q. Zhang, C. C. R. Yap, B. K. Tay, T. H. T. Edwin, A. Olivier, and D. Baillargeat. *Adv. Funct. Mater.*, **2012**, *22*(7), 1385. https://onlinelibrary.wiley.com/journal/16163028
286. P. Tonndorf, R. Schmidt, P. Böttger, X. Zhang, J. Börner, A. Liebig, M. Albrecht, C. Kloc, O. Gordan, D. R. T. Zahn, S. Michaelis de Vasconcellos, and R. Bratschitsch. *Opt. Express*, **2013**, *21*(4), 4908. https://doi.org/10.1364/oe.21.004908
287. P. Hajiyev, C. Cong, C. Qiu, and T. Yu. *Sci. Rep.*, **2013**, *3*(1), 2593. https://doi.org/10.1038/srep02593
288. S. Mañas-Valero, V. García-López, A. Cantarero, and M. Galbiati. *Appl. Sci.*, **2016**, *6*(9), 264. https://doi.org/10.3390/app6090264
289. J. Ibáñez, T. Woźniak, F. Dybala, R. Oliva, S. Hernández, and R. Kudrawiec. *Sci. Rep.*, **2018**, *8*(1), 12757. https://doi.org/10.1038/s41598-018-31051-y
290. A. Cingolani, M. Lugarà, and F. Lévy. *Phys. Scr.*, **1988**, *37*(3), 389. https://doi.org/10.1088/0031-8949/37/3/015
291. A. Cruz, Z. Mutlu, M. Ozkan, and C. S. Ozkan. *MRS Commun.*, **2018**, *8*(3), 1191. https://doi.org/10.1557/mrc.2018.185
292. X. Zhang, X.-F. Qiao, W. Shi, J.-B. Wu, D.-S. Jiang, and P.-H. Tan. *Chem. Soc. Rev.*, **2015**, *44*(9), 2757. https://doi.org/10.1039/C4CS00282B
293. D. Wolverson, S. Crampin, A. S. Kazemi, A. Ilie, and S. J. Bending. *ACS Nano*, **2014**, *8*(11), 11154. https://doi.org/10.1021/nn5053926
294. M. Hangyo, S.-I. Nakashima, and A. Mitsuishi. *Ferroelectrics*, **1983**, *52*(1), 151. http://doi.org/10.1080/00150198308208248
295. J. Gao, J. Si, X. Luo, J. Yan, F. Chen, G. Lin, L. Hu, R. Zhang, P. Tong, W. Song, X. Zhu, W. Lu, and Y. Sun. *Phys. Rev. B*, **2018**, *98*, 224104. https://doi.org/10.1103/PhysRevB.98.224104
296. D. Wolverson and L. S. Hart. *Nanoscale Res. Lett.*, **2016**, *11*(1), 250. https://doi.org/10.1186/s11671-016-1459-9
297. R. He, Z. Ye, G. Ye, J. Van Baren, C. H. Lui, J.-A. Yan, X. Xi, I. H. Lu, and S. M. Leong. *2D Mater.*, **2016**, *3*(3), 7. https://doi.org/10.1088/2053-1583/3/3/031008
298. H. M. Hill, A. F. Rigosi, S. Krylyuk, J. Tian, N. V. Nguyen, A. V. Davydov, D. B. Newell, and A. R. Hight Walker. *Phys. Rev. B*, **2018**, *98*(16), 165109. https://doi.org/10.1103/PhysRevB.98.165109
299. K. Wang, Z. Guo, Y. Li, Y. Guo, H. Liu, W. Zhang, Z. Zou, Y. Zhang, and Z. Liu. *ACS Appl. Nano Mater.*, **2020**, *3*(11), 11363. https://doi.org/10.1021/acsanm.0c02449
300. X. Ma, P. Guo, C. Yi, Q. Yu, A. Zhang, J. Ji, Y. Tian, F. Jin, Y. Wang, K. Liu, T. Xia, Y. Shi, and Q. Zhang. *Phys. Rev. B*, **2016**, *94*(21), 214105. https://doi.org/10.1103/PhysRevB.94.214105
301. C. Ruppert, O. B. Aslan, and T. Heinz. *Nano Lett.*, **2014**, *14*(11), 6231. https://doi.org/10.1021/nl502557g

302. T. Sekine, T. Nakashizu, K. Toyoda, K. Uchinokura, and E. Matsuura. *Solid State Commun.*, **1980**, *35*(4), 371. https://doi.org/10.1016/0038-1098(80)90518-9

303. A. Berkdemir, H. R. Gutiérrez, A. R. Botello-Méndez, N. Perea-López, A. L. Elías, C.-I. Chia, B. Wang, V. H. Crespi, F. López-Urías, J.-C. Charlier, H. Terrones, and M. Terrones. *Sci. Rep.*, **2013**, *3*(1), 1755. https://doi.org/10.1038/srep01755

304. X. Luo, Y. Zhao, J. Zhang, M. Toh, C. Kloc, Q. Xiong, and S. Y. Quek. *Phys. Rev. B*, **2013**, *88*(19), 195313. https://doi.org/10.1103/PhysRevB.88.195313

305. E. del Corro, H. Terrones, A. Elias, C. Fantini, S. Feng, M. A. Nguyen, T. E. Mallouk, M. Terrones, and M. A. Pimenta. *ACS Nano*, **2014**, *8*(9), 9629. https://doi.org/10.1021/nn504088g

306. H. Terrones, E. D. Corro, S. Feng, J. M. Poumirol, D. Rhodes, D. Smirnov, N. R. Pradhan, Z. Lin, M. A. T. Nguyen, A. L. Elías, T. E. Mallouk, L. Balicas, M. A. Pimenta, and M. Terrones. *Sci. Rep.*, **2014**, *4*(1), 4215. https://doi.org/10.1038/srep04215

307. Y. C. Jiang, J. Gao, and L. Wang. *Sci. Rep.*, **2016**, *6*(1), 19624. https://doi.org/10.1038/srep19624

308. D. Wang, X. Zhang, G. Guo, S. Gao, X. Li, J. Meng, Z. Yin, H. Liu, M. Gao, L. Cheng, J. You, and R. Wang. *Adv. Mater.*, **2018**, *30*(44), 1803285. https://doi.org/10.1002/adma.201803285

309. J. R. Duffey and R. D. Kirby. *Phys. Rev. B*, **1981**, *23*(4), 1534. https://doi.org/10.1103/PhysRevB.23.1534

310. G. Radovsky, T. Shalev, and A. Ismach. *J. Mater. Sci.*, **2019**, *54*, 7768. https://doi.org/10.1007/s10853-019-03437-4

311. X. Duan, C. Wang, Z. Fan, G. Hao, L. Kou, U. Halim, H. Li, X. Wu, Y. Wang, J. Jiang, A. Pan, Y. Huang, R. Yu, and X. Duan. *Nano Lett.*, **2016**, *16*(1), 264. https://doi.org/10.1021/acs.nanolett.5b03662

312. S. Zhao, M. Lu, S. Xue, L. Tao, Y. Sui, and Y. Wang. *Appl. Phys. Lett.*, **2019**, *115*(6), 063105. https://doi.org/10.1063/1.5102085

313. C.-H. Ho, Z.-Z. Liu, and M.-H. Lin. *Nanotechnology*, **2017**, *28*(23), 235203. https://doi.org/10.1088/1361-6528/aa6f51

314. D. Dumcenco, K. Y. Chen, Y. P. Wang, Y.-S. Huang, and K. Tiong. *J. Alloys Compd.*, **2010**, *506*, 940. https://doi.org/10.1016/j.jallcom.2010.07.120

315. Y. Chen, D. O. Dumcenco, Y. Zhu, X. Zhang, N. Mao, Q. Feng, M. Zhang, J. Zhang, P.-H. Tan, Y.-S. Huang, and L. Xie. *Nanoscale*, **2014**, *6*(5), 2833. https://doi.org/10.1039/C3NR05630A

316. Z. Hemmat, J. Cavin, A. Ahmadiparidari, A. Ruckel, S. Rastegar, S. N. Misal, L. Majidi, K. Kumar, S. Wang, J. Guo, R. Dawood, F. Lagunas, P. Parajuli, A. T. Ngo, L. A. Curtiss, S. B. Cho, J. Cabana, R. F. Klie, R. Mishra, and A. Salehi-Khojin. *Adv. Mater.*, **2020**, *32*(26), 1907041. https://doi.org/10.1002/adma.201907041

317. B. Chakraborty, A. Bera, D. V. S. Muthu, S. Bhowmick, U. V. Waghmare, and A. K. Sood. *Phys. Rev. B*, **2012**, *85*(16), 161403. https://doi.org/10.1103/PhysRevB.85.161403

318. M. R. Laskar, D. N. Nath, L. Ma, E. W. Lee. II, C. H. Lee, T. Kent, Z. Yang, R. Mishra, M. A. Roldan, J.-C. Idrobo, S. T. Pantelides, S. J. Pennycook, R. C. Myers, Y. Wu, and S. Rajan. *Appl. Phys. Lett.*, **2014**, *104*(9), 092104. http://doi.org/10.1063/1.4867197

319. G. Bhowmik, K. Gruenewald, G. Malladi, T. Mowll, C. Ventrice, and M. Huang. *MRS Adv.*, **2019**, *4*(10), 609. https://doi.org/10.1557/adv.2019.24

320. Y. Jin, Z. Zeng, Z. Xu, Y.-C. Lin, K. Bi, G. Shao, T. S. Hu, S. Wang, S. Li, K. Suenaga, H. Duan, Y. Feng, and S. Liu. *Chem. Mater.*, **2019**, *31*(9), 3534. https://doi.org/10.1021/acs.chemmater.9b00913

321. N. Al-Dulaimi, D. J. Lewis, X. L. Zhong, M. Azad Malik, and P. O′Brien. *J. Mater. Chem. C*, **2016**, *4*(12), 2312. https://doi.org/10.1039/C6TC00489J

322. B. Wu, P. Kang, X. Zhang, H. Nan, K. Ostrikov, X. Gu, and S. Xiao. *Thin Solid Films*, **2021**, *722*, 138576. https://doi.org/10.1016/j.tsf.2021.138576

323. M. Zhong, C. Shen, L. Huang, H.-X. Deng, G. Shen, H. Zheng, Z. Wei, and J. Li. *NPJ 2D Mater. Appl.*, **2019**, *3*(1), 1. https://doi.org/10.1038/s41699-018-0083-1

324. Z. Luo, Y. Ouyang, H. Zhang, M. Xiao, J. Ge, Z. Jiang, J. Wang, D. Tang, X. Cao, C. Liu, and W. Xing. *Nat. Commun.*, **2018**, *9*(1), 2120. https://doi.org/10.1038/s41467-018-04501-4
325. D. Wang, X. Zhang, Y. Shen, and Z. Wu. *RSC Adv.*, **2016**, *6*(20), 16656. https://doi.org/10.1039/C6RA02610A
326. C.-T. Wu, S.-Y. Hu, K.-K. Tiong, and Y.-C. Lee. *Results Phys.*, **2017**, *7*, 4096. https://doi.org/10.1016/j.rinp.2017.10.033
327. P. Rathod, J. Egede, A. Voevodin, and N. Shepherd. *Appl. Phys. Lett.*, **2018**, *113*, 062106. https://doi.org/10.1063/1.5040119
328. F. Zhang, B. Zheng, A. Sebastian, D. H. Olson, M. Liu, K. Fujisawa, Y. T. H. Pham, V. O. Jimenez, V. Kalappattil, L. Miao, T. Zhang, R. Pendurthi, Y. Lei, A. L. Elías, Y. Wang, N. Alem, P. E. Hopkins, S. Das, V. H. Crespi, M.-H. Phan, and M. Terrones. *Adv. Sci.*, **2020**, *7*(24), 2001174. https://doi.org/10.1002/advs.202001174
329. M. N. Nasruddin and M. Sigiro. *Optik*, **2016**, *127*(4), 1599. https://doi.org/10.1016/j.ijleo.2015.11.056
330. S. Ahmed, X. Ding, P. Murmu, N. N. Bao, R. Liu, J. Kennedy, J. Ding, and J. Yi. *J. Alloys Compd.*, **2017**, *731*, 25. https://doi.org/10.1016/j.jallcom.2017.09.288
331. W. Y. Liang. In: Intercalation in Layered Materials / Ed. M. S. Dresselhaus. Boston, MA: Springer US, **1986**, 31-73. https://doi.org/10.1007/978-1-4757-5556-5_2
332. K. Nagao, M. Koyano, S. Katayama, Y. Yamamura, and T. Tsuji. *Phys. Status Solidi B*, **2001**, *223*, 281. https://doi.org/10.1002/1521-3951(200101)223:1<281::AID-PSSB281>3.0.CO;2-Z
333. C. M. Pereira and W. Y. Liang. *J. Phys. C: Solid State*, **1985**, *18*(32), 6075. https://doi.org/10.1088/0022-3719/18/32/019
334. S. Chen, V. L. Johnson, D. Donadio, and K. J. Koski. *J. Chem. Phys.*, **2020**, *153*(12), 124701. https://doi.org/10.1063/5.0018716
335. M. Kang, S. Rathi, I. Lee, D. Lim, J. Wang, L. Li, M. A. Khan, and G.-H. Kim. *Appl. Phys. Lett.*, **2015**, *106*(14), 143108. https://doi.org/10.1063/1.4917458
336. R. J. Toh, Z. Sofer, and M. Pumera. *J. Mater. Chem. A*, **2016**, *4*(47), 18322. https://doi.org/10.1039/C6TA08089H
337. X. Zhang, N. Peng, T. Liu, R. Zheng, M. Xia, H. Yu, S. Chen, M. Shui, and J. Shu. *Nano Energy*, **2019**, *65*, 104049. https://doi.org/10.1016/j.nanoen.2019.104049
338. H. Bark, Y. Choi, J. Jung, J. H. Kim, H. Kwon, J. Lee, Z. Lee, J. H. Cho, and C. Lee. *Nanoscale*, **2018**, *10*(3), 1056. https://doi.org/10.1039/C7NR07593F
339. G. J. Orchin, D. D. Fazio, A. D. Bernardo, M. Hamer, D. Yoon, A. R. Cadore, I. Goykhman, K. Watanabe, T. Taniguchi, J. W. A. Robinson, R. V. Gorbachev, A. C. Ferrari, and R. H. Hadfield. *Appl. Phys. Lett.*, **2019**, *114*(25), 251103. https://doi.org/10.1063/1.5097389
340. G. S. Gund, M. G. Jung, K.-Y. Shin, and H. S. Park. *ACS Nano*, **2019**, *13*(12), 14114. https://doi.org/10.1021/acsnano.9b06732
341. J. Shi, X. Wang, S. Zhang, L. Xiao, Y. Huan, Y. Gong, Z. Zhang, Y. Li, X. Zhou, M. Hong, Q. Fang, Q. Zhang, X. Liu, L. Gu, Z. Liu, and Y. Zhang. *Nat. Commun.*, **2017**, *8*(1), 958. https://doi.org/10.1038/s41467-017-01089-z
342. H. Chen, J. Si, S. Lyu, T. Zhang, Z. Li, C. Lei, L. Lei, C. Yuan, B. Yang, L. Gao, and Y. Hou. *ACS Appl. Mater. Interfaces*, **2020**, *12*(22), 24675. https://doi.org/10.1021/acsami.9b15039
343. G. Liu, B. Debnath, T. R. Pope, T. T. Salguero, R. K. Lake, and A. A. Balandin. *Nat. Nanotechnol.*, **2016**, *11*(10), 845. https://doi.org/10.1038/nnano.2016.108
344. W. Choi, N. Choudhary, G. H. Han, J. Park, D. Akinwande, and Y. H. Lee. *Mater. Today*, **2017**, *20*(3), 116. https://doi.org/10.1016/j.mattod.2016.10.002
345. Q. H. Wang, K. Kalantar-Zadeh, A. Kis, J. N. Coleman, and M. S. Strano. *Nat. Nanotechnol.*, **2012**, *7*(11), 699. https://doi.org/10.1038/nnano.2012.193
346. B. Radisavljevic, A. Radenovic, J. Brivio, V. Giacometti, and A. Kis. *Nat. Nanotechnol.*, **2011**, *6*(3), 147. https://doi.org/10.1038/nnano.2010.279
347. S. Das, M. Demarteau, and A. Roelofs. *Appl. Phys. Lett.*, **2015**, *106*(17), 173506. https://doi.org/10.1063/1.4919565

348. B. Hinnemann, P. G. Moses, J. Bonde, K. P. Jørgensen, J. H. Nielsen, S. Horch, I. Chorkendorff, and J. K. Nørskov. *J. Am. Chem. Soc.*, **2005**, *127*(15), 5308. https://doi.org/10.1021/ja0504690

349. A. P. Tiwari, T. G. Novak, X. Bu, J. C. Ho, and S. Jeon. *Catalysts*, **2018**, *8*(11), 551. https://doi.org/10.3390/catal8110551

350. J. Deng, W. Yuan, P. Ren, Y. Wang, D. Deng, Z. Zhang, and X. Bao. *RSC Adv.*, **2014**, *4*(66), 34733. https://doi.org/10.1039/C4RA05614K

351. F. Gong, M. Liu, Q. Liu, L. Gong, Y. Zhang, E. Meng, Y. Ma, L. Xu, and G. Wang. *Colloids Surf.*, *A*, **2020**, *601*, 124950. https://doi.org/10.1016/j.colsurfa.2020.124950

352. A. P. Murthy, J. Theerthagiri, J. Madhavan, and K. Murugan. *Phys. Chem. Chem. Phys.*, **2017**, *19*(3), 1988. https://doi.org/10.1039/C6CP07416B

353. M. Chatti, T. Gengenbach, R. King, L. Spiccia, and A. N. Simonov. *Chem. Mater.*, **2017**, *29*(7), 3092. https://doi.org/10.1021/acs.chemmater.7b00114

354. X. R. Guo, Y. Hou, R. Ren, and J. H. Chen. *Nanoscale Res. Lett.*, **2017**, *12*, 479. https://doi.org/10.1186/s11671-017-2248-9

355. K. O. Obodo, C. N. M. Ouma, J. T. Obodo, M. Braun, and D. Bessarabov. *Comput. Condens. Matter.*, **2019**, *21*, e00419. https://doi.org/10.1016/j.cocom.2019.e00419

356. H. Zhou, F. Yu, Y. Huang, J. Sun, Z. Zhu, R. J. Nielsen, R. He, J. Bao, W. A. Goddard Iii, S. Chen, and Z. Ren. *Nat. Commun.*, **2016**, *7*(1), 12765. https://doi.org/10.1038/ncomms12765

357. T. Kosmala, H. Coy Diaz, H.-P. Komsa, Y. Ma, A. V. Krasheninnikov, M. Batzill, and S. Agnoli. *Adv. Energy Mater.*, **2018**, *8*(20), 1800031. https://doi.org/10.1002/aenm.201800031

358. K. Xu, F. Wang, Z. Wang, X. Zhan, Q. Wang, Z. Cheng, M. Safdar, and J. He. *ACS Nano*, **2014**, *8*(8), 8468. https://doi.org/10.1021/nn503027k

359. Q. Gong, S. Sheng, H. Ye, N. Han, L. Cheng, and Y. Li. *Part. Part. Syst. Charact.*, **2016**, *33*(8), 576. https://doi.org/10.1002/ppsc.201500255

360. N. N. Som and P. K. Jha. *Int. J. Hydrog. Energy*, **2020**, *45*(44), 23920. https://doi.org/10.1016/j.ijhydene.2019.09.033

361. Y. Xia, J. Huang, W. Wu, Y. Zhang, H. Wang, J. Zhu, J. Yao, L. Xu, Y. Sun, L. Zhang, R. Lu, J. Xiong, and G. Zou. *ChemCatChem*, **2018**, *10*(19), 4424. https://doi.org/10.1002/cctc.201800757

362. N. H. Attanayake, A. C. Thenuwara, A. Patra, Y. V. Aulin, T. M. Tran, H. Chakraborty, E. Borguet, M. L. Klein, J. P. Perdew, and D. R. Strongin. *ACS Energy Lett.*, **2018**, *3*(1), 7. https://doi.org/10.1021/acsenergylett.7b00865

363. C. N. M. Ouma, K. O. Obodo, M. Braun, G. O. Amolo, and D. Bessarabov. *Appl. Surf. Sci.*, **2019**, *470*, 107. https://doi.org/10.1016/j.apsusc.2018.11.044

364. R. Chen, Y. Ao, C. Wang, and P. Wang. *Chem. Commun.*, **2020**, *56*(60), 8472. https://doi.org/10.1039/D0CC01300E

365. R. Vargas-Bernal. *Sensors*, **2019**, *19*(6), 1295. https://doi.org/10.3390/s19061295

366. H. Tang, L. N. Sacco, S. Vollebregt, H. Ye, X. Fan, and G. Zhang. *J. Mater. Chem. A*, **2020**, *8*(47), 24943. https://doi.org/10.1039/D0TA08190F

367. R. Kumar, W. Zheng, X. Liu, J. Zhang, and M. Kumar. *Adv. Mater. Technol.*, **2020**, *5*(5), 1901062. https://doi.org/10.1002/admt.201901062

368. S. Zhao, J. Xue, and W. Kang. *Chem. Phys. Lett.*, **2014**, *595–596*, 35. https://doi.org/10.1016/j.cplett.2014.01.043

369. Q. Yue, Z. Shao, S. Chang, and J. Li. *Nanoscale Res. Lett.*, **2013**, *8*(1), 425. https://doi.org/10.1186/1556-276x-8-425

370. M. J. Szary. *Appl. Surf. Sci.*, **2020**, *529*, 147083. https://doi.org/10.1016/j.apsusc.2020.147083

371. T. Wang, H. Shang, and Q. Zhang. *Chem. Eng. Sci.*, **2020**, *228*, 115950. https://doi.org/10.1016/j.ces.2020.115950

372. J. Cao, J. Zhou, Y. Zhang, and X. Liu. *Microelectron. Eng.*, **2018**, *190*, 63. https://doi.org/10.1016/j.mee.2018.01.012

373. J. Zhu, H. Zhang, Y. W. Tong, L. Zhao, Y. F. Zhang, Y. Z. Qiu, and X. N. Lin. *Appl. Surf. Sci.*, **2017**, *419*, 522. https://doi.org/10.1016/j.apsusc.2017.04.157

374. B. Zhao, L. L. Liu, G. D. Cheng, T. Li, N. Qi, Z. Q. Chen, and Z. Tang. *Mater. Des.*, **2017**, *113*, 1. https://doi.org/10.1016/j.matdes.2016.10.005
375. H. Luo, Y. J. Cao, J. Zhou, J. M. Feng, J. M. Cao, and H. Guo. *Chem. Phys. Lett.*, **2016**, *643*, 27. https://doi.org/10.1016/j.cplett.2015.10.077
376. D. Ma, W. Ju, T. Li, G. Yang, C. He, B. Ma, Y. Tang, Z. Lu, and Z. Yang. *Appl. Surf. Sci.*, **2016**, *371*, 180. https://doi.org/10.1016/j.apsusc.2016.02.230
377. K. Ding, Y. Lin, and M. Huang. *Vacuum*, **2016**, *130*, 146. https://doi.org/10.1016/j.vacuum.2016.05.005
378. Y. Wang, B. Wang, R. Huang, B. Gao, F. Kong, and Q. Zhang. *Physica E*, **2014**, *63*, 276. https://doi.org/10.1016/j.physe.2014.06.017
379. J. Sun, N. Lin, H. Ren, C. Tang, L. Yang, and X. Zhao. *RSC Adv.*, **2016**, *6*(21), 17494. https://doi.org/10.1039/C5RA24592C
380. H. Nguyen, D.-Q. Hoang, T. P. Dao, C. Nguyen, H. V. Phuc, N. Hieu, D. Hoat, H. Luong, T. Du Hien, K. Pham, and T. Vu. *Superlattices Microstruct.*, **2020**, 106454. https://doi.org/10.1016/j.spmi.2020.106454
381. J. Ni, W. Wang, M. Quintana, F. Jia, and S. Song. *Appl. Surf. Sci.*, **2020**, *514*, 145911. https://doi.org/10.1016/j.apsusc.2020.145911
382. J.-H. Kim, A. Mirzaei, H. W. Kim, and S. S. Kim. *Sens. Actuators, B*, **2020**, *313*, 128040. https://doi.org/10.1016/j.snb.2020.128040
383. H. Tang, Y. Li, R. Sokolovskij, L. Sacco, H. Zheng, H. Ye, H. Yu, X. Fan, H. Tian, T.-L. Ren, and G. Zhang. *ACS Appl. Mater. Interfaces*, **2019**, *11*(43), 40850. https://doi.org/10.1021/acsami.9b13773